# Tensor network and quantum simulations of 1+1-dimensional quantum electrodynamics

DISSERTATION

zur Erlangung des akademischen Grades
doctor rerum naturalium
(Dr. rer. nat.)
im Fach: Physik
Spezialisierung: Theoretische Physik

eingereicht an der
Mathematisch-Naturwissenschaftlichen Fakultät
der Humboldt-Universität zu Berlin

von

**Takis Angelides**
geboren am 2 Oktober 1996 in Nicosia, Zypern

Präsidentin der Humboldt-Universität zu Berlin:
Prof. Dr. Julia von Blumenthal

Dekan der Mathematisch-Naturwissenschaftlichen Fakultät:
Prof. Dr. Emil List-Kratochvil

Gutachter: 1. Prof. Dr. Agostino Patella
2. Prof. Dr. Karl Jansen
3. Prof. Dr. Norbert Schuch

Tag der mündlichen Prüfung: 26.09.2025

*To my family,*

Parts of this work reuse material from the publications and preprints listed below.

The author of this thesis has been the main contributor for the following work:

- **Angelides, T.**, Guo Y., Jansen K., Kühn, S., Magnifico, G., *Meson thermalization with a hot medium in the open Schwinger model*, J. High Energ. Phys. 2025, 195 (2025) https://doi.org/10.1007/JHEP04(2025)195
- **Angelides, T.**, Naredi, P., Crippa, A., Jansen, K., Kühn, S., Tavernelli, I., Wang, D. S., *First-Order Phase Transition of the Schwinger Model with a Quantum Computer*, npj Quantum Information **11**, 6 (2025). https://doi.org/10.1038/s41534-024-00950-6
- **Angelides, T.**, Funcke, L., Jansen, K., Kühn, S., *Computing the Mass Shift of Wilson and Staggered Fermions in the Lattice Schwinger Model with Matrix Product States*, Phys. Rev. D **108**, 014516 (2023). https://doi.org/10.1103/PhysRevD.108.014516
- **Angelides, T.**, Funcke, L., Jansen, K., Kühn, S., *Mass Renormalization of the Schwinger Model with Wilson and Staggered Fermions in the Hamiltonian Lattice Formulation*, PoS(LATTICE2022)046 (2023). https://doi.org/10.22323/1.430.0046

The author of this thesis has also contributed to the following work:

- Guo, Y., **Angelides, T.**, Jansen, K., Kühn, S., *Concurrent VQE for Simulating Excited States of the Schwinger Model*, arXiv:2407.15629 [quant-ph] (2024). https://arxiv.org/abs/2407.15629

# Acknowledgments

I would like to start by thanking my supervisor Prof. Karl Jansen for his support and guidance throughout my Ph.D., as well as Prof. Agostino Patella for his supervision at Humboldt University and the insightful discussions. I give my special thanks to Stefan Kühn for introducing me to tensor networks and his invaluable support and supervision over the years. Further, I express my appreciation to my colleagues for the pleasant work environment: Leonardo Chimirri, Cenk Tüysüz, Maria Demidik, Arianna Crippa, Manuel Schneider, Miriam Goldack, Tim Schwägerl, Hala Elhag, Yibin Guo, Yahui Chai and many more at our DESY campus. I extend my love to my family for the life-long support: Kakia, Christia, Andrea and Andros Angelides. I also would like to extend my love to my friends with whom I have spent a wonderful four years in Berlin-Brandenburg. Finally, I acknowledge that my work has been partly funded by the European Union's Horizon 2020 Research and Innovation Programme under the Marie Sklodowska-Curie COFUND scheme with grant agreement no. 101034267.

# Abstract

We consider the Schwinger model with a single fermion flavor in the presence of a topological $\theta$-term as a benchmark model to develop quantum computing (QC) and tensor network (TN) techniques, as well as to probe its physics, which shares many similarities with quantum chromodynamics (QCD). The techniques developed aim to eventually enhance our capabilities in simulating strongly coupled non-perturbative regimes of the Standard Model, particularly in unexplored regions of its phase diagram where the conventionally used techniques are not applicable.

Discretizing fermions on a lattice is a crucial step in simulating lattice gauge theory (LGT) models such as the Schwinger model. Using the two common discretization schemes of Wilson and staggered fermions, we first explore the additive mass renormalization induced by these schemes within the Hamiltonian formalism relevant for QC and TNs. By formulating a method to measure this mass renormalization, we demonstrate its dependence on various system parameters. This, in turn, allows for more reliable and precise continuum extrapolations of relevant observables, for which we achieve excellent agreement with results from continuum mass perturbation theory. This work introduces, for the first time, a method to measure the mass renormalization in the Hamiltonian formalism, enabling QC and TNs to require fewer resources to achieve higher precision in continuum extrapolations. These extrapolations are essential for LGTs computations in higher dimensions to match experimental results, such as those from the large hadron collider (LHC) experiment.

Secondly, we demonstrate the capabilities of quantum hardware in simulating the first-order phase transition of the model, utilizing a composite set of state-of-the-art error mitigation techniques. While we classically simulate the variational quantum eigensolver (VQE) algorithm to acquire the ground states at the relevant points of the phase diagram as parameterized quantum circuits (PQCs), we perform inference runs by preparing these states on IBM's noisy intermediate-scale quantum (NISQ) devices and measure observables that signal the phase transition. Our results show that these quantum devices are able to reproduce the transition with reasonable accuracy, showcasing the potential of NISQ devices in probing the phase diagram of LGTs. Additionally, we perform continuum extrapolations of the electric field observable using TNs, providing an estimate of the resources required for continuum extrapolations in QC.

Finally, the Schwinger model is studied in the context of open quantum system (OQS) in the presence of a hot environment. We prepare mesonic states of the model, such as the Schwinger boson or the electric field flux state, and evolve them under the influence of this environment, following the dynamics governed by a Lindblad master equation in the Markovian quantum Brownian motion (QBM) limit. The evolution is carried out using TNs and the adaptive time-dependent density matrix renormalization group (DMRG) (ATD-DMRG) algorithm. Specifically, we probe the thermalization time of these mesonic states as a function of various relevant parameters. Additionally, we explore the connection between the thermalization time and mutual information within the states. Finally, we demonstrate how our method can scale to larger system sizes, achieving excellent preservation of the expected parity symmetry of the electric field observable. The relevance of this work to quarkonia within the quark gluon plasma (QGP) produced at the LHC and relativistic heavy ion collider (RHIC) is discussed throughout.

# Zusammenfassung

Wir betrachten das Schwinger-Modell mit einer einzigen Fermion-Flavour in Anwesenheit eines topologischen $\theta$-Terms als ein Benchmark-Modell zur Entwicklung von quantum computing (QC)- und tensor network (TN)-Techniken sowie zur Untersuchung seiner Physik, die viele Gemeinsamkeiten mit quantum chromodynamics (QCD) aufweist. Die entwickelten Techniken zielen darauf ab, letztlich unsere Fähigkeiten zur Simulation stark gekoppelte, nichtperturbativer Regime des Standardmodells in der Zukunft zu verbessern, insbesondere in bislang unerforschten Bereichen seines Phasendiagramms, in denen herkömmliche Methoden nicht anwendbar sind.

Die Diskretisierung von Fermionen auf einem Gitter ist ein entscheidender Schritt bei der Simulation von lattice gauge theory (LGT)-Modellen wie dem Schwinger-Modell. Unter Verwendung der beiden gängigen Diskretisierungsschemata – Wilson- und gestaggerte Fermionen – untersuchen wir zunächst die additive Massenrenormierung, die durch diese Schemata im Hamilton-Formalismus hervorgerufen wird, welcher für QC und TNs relevant ist. Durch die Entwicklung einer Methode zur Messung dieser Massenrenormierung zeigen wir deren Abhängigkeit von verschiedenen Systemparametern. Dies ermöglicht wiederum zuverlässigere und präzisere Kontinuumsextrapolationen relevanter Observablen, bei denen wir eine ausgezeichnete Übereinstimmung mit Ergebnissen der kontinuierlichen Massen-Störungstheorie erzielen. Diese Arbeit stellt erstmals eine Methode zur Messung der Massenrenormierung im Hamilton-Formalismus vor, wodurch QC und TNs mit weniger Ressourcen eine höhere Präzision bei Kontinuumsextrapolationen erreichen können. Solche Extrapolationen sind essenziell für LGTs-Berechnungen in höheren Dimensionen, um experimentelle Ergebnisse wie die des large hadron collider (LHC)-Experiments reproduzieren zu können.

Zweitens demonstrieren wir die Leistungsfähigkeit von Quantenhardware bei der Simulation des Phasenübergangs erster Ordnung des Modells unter Einsatz eines kombinierten Sets modernster Fehlerkorrekturmethoden. Während wir den variational quantum eigensolver (VQE)-Algorithmus klassisch simulieren, um die Grundzustände an relevanten Punkten des Phasendiagramms als parametrisierte Quanten-Schaltkreise zu erhalten, führen wir Inferenzläufe durch, indem wir diese Zustände auf IBMs noisy intermediate-scale quantum (NISQ)-Geräten präparieren und Observablen messen, die den Phasenübergang signalisieren. Unsere Ergebnisse zeigen, dass diese Quantenprozessoren in der Lage sind, den Übergang mit angemessener Genauigkeit zu reproduzieren, was das Potenzial von NISQ-Geräten zur

Erforschung des Phasendiagramms von LGTs unterstreicht. Zusätzlich führen wir Kontinuumsextrapolationen der elektrischen Feld-Observable unter Verwendung von TNs durch, um eine Abschätzung der für QC benötigten Ressourcen bei solchen Extrapolationen zu geben.

Abschließend wird das Schwinger-Modell im Kontext von open quantum system (OQS) in Anwesenheit einer heißen Umgebung untersucht. Wir präparieren mesonische Zustände des Modells, wie den Schwinger-Boson oder den elektrischen Feldflusszustand, und lassen sie unter Einfluss dieser Umgebung gemäß der durch eine Lindblad-Mastergleichung im Markovschen quantum Brownian motion (QBM)-Grenzfall bestimmten Dynamik evolvieren. Die Zeitentwicklung erfolgt mittels TNs und dem adaptive time-dependent density matrix renormalization group (DMRG) (ATD-DMRG)-Algorithmus. Konkret untersuchen wir die Thermalisierungszeit dieser mesonischen Zustände als Funktion verschiedener relevanter Parameter. Zusätzlich erforschen wir die Verbindung zwischen der Thermalisierungszeit und der gegenseitigen Information innerhalb der Zustände. Schließlich zeigen wir, wie unsere Methode auf größere Systemgrößen skaliert werden kann, wobei die erwartete Paritätssymmetrie der elektrischen Feldobservable exzellent erhalten bleibt. Die Relevanz dieser Arbeit für Quarkonia im quark gluon plasma (QGP), wie er beim LHC und relativistic heavy ion collider (RHIC) erzeugt wird, wird durchgehend diskutiert.

# Contents

Abstract v

List of Figures xi

List of Tables xxii

List of Abbreviations xxiv

Introduction 1

1 Theory 4
- 1.1 Continuum Schwinger model 5
- 1.2 Fermion doubling problem 9
- 1.3 Wilson fermions 10
- 1.4 Staggered fermions 13
- 1.5 Open quantum systems 15

2 Tensor network methods 18
- 2.1 Matrix product states 19
- 2.2 Entanglement entropy and bond dimension 20
- 2.3 Matrix product operators 22
- 2.4 Canonical form 25
- 2.5 Density matrix renormalization group 25
- 2.6 Adaptive time-dependent DMRG 28

3 Quantum computing methods 33
- 3.1 Variational quantum eigensolver 34
  - 3.1.1 Quantum circuits 34
  - 3.1.2 Measuring observables 34
  - 3.1.3 Algorithm routine 36
- 3.2 Error Mitigation 37
  - 3.2.1 Readout Error Mitigation 37
  - 3.2.2 Zero Noise Extrapolation 38

3.2.3 Pauli Twirling . . . 38
3.2.4 Dynamical Decoupling . . . 39

4 Computing the mass shift of the lattice Schwinger model 40
4.1 Wilson fermions Hamiltonian . . . 41
4.2 Measuring the mass shift . . . 42
4.3 Parameter dependence of mass shift . . . 44
4.3.1 Volume . . . 44
4.3.2 Lattice spacing . . . 44
4.3.3 $\theta$-parameter . . . 46
4.3.4 Wilson parameter . . . 48
4.4 Continuum extrapolation . . . 48
4.4.1 Electric Field Density . . . 49
4.4.2 Schwinger Boson Mass . . . 50
4.5 Staggered fermions . . . 51
4.5.1 Electric field density method for staggered fermions . . . 52
4.5.2 Energy gap method . . . 52

5 First-order phase transition of the Schwinger model with a quantum computer 56
5.1 Observables . . . 57
5.2 Parametric circuits . . . 58
5.3 Comparison of parametric circuits with VQE . . . 61
5.4 Lattice effects on the phase transition . . . 64
5.5 Inference runs on quantum hardware . . . 66
5.6 Error mitigation . . . 67
5.7 Continuum extrapolation with MPS . . . 70

6 Open quantum systems 74
6.1 String thermalization . . . 76
6.1.1 Dependence on $D$, $l_0$ and $m$ . . . 76
6.1.2 Correlations between thermalization time and mutual information . . 81
6.1.3 Temperature dependence . . . 83
6.1.4 Larger system sizes and symmetry preservation . . . 85
6.2 Schwinger boson thermalization . . . 89

Conclusion 93

Bibliography 95

# List of Figures

1.1 Working in the large mass limit, the top line shows the configuration for case 1 of Eq. (1.4) which is a state in the absence of electrical charges and with only a background electric field $gl_0$ present. For case 2 in Eq. (1.5), the bottom line shows the case of a negative-positive charge pair set a distance $\Delta x$ apart. . . 7

1.2 Illustration of the phase diagram of the Schwinger model in the presence of a topological term in the $m/g-\theta$ plane. Since the physics is periodic in $\theta$ with period $2\pi$, only the first period is shown. The critical line (shown in black) indicates the first-order phase transitions occurring at $\theta=\pi$ for masses larger than the critical one $m_c/g \approx 0.33$, which ends in a second-order phase transition (green dot) exactly at $m_c/g$. Below the critical mass no transitions occur. . . . . . . . . . . . . . . . . . . . . . . . . . . . . . . . . . . 7

2.1 $(a)$: Examples of rank-2 and rank-3 tensors. The circles represent tensors $A$, with vertical legs indicating physical indices $\sigma$ and horizontal legs representing bond indices $\alpha$. $(b)$: Diagrammatic representation of an matrix product state (MPS) as described in Eq. (2.2). The connected legs signify contractions over the shared indices of the $A$ tensors. . . . . . . . . . . . . . . . . . . . . . . . . 20

2.2 Procedure for performing an singular value decomposition (SVD) on a multi-dimensional tensor, illustrated with a 4-site example. The first step is to reshape the tensor $\psi_{\sigma_0\sigma_1\sigma_2\sigma_3}$ into a matrix $\psi_{IJ}$, where $I \in [\sigma_0, \sigma_1]$ and $J \in [\sigma_2, \sigma_3]$. This matrix is then decomposed using the singular value decomposition (SVD) as $\psi_{IJ} = \sum_a U_{Ia} S_{aa} V^{\dagger}_{aJ}$. Here, $U$ and $V$ are unitary matrices, and $S$ is a diagonal matrix containing the singular values. . . . . . . . . . . . . . . . . . . . . . . . 21

2.3 $(a)$: Examples of rank-3 and rank-4 tensors. The squares represent tensors $W$, with vertical legs indicating physical indices $\sigma, \sigma'$, and horizontal legs representing bond indices $\alpha$. $(b)$: Diagrammatic representation of an matrix product operator (MPO), as described in Eq. (2.16). The connected legs denote contractions over the shared indices of the $W$ tensors. . . . . . . . . . . . . . 23

2.4 The diagram measures the expectation value $\langle\psi|\,\mathcal{O}\,|\psi\rangle$ of an operator $\mathcal{O}$ with respect to the quantum state $|\psi\rangle$. The operator is represented by the green boxes forming the MPO in the middle. The quantum state $|\psi\rangle$ is represented by the blue circles forming the MPS on the bottom and by convention the MPS with its legs facing down represents $\langle\psi|$. . . . . . . . . . . . . . . . . . . . . . . . . 24

2.5 ($a$): Left canonical form (LCF) for an matrix product state (MPS) site, corresponding to Eq. (2.20). ($b$): Right canonical form (RCF) for an matrix product state (MPS) site, corresponding to Eq. (2.21). ($c$): Left canonical form (LCF) for an matrix product operator (MPO) site, corresponding to Eq. (2.22). ($d$): Right canonical form (RCF) for an matrix product operator (MPO) site, corresponding to Eq. (2.23). . . . . . . . . . . . . . . . . . . . . . . . . . . . . . . 26

2.6 The top diagram defines $P_n$ inside the green box, while the bottom diagram defines $N_n$ inside the cyan box. These two tensors are used to derive the optimization formula in Eq. (2.26) within the density matrix renormalization group (DMRG) algorithm. The division of the top by the bottom diagram gives the energy $E = \langle\psi|\,H\,|\psi\rangle \,/\, \langle\psi|\psi\rangle$ to be minimized by the DMRG. . . . . 27

2.7 ($a$): Initial matrix product operator (MPO) representing the system's density matrix $\rho_S(t)$. ($b$): Separating the legs on each site with singular value decomposition (SVD). ($c$): matrix product state (MPS) representing $\rho_S(t)$ equivalent to the matrix product operator (MPO) in ($a$). . . . . . . . . . . . . . . . . . . . . 30

2.8 ($a$): Measuring the expectation value $\mathrm{Tr}(O\rho_S(t))$ with the top matrix product operator (MPO) (green boxes) representing a generic operator $O$ and the bottom matrix product operator (MPO) (blue boxes) representing the system's density matrix $\rho_S(t)$. ($b$): The equivalent contraction to ($a$) after the transformation of $\rho_S(t)$ from matrix product operator (MPO) to matrix product state (MPS) (blue circles) shown in Fig. 2.7. . . . . . . . . . . . . . . . . . . . . . . . . . . . . 30

2.9 Schematic drawing example of the even group (bottom green boxes), Taylor group (middle red boxes) and odd group (top blue box) for $\mathcal{L}$ in Eq. (2.31) at $N = 4$. These groups are applied to the matrix product state (MPS) at the very bottom representing $\rho_S$ as required by Eq. (2.32), although here only $e^{\tau\mathcal{L}_O}e^{\frac{\tau}{2}\mathcal{L}_T}e^{\frac{\tau}{2}\mathcal{L}_E}$ is shown. . . . . . . . . . . . . . . . . . . . . . . . . . . . . 31

3.1 A quantum circuit of two qubits. The states $|0\rangle$ specify the initial state of the qubits. The qubits are spin-1/2 degrees of freedom, hence, can be in the general normalized state $|\psi\rangle = \alpha\,|0\rangle + \beta\,|1\rangle$. In other words, their basis consists of the eigenvectors of the Pauli $Z$ operator. Actions on these qubits are placed on the horizontal lines. These actions are unitary operators called gates. Here we have the gate $R_P(\alpha) = \exp\{-i\alpha P/2\}$ with $P \in \{X, Y, Z\}$ as a parameterized gate. The parameter $\alpha$ can be varied to change the action of the gate. We also define the parametric gate $R(\alpha, \beta, \gamma) = R_X(\gamma)R_Z(\beta)R_X(\alpha)$. The third gate is called the CNOT gate which has the action of flipping the state of the qubit on which the cross is placed, if the qubit from which the line of gate starts from is in the state $|1\rangle$. Finally, the two boxes at the end represent measurement of the qubits in the $Z$ basis. This collapses the wavefunction of the qubit into either $|0\rangle$ or $|1\rangle$. . . . . . . . . . . . . . . . . . . . . . . . . . . . . . . . . . . . . 34

3.2 The variational quantum eigensolver (VQE) routine, as described in Sec. 3.1.3, takes as input a Hamiltonian, a parameterized quantum circuit (PQC) ansatz, and an initial set of parameters $\boldsymbol{\theta}$. The algorithm begins by preparing a fixed initial state and subsequently applying the parameterized circuit to this state. The energy expectation value with respect to the resulting quantum state is then measured and passed to a classical optimizer, which iteratively updates the parameters to minimize the energy. This optimization cycle continues until the energy converges to a desired threshold. . . . . . . . . . . . . . . . . . . . . . 36

4.1 $\mathcal{F}/g$ (electric field density (EFD)) versus lattice mass $m_{\text{lat}}/g$. The markers represent data for different physical volumes $N/\sqrt{x} = 10$ (purple circles), 15 (yellow triangles), 25 (black crosses), and 40 (blue squares), demonstrating the presence of finite-volume effects for the mass shift (MS). Following Eq. (1.7), the electric field density (EFD) vanishes for $m_{\text{r}}/g = 0$; therefore, the intercepts of the data curves with $\mathcal{F}/g = 0$ (red dashed line) correspond to minus the mass shift (MS) for a given volume. Note that the error bars are much smaller than the markers and thus, are not visible. . . . . . . . . . . . . . . . . . . . . . . . 43

4.2 $\langle L_W \rangle$ (electric field density (EFD)) against inverse bond dimension $1/D$ to extrapolate to $D \to \infty$ with $D = 40, 60, 80$. This example is for Wilson fermions at $N = 100$, $l_0 = 0.1$, $m_{\text{lat}}/g = -0.08236266$. Similar behavior was observed for staggered fermions as well. The error bars are emanating from the variational algorithm to compute the relevant ground states. As shown by the calculation on the top of the y-axis, the points are all closely converged to the value corresponding to the $D \to \infty$ limit. . . . . . . . . . . . . . . . . . . . . . . . . . . 43

4.3 Mass shift (MS) versus inverse volume. The markers show data for volumes $N/\sqrt{x}$ between 10 and 40, where $x = 10$ and $l_0 = 0.1$ are fixed. The mass shift (MS) exhibits a plateau for volumes $N/\sqrt{x} \gtrsim 30$, with a relative difference in the mass shift (MS) of $\sim 0.01\%$ for the largest two volumes of 35 and 40 (see inset). The error bars are much smaller than the markers and thus are not visible. . . . . 45

4.4 Mass shift (MS) as a function of the lattice spacing $ag$. We fix $l_0 = 0.125$ and $N/\sqrt{x} = 30$, with $N$ ranging from 300 to 500. To first order, the $ag$-dependence of the mass shift (MS) is linear. As before, the error bars are much smaller than the markers and thus are not visible. . . . . 45

4.5 Mass shift (MS) versus lattice spacing $ag = 1/\sqrt{x}$ for two different values of the background field, $l_0 = \theta/(2\pi) = 0.03$ (black crosses) and 0.25 (red circles), demonstrating that the mass shift (MS) is different when $l_0 = \theta/2\pi$ varies. The volume is fixed to $N/\sqrt{x} = 20$, with $N$ ranging from 25 to 90. As before, the error bars are much smaller than the markers and thus are not visible. . . . . 46

4.6 Difference in mass shift (MS) between two different values of the background field, $l_0 = \theta/(2\pi) = 0.25$ and 0.03, see Eq. (4.6), as a function of the lattice spacing $ag$. The volume is fixed to $N/\sqrt{x} = 20$, with $N$ ranging from 25 to 90. The inset shows data for $x = 1/(ag)^2 = 12.25$, 16, and 20.25, which demonstrate that the $\theta$-dependence of the mass shift (MS) becomes negligible for small $ag$. As before, the error bars are much smaller than the markers and thus are not visible. . . . . 47

4.7 Mass shift (MS) versus background electric field $l_0$. The field $l_0 = \theta/2\pi$ is swept over a full period between 0 and 1, and the mass shift (MS) shows the expected periodicity in $l_0$. The data points correspond to $l_0 \in [0.01, 0.9526]$, $N = 100$, and $x = 1$. As before, the error bars are much smaller than the markers and thus are not visible. . . . . 47

4.8 $\mathcal{F}/g$ (electric field density (EFD)) as a function of the lattice mass $m_{\text{lat}}/g$ for the Wilson parameter $r = 1$ (black solid line with lower $x$-axis) and $r = -1$ (blue dashed line with upper $x$-axis). We fix $N = 100$, $x = 1$, and $l_0 = 0.125$. The horizontal red dotted line indicates $\mathcal{F}/g = 0$, and the orange dash-dotted vertical line passes the intersection point of the blue and black lines with the red dotted line. The intersection is at a value of $m_{\text{lat}}/g = 0.214681$ for $r = -1$ (upper $x$-axis) and $m_{\text{lat}}/g = -0.214681$ for $r = 1$ (lower $x$-axis). As before, the error bars are much smaller than the markers and thus are not visible. . . . . 48

4.9 $\mathcal{F}/g$ (electric field density (EFD)) as a function of lattice spacing $ag$. Black crosses represent data incorporating the mass shift (MS) for $m_r/g = 0.03$, while green triangles correspond to data without the mass shift (MS), keeping $m_{\text{lat}}/g = 0.03$ fixed. We set $l_0 = 0.125$ and $N/\sqrt{x} = 20$. For data that include the mass shift (MS), a linear fit suffices, as expected from the $\mathcal{O}(ag)$ scaling behavior of non-improved Wilson fermions [268]. In contrast, for data without the mass shift (MS), we estimate $\mathcal{F}/g$ at $ag \to 0$ by fitting quadratic, cubic, and quartic polynomials and computing a weighted average of their $y$-intercepts. We use mean squared errors (MSEs) as weights and determine the uncertainty of each intercept using the method in Sec. 4.2. The final error is obtained by adding individual uncertainties in weighted quadrature. Error bars are too small to be visible. . . . . . . . . . . . . . . . . . . . . . . . . . . . . . . . . . 49

4.10 $\mathcal{F}/g$ (electric field density (EFD)) extrapolated to the continuum as a function of mass $m/g$. The black crosses correspond to data that incorporate the mass shift (MS), where $m/g$ represents the renormalized mass $m_r/g = m_{\text{lat}}/g +$ MS. Green circles represent data where the mass shift (MS) is ignored, with $m/g = m_{\text{lat}}/g$. The red curve denotes the continuum perturbative prediction from Eq. (1.7), where $m/g$ refers to the continuum mass. The extrapolation to $ag = 0$ is performed using eight points with $N \in [100, 300]$, keeping $l_0 = 0.125$ and $N/\sqrt{x} = 20$ fixed. Error bars for the black crosses are too small to be visible. 50

4.11 Schwinger boson mass (vector mass gap), $M_S/g$, as a function of the squared lattice spacing, $(ag)^2$. The data points (black crosses) correspond to $l_0 = 0.125$ and $m_r/g = 0$, with a fixed volume of $N/\sqrt{x} = 40$ for $N \in [300, 600]$. A quadratic fit in $ag$ (red line) yields an extrapolated value of $M_S/g = 0.5642 \pm 0.0011$, which aligns with the theoretical expectation $M_S/g = 1/\sqrt{\pi} \approx 0.5641$ from Eq. (1.6). . . . . . . . . . . . . . . . . . . . . . . . . . . . . . . . . 51

4.12 $\mathcal{F}/g$ (electric field density (EFD)) as a function of the lattice mass $m_{\text{lat}}/g$ for staggered fermions, with $x = 10$ and $l_0 = 0.125$. The horizontal blue dotted line marks the point where the electric field density (EFD) vanishes, while the vertical purple dashed line represents the theoretical prediction for the mass shift (MS) from Ref. [267]. Different markers indicate data for various physical volumes: $N/\sqrt{x} = 10$ (yellow triangles), 20 (black crosses), and 30 (red circles). The error bars, stemming from the extrapolation in bond dimension, are too small to be visible. . . . . . . . . . . . . . . . . . . . . . . . . . . . . . . . . 53

4.13 The behavior of $m_s/g$ (mass shift (MS)) as a function of $1/\sqrt{x}$ for $l_0 = 0$ (red circles) and $l_0 = 0.08$ (blue squares), where $l \equiv l_0$ for this plot. The mass shift (MS) is estimated using the gap method by solving Eq. (4.10) for various $N$ using matrix product state (MPS), followed by extrapolation to infinite volume for a fixed $x$. For comparison, results from the electric field density (EFD) method are also shown for $l_0 = 0.08$ (green triangles). The black line represents the analytically computed value $1/(8\sqrt{x})$ from Ref. [267] for periodic boundary conditions. . . . . . . . . . . . . . . . . . . . . . . . . . . . . . . . . . . . . . 54

4.14 Results for $\Delta/(2\sqrt{x}) - 1/\sqrt{\pi}$ versus $m_{\text{lat}}/g$ for 40 physical qubits and $x = 1$ from concurrent variational quantum eigensolver (cVQE) (open symbols) and a direct matrix product state (MPS) calculation ($\times$, $+$) for comparison, where $\Delta$ is the energy gap $E_1 - E_0$. The red circles (blue squares) and red triangles (blue lower triangle) correspond to results for $l_0 = 0$ and $l_0 = 0.08$, respectively, for eight (ten) layers of the ladder ansatz from Fig. 3(b). The black "$\times$" ("$+$") represent data from a direct matrix product state (MPS) calculation with bond dimension $D = 40$, serving as the reference value for $l_0 = 0$ ($l_0 = 0.08$). The dashed line marks $\Delta/(2\sqrt{x}) - 1/\sqrt{\pi} = 0$, and its intersection with the concurrent variational quantum eigensolver (cVQE) data provides an estimate of the mass shift (MS), up to a minus sign. . . . . . . . . . . . . . . . . . . . . . 55

5.1 Decomposition of a generic SO(4) gate depending on the six parameters $\theta_1, \ldots, \theta_6$ (a) the $R_{XX+YY}(\theta) = R_{Z_0} \exp(-i\theta(XX + YY)/2) R_{Z_0}^\dagger$ (b), into CNOT and Pauli rotation gates. The $R_{Z_0}$ rotations in the definition of $R_{XX+YY}(\theta)$ restrict the state to the real subspace. Boxes acting on a single qubit correspond to Pauli rotation gates, $R_P(\alpha) = \exp\{-i\alpha P/2\}$ with $P \in \{X, Y, Z\}$. Single-qubit gates where the argument is omitted refer to rotations around an angle $\pi/2$, $R_P(\pi/2)$. The light blue boxes represent the parameterized gates which are $R(\alpha, \beta, \gamma) = R_X(\gamma) R_Z(\beta) R_X(\alpha)$ in (a) and $R_Y(\theta)$ in (b). Panel (c) and (d) illustrate one layer of the brick and ladder ansatz, respectively, both following a non-parametric part for preparing the initial state $|\psi_{in}\rangle$ (yellow box). The first layer in the brick ansatz has a CNOT-depth of 4 whereas in ladder it is $2n - 2$, where $n$ is the number of qubits, and in both cases it increases by 4 with each layer. . . . . . . . . . . . . . . . . . . . . . . . . . 59

5.2 Electric field density (EFD) $\langle L_{W,S} \rangle$ and particle number (PN) $\langle P_{W,S} \rangle$ against $l_0$ with data from quantum hardware (black crosses), as compared to the noiseless expectation values (red pluses) and exact diagonalization (blue circles) for Wilson and staggered fermions respectively. The staggered fermions in this case have the same number of qubits as the Wilson fermions. Hence, while the title of each column specifies the $N$ for Wilson fermions, for staggered it is taken to be double that value. The lattice mass for these data is set to $m_{\text{lat}}/g = 10$, so that we are above the second order phase transition of Fig. 1.2, without having to account for the mass shift (MS). Therefore, we can observe the first-order phase transition. Note that the error bars, which are discussed in Sec. 5.4, are much smaller than the y-scale and thus, are not visible. . . . . . . . . . . . . 62

5.3 The description for this figure follows Fig. 5.2, however the lattice mass here is set to $m_{\text{lat}}/g = 0$, so that we are below the second order phase transition and thus observe no first-order phase transition as expected. Note that the error bars are much smaller than the y-scale and thus, are not visible. The blue circles represent the exact diagonalization, red pluses the noiseless simulations and black crosses the quantum hardware results. . . . . . . . . . . . . . . . . . . 63

5.4 The phase transition point $l_0^*$ as a function of $1/N$ for $x = 7, 9$ and $m_{\text{r}}/g = 0.5$ (a), $1$ (b). The error bars, estimated via the bisection method described in the main text, are smaller than the scale of the y-axis and are therefore not visible. . . . . . . . . . . . . . . . . . . . . . . . . . . . . . . . . . . . . . . . . 66

5.5 Histograms for the absolute errors of the mitigated and unmitigated data for the electric field density (EFD) for the Wilson $(a)$ and the staggered discretization $(b)$ as well as the particle number (PN) for the Wilson fermions $(c)$ and the staggered formulation $(d)$. Blue bars represent the absolute error between the hardware data after zero noise extrapolation (ZNE) and the simulated VQE, while red bars represent the absolute error between unmitigated hardware data and the simulated VQE. Each subplot includes all $N, m_{\text{lat}}/g, l_0$. . . . . . . . . 68

5.6 Electric field density (EFD) $\langle L_{W,S} \rangle$ and particle number (PN) $\langle P_{W,S} \rangle$ against noise factor for zero noise extrapolation (ZNE) on the data (black crosses) obtained from quantum hardware for different parameters specified in the titles of each subplot with Wilson and staggered fermions. The red pluses are noiseless values of the observables and the blue circles are the exact diagonalization results. For the fits we fit a first-order polynomial to either all points (blue continuous line) or to points with noise factor 1, 3 (dashed orange line). We also fit a second order polynomial to all points (green dotted dashed line). The brown triangle is the weighted average of the extrapolated points of these 3 fits. The plots on the left $(a-d)$ are showing examples where the zero noise extrapolation (ZNE) helped take the expectation values measured closer to the noiseless result, while on the right $(e-h)$ we show occasions where the zero noise extrapolation (ZNE) might not be able to improve the result. However, overall the results of the main text indicate that zero noise extrapolation (ZNE) can significantly improve the results. The calculation of the error bars is described within this Appendix and where they are not visible, they are smaller than the markers and y-scale. . . . . . . . . . . . . . . . . . . . . . . . . . . . . . . . . . 69

5.7 Electric field density (EFD) $\langle L_{W,S} \rangle$ against $ag$ to extrapolate to the continuum limit with fixed volume $N/\sqrt{x} = 30$, fixed $m_{\mathrm{r}}/g = 0.01$, using $N = 70, 80, 90, 100$. The continuous orange line is a linear fit and the dashed blue line is a second order polynomial fit. $(a-c)$ is showing Wilson fermions for $l_0 = 0.1, 0.4, 0.6$ respectively and $(d-f)$ the same for staggered fermions with the same $x$ as Wilson fermions and the electric field density (EFD) method for the mass shift (MS) [60]. The error bars emanate from the variational algorithm to compute the relevant ground states and the extrapolation in bond dimension. They are much smaller than the markers and thus, are not visible. 71

5.8 Electric field density (EFD) $\mathcal{F}/g$ against $l_0$ for Wilson fermions and staggered fermions at $m_{\mathrm{r}}/g = 0.01$. The following mean squared error (MSE) values are the mean squared error (MSE) of each of the data as compared to the continuum mass perturbation theory prediction for the electric field density (EFD) $\mathcal{F}/g$ given in Eq. (1.7). For staggered fermions with $\mathrm{MS}_t$ and same $x$ (number of qubits as Wilson), the mean squared error (MSE) is $1.041 \times 10^{-6}$ $(6.16 \times 10^{-7})$, and respectively for $\mathrm{MS}_L$ $6.143 \times 10^{-9}$ $(2.617 \times 10^{-8})$. For Wilson fermions the mean squared error (MSE) is $7.926 \times 10^{-9}$. The error bars emanate from the errors in the variational algorithm to compute the relevant ground states, the extrapolation in bond dimension and in lattice spacing. . . 72

5.9 Electric field density (EFD) $\mathcal{F}/g$ against $l_0$ for Wilson fermions using no mass shift (MS) at $m_\mathrm{r}/g = m_\mathrm{lat}/g = 0.01$. The MSE is calculated as in the main text and found here to be $7.939 \cdot 10^{-4}$. The error bars emanate from the errors in the variational algorithm to compute the relevant ground states, the extrapolation in bond dimension and in lattice spacing. . . . . . . . . . . . . . . . . . . . . . . 73

6.1 Subtracted electric field (SEF) $\Delta F(n)$ per link $n$ as a function of time $t$. The red line on the y-axis represents the initial electric field flux generated by the pair of positive/negative charges shown as plus/minus on the string's endpoints. $(b)$: Subtracted charge $\Delta Q(n)$ per site $n$ as a function of time $t$. In $(b)$ we focus on the early time dynamics and show how the charges forming the initial string spread out. The parameters used are $N = 12$, $x = 1$, $m = 0.5$, $l_0 = 0$, $D = 2$, $T = 10$. . . . . . . . . . . . . . . . . . . . . . . . . . . . . . . . . 77
6.2 Subtracted electric field (SEF) $\Delta F(n)$ of the middle link $n = 5$ as a function of time $t$. The inset zooms in on the early-time dynamics, demonstrating the monotonic decrease of subtracted electric field (SEF) from its initial value to zero, indicating thermalization towards the steady state. The time resolution is fine enough to render the data quasi-continuous, with points connected by lines. This monotonic trend in subtracted electric field (SEF) is key to defining the thermalization time $\mathcal{T}$. . . . . . . . . . . . . . . . . . . . . . . . . . . . . . . . 78
6.3 Thermalization time $\mathcal{T}$ as a function of dissipator strength $D$ and background electric field $l_0$. The parameters are $N = 12$, $x = 1$, $T = 10$, $(a)$: $m = 0.1$, $(b)$: $m = 0.5$, $(c)$: $m = 0.75$, $(d)$: $m = 1$. Each axis contains 20 equidistant points with $D \in [2, 5]$, $l_0 \in [0.0, 0.5]$. All other parameters are as given in Sec. 6.1. Cyan contour lines represent levels of thermalization time $\mathcal{T}$. Increasing $D$, $l_0$, or $m$ results in a higher $\mathcal{T}$. . . . . . . . . . . . . . . . . . . . . . . . . . . . . 79
6.4 $(a)$: Thermalization time $\mathcal{T}$ vs dissipator strength $D$, $(b)$: applied background electric field $l_0$, and $(c)$: mass $m$. The error bars, which are not visible due to the large y-scale, are estimated to be 0.1, as inferred from the data in table 6.1 and discussed in Sec. 6.1.4. The lines are provided as visual aids. . . . . . . . 80
6.5 $(a)$: Subtracted kinetic energy (SKE) $\Delta K$ vs time for $m = 0.1$ and $(b)$: $m = 1.0$ at $N = 12$. The time resolution is fine enough that the data appears quasi-continuous, with points connected by lines. Higher dissipator strength $D$ leads to a lower subtracted kinetic energy (SKE) peak. Insets display a later stage of the time evolution, highlighting the approach to thermalization. . . . . . 80

6.6 Subtracted mutual information (SMI) $\Delta I$ as a function of time $t$ for the parameter sets in the four corners of Fig. 6.3(a, d) at $N = 12$. The mutual information is measured between sites 4,5 and 6,7. The initial string extends between sites 4 to 7, hence the two regions 4,5 and 6,7 measure the mutual information between the two halves of the original string. The inset focuses on the times between 10 and 20 to emphasize how fast the subtracted mutual information (SMI) of each parameter set decreases. The resolution in $t$ is fine enough that the data is quasi-continuous and connected with lines. . . . . . . 82

6.7 Thermalization time $\mathcal{T}$ as a function of the environment's temperature $T$ for $N = 12$, $D = 2, 5$, $l_0 = 0.0, 0.5$, $m = 0.1, 1.0$. The error bars, which are not visible due to the y-scale of the plot, are estimated to be 0.1 as inferred from the data in table 6.1 and discussed in Sec. 6.1.4. The lines represent the fit described by Eq. (6.3). . . . . . . . . . . . . . . . . . . . . . . . . . . . . . . . . 84

6.8 $(a)$: Subtracted kinetic energy (SKE) $\Delta K$, $(b)$: particle number (PN) $\mathcal{P}$ for the case where the initial state is the Dirac vacuum with the string present $\mathcal{P}$ $(b)$, both as a function of time $t$. In $(a)$ the legend gives the value of $\Delta K$ at the peak and in $(b)$ the legend gives the final value of $\mathcal{P}$ at time $t = 100$. The comparison is drawn between temperatures $T = 7$ and $T = 100$. The bottom two subplots $(c)$, $(d)$ show the subtracted electric field (SEF) $\Delta F(n)$ as a function of the link number $n$ and time $t$ for $T = 7, 100$ respectively. All plots have fixed parameters $N = 12$, $D = 5$, $l_0 = 0.5$ and $m = 1.0$. . . . . . . 86

6.9 Subtracted mutual information (SMI) $\Delta I$ as a function of time $t$ for $D = 5.0$, $m = 1.0$, $l_0 = 0.5$ and $T \in [7, 100]$. Inset $(a)$ focuses on the peak of $\Delta I$ and inset $(b)$ on the order at which different temperatures decrease to the steady state value $\Delta I = 0$ in late times. . . . . . . . . . . . . . . . . . . . . . . . . . . . 87

6.10 Subtracted electric field (SEF) $\Delta F(n)$ per link number $n$ as a function of time $t$ for $N = 12, 24$, with parameter values $l_0 = 0.0, 0.5$, $D = 2.0, 5.0$, and $m = 0.1, 1.0$. Additional parameter details are provided in Section 6.1. The subtracted electric field (SEF) approaches zero upon thermalization, and the data indicate that increasing $D$, $l_0$, and $m$ results in longer thermalization times. Doubling the system size further mitigates boundary effects. . . . . . . 88

6.11 $(a)$: Subtracted electric field (SEF) $\Delta F(n)$ per link number $n$ over time $t$ for $N = 100$, $D = 0.15$, $x = 4$, $m = 0$, $\tau = 0.001$. $(b)$: Close-up of the middle region of subplot $(a)$. $(c)$: Absolute subtracted electric field (SEF) difference between symmetric link pairs, $P = |\Delta F(n = i) - \Delta F(n = N - i - 2)|$, for $i \in [0, 48]$, using data from $(a)$. The algorithm preserves reflection symmetry around the central link with an average accuracy of $\mathcal{O}\left(10^{-4}\right)$. The darkest line corresponds to the link pair closest to the center, while the brightest line represents the first and last links. . . . . . . . . . . . . . . . . . . . . . . . . . . . . . . . . 90

6.12 $(a)-(c)$: Subtracted electric field (SEF) of the Schwinger boson, $\Delta F_B(n)$, per link number $n$ as a function of time $t$ for $D = 2, 3.5, 5$. $(d)$: Comparison of thermalization time measured using the subtracted electric field (SEF) ($\mathcal{T}_{\Delta F_B}$) and the subtracted energy ($\mathcal{T}_{\Delta E_B}$) as a function of the dissipator strength $D$. $(e)$, $(f)$: Time evolution of subtracted electric field (SEF) and subtracted energy, respectively, for different values of $D$. The insets highlight the long-time behavior. In $(e)$ and $(f)$, individual data points are omitted for clarity, as the time steps are finely spaced. . . . . . . . . . . . . . . . . . . . . . . . . . . . . . . 91

6.13 $(a)$: Time evolution of the subtracted particle number (SPN) $\Delta\mathcal{P}_B$ for the Schwinger boson. $(b)$: Evolution of the subtracted kinetic energy (SKE), $\Delta K_B$. Both plots demonstrate how increasing the dissipator strength $D$ slows the thermalization process. The insets highlight the long-time behavior. Individual data points are omitted for clarity due to the fine time resolution. . . . . . . 92

# List of Tables

5.1 This table corresponds to the absolute error with respect to the results from mass perturbation theory for the data presented in the main text. For staggered fermions that use the theoretically predicted mass shift (MS), $\mathrm{MS}_t$, the error tends to grow with $l_0$ due to the fact that the $\mathrm{MS}_t$ does not account for an $l_0$ dependence. . . . . . . . . . . . . . . . . . . . . . . . . . . . . . . . . . . . . 72

6.1 Thermalization times for different parameters at $N = 12$ and $N = 24$. Other parameter values are provided in Section 6.1. . . . . . . . . . . . . . . . . . . . . 89

# List of Abbreviations

**ATD-DMRG** adaptive time-dependent DMRG

**CP** charge conjugation - parity

**cVQE** concurrent variational quantum eigensolver

**DMRG** density matrix renormalization group

**EFD** electric field density

**L-BFGS-B** limited-memory Broyden-Fletcher-Goldfarb-Shanno with box constraints

**LCF** left canonical form

**LGT** lattice gauge theory

**LHC** large hadron collider

**MCF** mixed canonical form

**MPO** matrix product operator

**MPS** matrix product state

**MS** mass shift

**MSE** mean squared error

**NISQ** noisy intermediate-scale quantum

**OBC** open boundary condition

**OQS** open quantum system

**PN** particle number

**PQC** parameterized quantum circuit

**QBM** quantum Brownian motion

**QC** quantum computing

**QCD** quantum chromodynamics

**QED** quantum electrodynamics

**QFT** quantum field theory

**QGP** quark gluon plasma

**QMBP** quantum many-body physics

**RCF** right canonical form

**RHIC** relativistic heavy ion collider

**SEF** subtracted electric field

**SKE** subtracted kinetic energy

**SMI** subtracted mutual information

**SPN** subtracted particle number

**SVD** singular value decomposition

**TN** tensor network

**TREX** twirled readout error extinction

**VQE** variational quantum eigensolver

**ZNE** zero noise extrapolation

# Introduction

The Standard Model, which describes three of the four fundamental forces of nature, has achieved unprecedented success, particularly in predicting particles such as the Higgs, W, and Z bosons before their experimental confirmation [1–3]. Moreover, it provides exceptionally precise theoretical predictions for the masses of these bosons [4–6], as well as for the magnetic moment of the electron [7]. It also offers powerful tools to investigate matter under extreme conditions, such as quarkonia in the quark gluon plasma (QGP) [4, 8–10], providing a unique window into fundamental physics, including the nature of the strong force and the conditions of the early universe. However, the Standard Model has limitations, particularly in explaining the matter-antimatter asymmetry, which is closely related to the strong charge conjugation - parity (CP) problem in quantum chromodynamics (QCD) [11–14]. The strong CP problem questions why QCD preserves CP symmetry to an extraordinary degree, despite theoretical expectations that it could be significantly violated. More specifically, the neutron electric dipole moment within QCD incorporating a topological $\theta$-term is given by $d_N = (5.2 \times 10^{-16} e \cdot \mathrm{cm})\,\theta$, with the experimental constraint $d_N < 10^{-26} e \cdot \mathrm{cm}$, leading to the bound $\theta < 10^{-10}$. Since a nonzero $\theta$ parameter explicitly breaks CP symmetry and theoretically spans the range $[0, 2\pi]$, the strong CP problem fundamentally concerns why it is so fine-tuned near $\theta = 0$. This fine-tuning is connected to the observed matter-antimatter asymmetry, as one of the necessary conditions for generating the baryon asymmetry of the universe is CP violation [15].

These limitations motivate both extensions of the Standard Model and deeper analyses of its existing content. To explore regimes in which analytical perturbation theory is not applicable, lattice gauge theory (LGT) has been developed as a powerful framework to probe strongly interacting theories such as QCD [16, 17], or even QCD+quantum electrodynamics (QED) [18–20]. To simulate LGTs, the Monte Carlo algorithm within the Lagrangian formulation has been a widely used and successful approach [16, 18, 21, 22], leading to significant progress, including precise determinations of the anomalous magnetic moment of the muon [23], quark masses [18], and many other observables. However, Monte Carlo methods face the well-known sign problem [24, 25], which presents severe challenges in regions of the QCD phase diagram with finite temperature and baryon density, as well as in real-time dynamics [26, 27]. Several strategies have been proposed to mitigate this problem, including dualization techniques and density-of-states approaches [28].

Promising alternative approaches to tackle these challenges are tensor networks (TNs) [29, 30] and quantum computing (QC) [31–33] techniques, which rely on the Hamiltonian formulation and naturally circumvent the sign problem [25]. On the one hand, TNs have already demonstrated promising results in LGT, both for real-time dynamics and spectrum exploration [34–36]. However, they are limited in their ability to represent quantum states with large entanglement entropy or to efficiently scale to higher spatial dimensions [37, 38], where QC methods offer a more natural representation. Quantum computers inherently leverage quantum mechanics in their simulations, avoiding theoretical constraints on the types of quantum states they can efficiently represent [39]. Nevertheless, in practice, both TNs and QC have their own limitations, necessitating the continuous development of new techniques within their respective frameworks.

To this end, the Schwinger model, which represents 1+1 dimensional QED, has been widely employed as a benchmark for developing and testing novel numerical techniques [40–53]. One of its key attractions is its structural similarity to QCD, exhibiting features such as confinement, chiral symmetry breaking, the axial anomaly, a mass gap, and strong-coupling behavior [54–57]. Despite these similarities, the Schwinger model is of significant interest in its own right, as will be explored in this thesis. For instance, it provides a theoretical setting to study the Sauter–Schwinger effect [45], which describes fermionic pair production in strong electric fields and has experimental relevance in high-intensity laser physics [58].

The objectives of this thesis are to utilize the Schwinger model, specifically in the presence of a topological $\theta$-term representing a background electric field, as a platform for advancing TN and QC simulations. In particular, we first address the challenge of mass renormalization within LGT and develop, for the first time within the Hamiltonian formulation, techniques for measuring the mass shift (MS), applicable to both TNs and QC. These techniques play a crucial role in the extrapolation of observables to the continuum limit, enabling meaningful comparisons with high-energy experimental results. Further, we aim to demonstrate the capabilities of QC in probing the phase diagram of LGTs, while showcasing the effectiveness of stacked error mitigation techniques on noisy intermediate-scale quantum (NISQ) devices. These devices, characterized by their limited number of qubits and susceptibility to noise and decoherence, require careful error handling and resource estimation to assess their near-term capabilities. Finally, this thesis explores the Schwinger model within the framework of open quantum system (OQS) to investigate the thermalization of mesonic states in a hot environment, such as the Schwinger boson state and the state consisting of an electric field flux string. This study emulates the dynamics of quarkonia in the QGP, which is of significant relevance to our understanding of the early universe and experimental facilities such as those at the large hadron collider (LHC) and relativistic heavy ion collider (RHIC).

The chapters of this thesis are organized as follows:

**Chapter 1** - This chapter introduces the theoretical background, starting with the continuum Schwinger model, its phase diagram, and quantum anomalies, as well as results from mass perturbation theory. It then discusses the fermion doubling problem and outlines two discretization approaches used to address it: Wilson and staggered fermions. Finally, we introduce the theory of OQS, focusing specifically on aspects relevant to this thesis, including the Markovian Lindblad master equation in the quantum Brownian motion (QBM) limit.

**Chapter 2** - This methods chapter provides a comprehensive introduction to matrix product states (MPSs) and their properties. It then discusses matrix product operators (MPOs), followed by descriptions of the density matrix renormalization group (DMRG) and adaptive time-dependent DMRG (ATD-DMRG) algorithms for ground-state search and time evolution, respectively.

**Chapter 3** - The second methods chapter covers key concepts in QC. It begins by explaining quantum circuits and measurement techniques, followed by a detailed discussion of the variational quantum eigensolver (VQE) algorithm for ground-state search. The chapter also explores various error mitigation techniques.

**Chapter 4** - This results chapter, based on [53, 59, 60], presents our methodology for measuring the MS of the Schwinger model and investigates its dependence on system parameters. We perform a continuum extrapolation of observables and compare them with mass perturbation theory predictions. Additionally, we contrast our MS measurement approach for staggered fermions with theoretical predictions.

**Chapter 5** - This chapter, based on [61], demonstrates the capability of QC in simulating the first-order phase transition of the Schwinger model by utilizing the current IBM quantum hardware. We analyze the VQE algorithm's effectiveness, identifying the best ansatz and optimal gate choices. Furthermore, we employ state-of-the-art error mitigation techniques, assess their performance, and perform continuum extrapolations using MPSs to estimate the quantum resources needed for future large-scale simulations.

**Chapter 6** - The final results chapter, based on [62], investigates the thermalization of mesonic states in a hot environment. It explores the Schwinger model as an OQS and examines how the thermalization time of these states depends on various parameters. Additionally, we establish connections between quantum mutual information and thermalization time, highlighting their correlation.

**Conclusion** - The thesis ends with a conclusion on the methods and results presented throughout. Further, we also provide an outlook on the various topics explored in the sections of results.

# 1 Theory

In this section we will discuss the physics of the continuum Schwinger model starting in Sec. 1.1. The Schwinger model describes quantum electrodynamics (QED) in 1+1 dimensions and has been the subject of intense study due to its relevance to both theoretical and experimental physics. One of the main reasons for its appeal is that it shares many similarities with quantum chromodynamics (QCD), such as confinement, charge screening, and chiral symmetry breaking in the massless limit [55, 63]. These phenomena are crucial for understanding the non-perturbative aspects of QCD, and the Schwinger model provides a simplified framework for studying them in a lower-dimensional setting. For instance, due to confinement, the fundamental particle of the Schwinger model's spectrum is the Schwinger boson, an fermion-antifermion bound state, as opposed to individual fermions. This is analogous to the case in QCD, where quark confinement leads to the formation of hadrons like pions, which are composed of quark-antiquark pairs [64].

It is also an interesting model in its own right, first of all because it is one of only a few quantum field theories with an exact solution in both the massless and large mass limits [65]. Furthermore, it is relevant to the study of experimentally interesting phenomena such as the Sauter–Schwinger effect, which describes the pair production of fermions in the presence of a strong electric field [45, 66]. This effect has been the subject of active research in both high-energy physics and ultracold atomic systems [67], with recent studies focusing on its possible experimental observation in quantum simulations.

Recent advances in quantum simulation have enabled the realization of the Schwinger model on platforms such as superconducting qubits [61, 68–75], ultracold atoms [76–80], and trapped ions [81–84], providing the opportunity to explore fermion confinement, chiral symmetry breaking, and other non-perturbative phenomena [85, 86]. These quantum simulators offer highly controllable environments where parameters such as the coupling constant, fermion mass, and gauge fields can be finely tuned to simulate the dynamics of the Schwinger model. For instance, trapped ions have been used to simulate QED in 1+1 dimensions, enabling the study of the model's vacuum structure and the role of gauge field interactions in fermion dynamics [85]. Ultracold atoms in optical lattices have also been employed to simulate the Schwinger model, providing insights into the physics of confinement and topological effects in low-dimensional systems [86]. These platforms form the onset for future studies of high-energy phenomena in synthetic quantum matter.

In the sections following, the fermion doubling problem is presented in Sec. 1.2, which arises from discretizing the spatial dimension on a lattice. Sections 1.3 and 1.4 outline two possible solutions to the doublers, namely the Hamiltonian formulations of Wilson and staggered fermions. Finally, in Sec. 1.5 we describe the theory behind the Schwinger model as an open quantum system (OQS), which is relevant to the study of Ch. 6.

## 1.1. Continuum Schwinger model

The Schwinger model with one fermion flavour in the continuum is described by the Hamiltonian density [46, 53, 55, 56, 60, 61, 87]

$$\mathcal{H} = -i\overline{\psi}\gamma^1 \left(\partial_1 - igA_1\right)\psi + m\overline{\psi}\psi + \frac{1}{2}\left(\dot{A}_1 + \frac{g\theta}{2\pi}\right)^2, \tag{1.1}$$

where the temporal gauge $A_0 = 0$ [88] is used. The physical states of this Hamiltonian need to obey the constraint of Gauss's law [89, 90]

$$\partial_1 \dot{A}_1 = -g\psi^\dagger\psi. \tag{1.2}$$

The first term in Eq. (1.1) is the kinetic term, which involves the two-component Dirac spinor $\psi(x)$ describing fermionic matter. This operator satisfies the standard fermionic anti-commutation relations $\{\psi^\dagger_\alpha(x), \psi_{\alpha'}(y)\} = \delta(x-y)\delta_{\alpha\alpha'}$ [91], with the spinor indices $\alpha, \alpha'$ now shown explicitly. By the definition $\overline{\psi} \equiv \psi^\dagger\gamma^0$, this term involves the two-dimensional matrices $\gamma^\mu$ with $\mu = 0, 1$, which satisfy the Clifford algebra [92] $\{\gamma^\mu, \gamma^\nu\} = 2\eta^{\mu\nu}$, where the metric is $\eta^{\mu\nu} = \mathrm{diag}(1, -1)$.

The next term involves the coupling $g$ between the fermionic operator $\psi$ and the gauge field operator $A_\mu$. Given our choice for the temporal gauge $A_0 = 0$, only the $\mu = 1$ component is present in the Hamiltonian. This is a vector gauge field operator that makes the Hamiltonian invariant under the local gauge transformation [93, 94]

$$\begin{aligned} &\psi \to e^{if(x)}\psi \\ &A_1 \to A_1 + \frac{\partial_1\left(f(x)\right)}{g}. \end{aligned} \tag{1.3}$$

The global transformation with the generic phase function $f$ independent of $x$ leads to the conservation of electrical charge through Noether's theorem [91, 95]. This means we can group the states of the Hilbert space into subspaces of a given total electric charge and the physical subspace is the one with zero total electrical charge [54]. This can also be understood intuitively using Gauss's law. Take a one dimensional space and set a positive charge $g$ in the middle. Then form a Gaussian surface around this charge, which in one dimension consists of two points on each side of the charge. Using Gauss's law, that states the electric field flux out of the Gaussian surface equals the charge enclosed, we find the electric field is constant throughout the space having the value $g/2$. This shows that states with non-zero total charge will have an electric field which does not decay to zero as $x$ tends to $\pm\infty$, leading to an infinite electric field energy.

The third term in the Hamiltonian is the mass term defining the bare mass $m$ while the final two terms involve the electric field energy density. In this last term the first part of the bracket represents the dynamical electric field energy density while the second part represents a static background electric field energy density [46, 56, 57]. This is a topological term involving the topological $\theta$ parameter defined between $[0, 2\pi)$ [60, 96].

This last last term enriches the phase diagram of the model with first and second order phase transitions which we turn to next.

Regarding the ground state in the limit of large mass in units of the coupling $m/g \gg 1$, where we can neglect the kinetic energy, it is energetically less probable to have charged particles present when the background electric field is small [96]. In this first case, the only energy contribution will come from the background electric field. A second case emerges as we increase the background electric field, since there is a $\theta$ value which makes it energetically favourable to produce a negative-positive charge pair separated by a distance $\Delta x$ that screens the original background electric field to reduce the overall energy. Let the one dimensional spatial dimension extend from $A$ to $B$ and define $l_0 \equiv \theta/2\pi$. Using Gauss's law we also know that a unit charge produces an electric field magnitude of $|E| = g/2$ [96]. The two different cases above, also shown in Fig. 1.1 as case 1 and 2, have respectively a total energy in units of the coupling given by

$$\text{Case 1:} \quad \int \frac{|E|^2}{2g} dx = g l_0^2 (B - A) \tag{1.4}$$

$$\text{Case 2:} \quad \int \frac{|E|^2}{2g} dx = \frac{g l_0^2}{2} (B - A - \Delta x) + \frac{g \left(l_0 - 1\right)^2}{2} \Delta x, \tag{1.5}$$

where we renormalize the energy of the Dirac sea to zero and assume no particles are present in this large mass limit [96]. A separation $\Delta x = B - A$ minimizes the energy of case 2. By equating the above two cases, we find that the transition happens at $\theta = \pi$. At this value of $\theta$ the combined action of charge conjugation - parity (CP) is a symmetry of the Hamiltonian Eq. (1.1) which then gets spontaneously broken when the system chooses one of the two cases of degenerate vacuum states [96, 97]. Away from this $\theta$ value, the CP transformation is not a symmetry, as the topological $\theta$ term is antisymmetric under this transformation [97]. Lowering the mass, we find a critical mass around $m/g \approx 0.33$ [96], where the first-order phase transition line ends with a second order phase transition point, as shown in Fig. 1.2, after which there is a unique vacuum state [56, 96, 97] and the CP symmetry is restored. In this small mass limit we have analytical results from mass perturbation theory [55]. The particle spectrum does not consist of fermions but rather a massive meson called the Schwinger boson. In the massless limit, this boson is free and the higher excited states are just free $n$-particle excitations of this boson. In the massive case, the boson becomes interacting so the excited

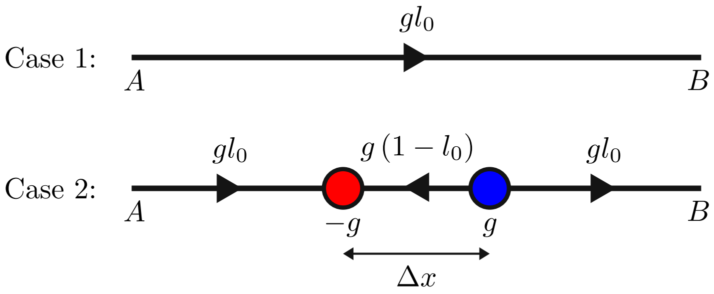

**Figure 1.1:** *Working in the large mass limit, the top line shows the configuration for case 1 of Eq.* (1.4) *which is a state in the absence of electrical charges and with only a background electric field* $gl_0$ *present. For case 2 in Eq.* (1.5), *the bottom line shows the case of a negative-positive charge pair set a distance* $\Delta x$ *apart.*

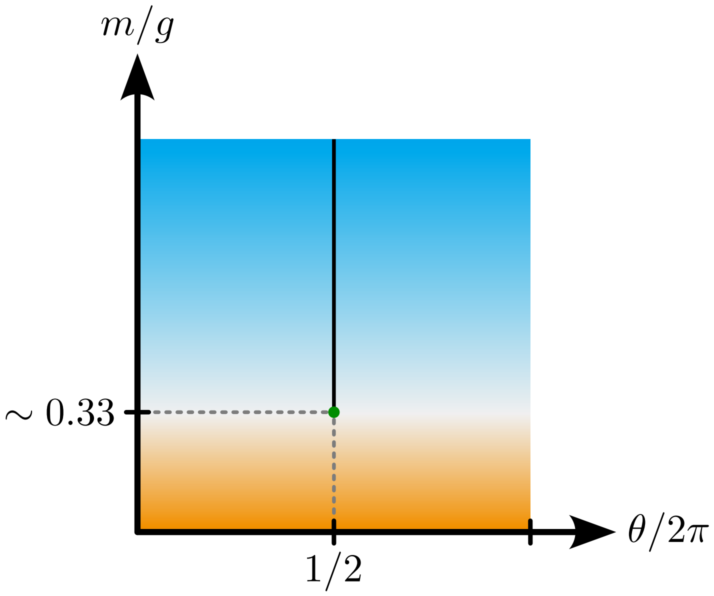

**Figure 1.2:** *Illustration of the phase diagram of the Schwinger model in the presence of a topological term in the* $m/g - \theta$ *plane. Since the physics is periodic in* $\theta$ *with period* $2\pi$, *only the first period is shown. The critical line (shown in black) indicates the first-order phase transitions occurring at* $\theta = \pi$ *for masses larger than the critical one* $m_c/g \approx 0.33$, *which ends in a second-order phase transition (green dot) exactly at* $m_c/g$. *Below the critical mass no transitions occur.*

states are $n$-boson bound states [56].

Two important results derived within mass perturbation theory are the mass of this Schwinger boson and the vacuum expectation value of the electric field density given respectively in units of the coupling by [55]

$$\frac{M_S}{g} = \frac{1}{\sqrt{\pi}}\left(1 + 3.5621\sqrt{\pi}\left(\frac{m}{g}\right)\cos\theta + \pi\left(5.4807 - 2.0933\cos\left(2\theta\right)\right)\left(\frac{m}{g}\right)^2\right)^{1/2} \tag{1.6}$$

$$\frac{\mathcal{F}}{g} = \frac{e^{\gamma}}{\sqrt{\pi}}\left(\frac{m}{g}\right)\sin\theta - 8.9139\,\frac{e^{2\gamma}}{4\pi}\left(\frac{m}{g}\right)^2\sin\left(2\theta\right). \tag{1.7}$$

We can also learn a lot about the theory by looking at the quantum axial anomaly which we will explain now. For this, and for Sec. 1.2, we will use the interchangeably equivalent to the Hamiltonian, which is the Lagrangian, related to the Hamiltonian by a Legendre transformation. The Lagrangian density of the model is given by

$$\mathcal{L} = \bar{\psi}(i\partial\!\!\!/ - gA\!\!\!/ - m)\psi - \frac{1}{4}F_{\mu\nu}F^{\mu\nu} + \frac{g\theta}{4\pi}\epsilon^{\mu\nu}F_{\mu\nu}. \tag{1.8}$$

At the classical level, this Lagrangian is symmetric under the axial transformation $\psi \to \psi' = e^{i\gamma_5\beta}\psi$ when $m = 0$ for any real angle $\beta$.

The quantum theory can be described by the partition function [93, 94, 98]

$$Z[m,\theta] = \int \mathcal{D}A\mathcal{D}\bar{\psi}\mathcal{D}\psi\; e^{iS[A,\bar{\psi},\psi,m,\theta]}, \tag{1.9}$$

where the action is defined as $S = \int d^2x\,\mathcal{L}$. This quantum theory does not preserve axial symmetry, even when $m = 0$. When a symmetry present at the classical level is not preserved at the quantum level, it is referred to as a quantum anomaly.

The anomaly originates from the transformation of the path integral measure $\mathcal{D}\psi$, which acquires a contribution from a Jacobian factor $J$ [98]:

$$J = \exp\left(-i\int d^2x \frac{g\beta}{4\pi}\epsilon^{\mu\nu}F_{\mu\nu}\right). \tag{1.10}$$

This factor can be derived using the Fujikawa method [98, 99]. Since both $\mathcal{D}\psi$ and $\mathcal{D}\bar{\psi}$ acquire the same factor, the full measure transforms by a factor of $J^2$.

Equipped with this factor we are able to show that $Z[m = 0, \theta]$ is identical to $Z[m = 0, \theta =$

0] [60],

$$
\begin{aligned}
Z[m=0,\theta] &= \int \mathcal{D}A\mathcal{D}\bar{\psi}\mathcal{D}\psi \; e^{iS[A,\bar{\psi},\psi,\theta]} \\
&= \int \mathcal{D}A\mathcal{D}\bar{\psi}'\mathcal{D}\psi' \; e^{iS[A,\bar{\psi},\psi,\theta]} \\
&= \int J^2\mathcal{D}A\mathcal{D}\bar{\psi}\mathcal{D}\psi \; e^{iS[A,\bar{\psi},\psi,\theta]} \\
&= \int \mathcal{D}A\mathcal{D}\bar{\psi}\mathcal{D}\psi \; e^{iS[A,\bar{\psi},\psi,\theta]-i\int d^2x \frac{g\beta}{2\pi}\epsilon^{\mu\nu}F_{\mu\nu}} \\
&= Z[m=0,\theta=0],
\end{aligned}
\tag{1.11}
$$

which implies that in the massless limit, the parameter $\theta$ is unphysical and can be transformed out of the theory [46, 56, 60, 96]. In the second equality of Eq. (1.11), the symmetry of the action at $m = 0$ under the axial transformation was used. In the last equality, we have set $\beta = \theta/2$ which cancels the $\theta$ term present in the original action. For the massive case, we would have found that $Z[m, \theta]$ is identical to $Z[-m, \theta + \pi]$ which comes from the mass term acquiring the factor $e^{2i\gamma_5\beta}$ under the axial transformation. In the second exponent term of the fourth line in Eq. (1.11), excluding the prefactor $i2\beta = i\theta$, we have the topological charge, which takes only integer values [56]. Thus, the quantum theory is symmetric under $\theta \to \theta + 2\pi$, just as any observable of the theory [46, 56, 60].

In summary, we have introduced the Schwinger model with one fermion flavour in the continuum, and in the next section we will start discussing the procedure to discretize this model on a lattice. We have looked at the axial anomaly, which shows how the $\theta$ parameter becomes unphysical in the massless limit and that observables are periodic in $\theta$ with a period of $2\pi$. These results are further confirmed by the analytical results from mass perturbation theory on the mass of the fundamental particle of the theory and the electric field density. We make extensive use of all of these insights in Ch. 4. Further, we have described the phase diagram of the model with a first-order phase transition line ending at a second order phase transition point. This takes the theory from a CP-violating phase at large mass to a phase of CP-symmetric phase for small mass. In Ch. 5, we explore this phase diagram with IBM's superconducting quantum computers.

## 1.2. Fermion doubling problem

In order to perform numerical simulations we need to discretize our model on a finite lattice. For fermions, this causes the fermion doubling problem which we will demonstrate in this section using a single massless free fermion in 1+1 dimensions [98, 100–102]. The action in the continuum

$$
S = \int d^2x \left( i\bar{\psi}\gamma^\mu\partial_\mu\psi \right), \tag{1.12}
$$

can be discretized with the forward, backward or symmetric discrete derivative. The first two will break charge, parity and Euclidean time reversal symmetries [101], so let us take the symmetric discrete derivative. The action becomes

$$S = a^2 \sum_{x\in\Gamma} i\overline{\psi}(x) \sum_{\mu} \gamma^{\mu} \left( \frac{\psi\left(x + a\hat{\mu}\right) - \psi\left(x - a\hat{\mu}\right)}{2a} \right), \tag{1.13}$$

where the sum runs over all lattice points $\Gamma$ and $\hat{\mu}$ is the unit vector in the temporal and spatial directions. If we Fourier transform this expression we have

$$S = a \sum_{k} \overline{\psi}_{-k} D(k) \psi_k, \tag{1.14}$$

where the range of $k_\mu$ in each direction is $k_\mu \in \left[-\frac{\pi}{a}, \frac{\pi}{a}\right)$ with the endpoints identified and $D(k)$ is called the inverse propagator given by

$$D(k) = \sum_{\mu} \gamma^{\mu} \sin\left(k_\mu a\right). \tag{1.15}$$

The poles of the propagator, i.e. the zeros of the inverse propagator in Eq. (1.15), specify how many fermion modes the lattice theory consists of [101]. In this case we find the physical one at $k_\mu = 0$ but also find further 3 unphysical ones, called the doublers, at $k = [0, \pi/a], [\pi/a, 0], [\pi/a, \pi/a]$. More generally for every direction we discretize, we will have a factor of 2 more fermion modes when we only started with one [98, 101, 102].

This is a consequence of the Nielsen-Ninomiya theorem [103] which states that the discretization of the massless free Dirac operator with the following properties does not exist:

1. $\{\gamma^5, D\} = 0$.
2. $D(x, y)$ has translational symmetry, i.e. $D(x, y) = D(x - y, 0)$.
3. $D(z, 0)$ decays faster than any inverse power of $|z|$ for $|z| \to \infty$.
4. $D$ is free of doublers.

Point 1 is equivalent to the statement that $D$ is a linear combination of the $\gamma$ matrices where we have defined $\gamma^5 = \gamma^0\gamma^1$. In the following sections we will look at Wilson and staggered fermions which avoid point 4 at the expense of breaking points 1 and 2 respectively.

## 1.3. Wilson fermions

One way to resolve the fermion doubling problem is to use the Wilson fermion discretization scheme [101, 102, 104]. In this thesis we will be focusing on the Hamiltonian formulation, therefore we focus on this formulation here as well.

To implement Wilson fermions we add the following term [104]

$$\Delta H = -r\frac{a^2}{2} \sum_{n} \overline{\psi}_n \left(\partial_1\right)^2 \psi_n, \tag{1.16}$$

to the free massive Dirac Hamiltonian

$$H_{\text{free}} = a \sum_n \overline{\psi}_n \left( -i\gamma^1 \partial_1 + m_{\text{lat}} \right) \psi_n . \tag{1.17}$$

In Eq. (1.16), $r$ is the Wilson parameter commonly set to one [105], $a$ is the lattice spacing, $n$ is the spatial lattice site index, and the sum runs over all spatial lattice sites. Choosing the symmetrized discrete first and second derivative for Eq. (1.17) and Eq. (1.16) respectively, we have the Wilson fermions free massive Dirac Hamiltonian

$$H_{\text{W}} = \sum_n \left( -\overline{\psi}_n \left( \frac{r + i\gamma^1}{2} \right) \psi_{n+1} + \overline{\psi}_n \left( \frac{-r + i\gamma^1}{2} \right) \psi_{n-1} + (am_{\text{lat}} + r)\, \overline{\psi}_n \psi_n \right) . \tag{1.18}$$

The chiral symmetry $\psi \to e^{i\gamma^5 \beta}$ for some real angle $\beta$ is broken explicitly by Wilson fermions even in the massless limit, which in turn causes an additive mass renormalization [60, 102, 106]. Therefore, in Eq. (1.18) we use $m_{\text{lat}}$ as the lattice mass which differs from the renormalized mass by an additive shift and which is the main focus of the study in Ch. 4.

Since we are in 1+1 dimensions and discretize only the spatial dimension we have one doubler that Wilson fermions have to eliminate. Through the addition of the term in Eq. (1.16) the mass of the doubler becomes inversely proportional to $a$ which then becomes infinitely heavy towards the continuum limit $a \to 0$ and thus decouples from the theory [107]. A way to see this is to apply the Fourier transform to Eq. (1.18) which gives

$$H_W = \sum_k \left( \psi_k^\dagger \gamma^0 \psi_k \left( m_{\text{lat}} + r \left( \frac{2}{a} \sin^2 \left( \frac{ka}{2} \right) \right) \right) + \frac{1}{a} \psi_k^\dagger \gamma^0 \gamma^1 \psi_k \sin(ka) \right) . \tag{1.19}$$

We can read off from this equation an effective lattice mass $m_{\text{eff}} = m_{\text{lat}} + r \left( \frac{2}{a} \sin^2 \left( \frac{ka}{2} \right) \right)$. At $k = 0$ we get the expected $m_{\text{eff}} = m_{\text{lat}}$ and for the doubler at $k = \pi/a$ we have $m_{\text{eff}} = m_{\text{lat}} + \frac{2r}{a}$, which is the result we set out to show.

For the rest of this section we will continue the derivation to reach the Hamiltonian for the Schwinger model [60, 69, 108]. The first step is to gauge the theory such that it is locally $U(1)$ symmetric. For this we introduce the link operator $U_n$ placed on the link between the sites at $n$ and $n + 1$. The conjugate field to $U_n$ is the electric field $E_n$ also placed on the links and satisfies the commutation relations $[E_n, U_{n'}] = g\delta_{n,n'} U_{n'}$. With these gauge field operators introduced we have

$$\begin{aligned} H_W = \sum_n \Bigg( &-\bar{\psi}_n \left( \frac{r + i\gamma^1}{2} \right) U_n \psi_{n+1} + \bar{\psi}_n \left( \frac{-r + i\gamma^1}{2} \right) U_n^\dagger \psi_{n-1} \\ &+ (am_{\text{lat}} - r)\bar{\psi}_n \psi_n + \frac{a}{2} \left( E_n + \frac{g\theta}{2\pi} \right)^2 \Bigg) , \end{aligned} \tag{1.20}$$

where the background electric field $gl_0 = g\theta/2\pi$ was explicitly considered. This Hamiltonian is now invariant under the gauge transformation

$$\begin{aligned}\psi_n &\to e^{i\beta_n}\psi_n \\ U_n &\to e^{i\beta_n}U_n e^{-i\beta_{n+1}},\end{aligned} \tag{1.21}$$

which is the discrete counterpart of Eq. (1.3). We introduce for the convenience of numerical simulations the dimensionless operators $L_n = E_n/g$ and $\phi_{n,\alpha} = (-1)^n\sqrt{a}\psi_{n,\alpha}$ while rescaling $H_W \to \left(2/ag^2\right) H_W$. We also have the discrete counterpart of Gauss's law from Eq. (1.2)

$$L_n - L_{n-1} = Q_n \tag{1.22}$$

$$Q_n = a\psi_n^\dagger\psi_n - 1 \tag{1.23}$$

where $Q_n$ is the discrete charge operator and $\sum_n Q_n$ a conserved quantity [60]. In this thesis we will be using open boundary conditions (OBCs) and with this boundary conditions the constrain in Eq. (1.22) can be solved iteratively

$$L_n = \epsilon_0 + \sum_{k=0}^{n} Q_k. \tag{1.24}$$

Here $\epsilon_0$ is the electric field on the left boundary which we set to zero as it will just shift the value of the free parameter $l_0$. The solution in Eq. (1.24) combined with a unitary transformation on the fermionic operators [109] replaces the gauge field operators $U_n, L_n$ with the fermionic degrees of freedom. Further, we perform an additional transformation $\phi_{n,\alpha} \to (-1)^n(-i)^\alpha\phi_{n,\alpha}$ which makes the Hamiltonian purely real [61].

For further convenience we map the fermionic operators to spin-1/2 operators using the mapping [61]

$$\phi_{n,\alpha} \to \chi_{2n-\lfloor\frac{\alpha}{2}\rfloor+1}, \tag{1.25}$$

where $\lfloor\cdot\rfloor$ is the floor function to the nearest integer greater than the input, and the Jordan-Wigner transformation $\chi_n = \prod_{k<n}(iZ_k)\sigma_n^-$ [110]. Choosing $\gamma^0 = X, \gamma^1 = iZ$, the charge operator then becomes

$$Q_n = (Z_{2n} + Z_{2n+1})/2 \tag{1.26}$$

To ensure the ground state is in the zero total charge sector, we add a penalty term $\Lambda$ to the Hamiltonian, $H \to H + \Lambda$, where $\Lambda = \lambda\left(\sum_{n=0}^{N-1} Q_n\right)^2$. With a large enough $\lambda$, we can ensure the ground state is in the sector with vanishing total charge. Putting everything together and with a few algebraic manipulations on nested sums the resulting final Hamiltonian is given by [61]

$$
\begin{aligned}
H_W = {} & x(r-1)\sum_{n=0}^{N-2}\left(\sigma^+_{2n}Z_{2n+1}Z_{2n+2}\sigma^-_{2n+3}+\text{h.c.}\right) \\
& + \frac{x(r+1)}{2}\sum_{n=0}^{N-2}\left(X_{2n+1}X_{2n+2}+Y_{2n+1}Y_{2n+2}\right) \\
& + \left(\frac{m_{\text{lat}}}{g}\sqrt{x}+xr\right)\sum_{n=0}^{N-1}\left(X_{2n}X_{2n+1}+Y_{2n}Y_{2n+1}\right) \\
& + \frac{1}{2}\sum_{n=0}^{2N-1}\sum_{k=n+1}^{2N-1}\left(N-\left\lceil\frac{k+1}{2}\right\rceil+\lambda\right)Z_nZ_k \\
& + l_0\sum_{n=0}^{2N-3}\left(N-\left\lceil\frac{n+1}{2}\right\rceil\right)Z_n \\
& + l_0^2(N-1)+\frac{1}{4}N(N-1)+\frac{\lambda N}{2},
\end{aligned}
\tag{1.27}
$$

where $\lceil\cdot\rceil$ is the ceiling function to the nearest integer greater than the input and $N$ is the total number of lattice sites.

## 1.4. Staggered fermions

Another approach for fermion discretization is the Kogut-Susskind staggered fermions [111]. In this scheme a staggered transformation, which is a symmetry of the free massive Dirac Hamiltonian, is used to remove the doubler without explicitly breaking chiral symmetry as is the case in Wilson fermions. The staggered transformation essentially places the first spinor degree of freedom on even sites and the second on odd sites leading to the Schwinger Hamiltonian that we will derive below [46, 53, 61, 70, 111, 112].

Our starting point is the free massive Dirac Hamiltonian in Eq. (1.17), that we discretize into

$$
H_{\text{free}} = a\sum_n\left(-i\psi_n^\dagger\gamma^0\gamma^1\frac{\psi_{n+1}-\psi_{n-1}}{2a}+m_{\text{lat}}\psi_n^\dagger\gamma^0\psi_n\right). \tag{1.28}
$$

The staggered transformation, which we apply to the above equation, is given by

$$
\psi_n = \frac{WX^n}{\sqrt{a}}\chi_n, \quad W=\frac{1}{\sqrt{2}}\begin{pmatrix} i & 1 \\ i & -1\end{pmatrix} \tag{1.29}
$$

Using our convention $\gamma^0 = X, \gamma^1 = iZ$, $\gamma^0\gamma^1 = Y$, we have

$$
H_{\text{free}} = a\sum_n\left(-i\chi_n^\dagger X^n\underbrace{W^\dagger Y W}_{X}X^{n+1}\frac{\chi_{n+1}-\chi_{n-1}}{2a^2}+\frac{m_{\text{lat}}}{a}\chi_n^\dagger X^n\underbrace{W^\dagger X W}_{Z}X^n\chi_n\right), \tag{1.30}
$$

which in turn gives

$$H_{\text{free}} = a \sum_n \left( -i\chi_n^\dagger \frac{\chi_{n+1} - \chi_{n-1}}{2a^2} + (-1)^n \frac{m_{\text{lat}}}{a} \chi_n^\dagger Z \chi_n \right). \tag{1.31}$$

We can expand this into up and down degrees of freedom $\chi_n = (\phi_{u,n}, \phi_{d,n})^T$

$$H_{\text{free}} = \frac{1}{2a} \sum_n \Big( - i\phi_{u,n}^\dagger \left(\phi_{u,n+1} - \phi_{u,n-1}\right) + 2m_{\text{lat}} a (-1)^n \phi_{u,n}^\dagger \phi_{u,n} \tag{1.32}$$

$$- i\phi_{d,n}^\dagger \left(\phi_{d,n+1} - \phi_{d,n-1}\right) - 2m_{\text{lat}} a (-1)^n \phi_{d,n}^\dagger \phi_{d,n} \Big), \tag{1.33}$$

from which we see that the up degrees of freedom on even sites behave like the down degrees of freedom on the odd sites and vice versa. Hence, we can drop the down degrees of freedom all together, which effectively spreads the up and down degrees of freedom onto even and odd sites, doubling the effective lattice spacing.

We now proceed as with the Wilson fermions to gauge the theory, which results in

$$H_S = -\frac{i}{2a} \sum_{n=0}^{N-2} \left( \phi_n^\dagger U_n \phi_{n+1} - \text{h.c.} \right) + m_{\text{lat}} \sum_{n=0}^{N-1} (-1)^n \phi_n^\dagger \phi_n + \frac{ag^2}{2} \sum_{n=0}^{N-2} \left(l_0 + L_n\right)^2, \tag{1.34}$$

where now, in contrast to Wilson fermions, the $\phi_n$ operators are single-component fermionic operators satisfying $\{\phi_n^\dagger, \phi_n'\} = \delta_{nn'}$ and we have dropped the up subscript from the up degrees of freedom that we have retained. We emphasize that $N$ in Eq. (1.34) labels the number of lattice sites on which only a single-component fermion field resides. This is in contrast to Wilson fermions where we start with $N$ sites on which a two component fermion field resides and then have double the sites after the mapping in Eq. (1.25). When the limit $a \to 0$ is taken, the fermionic operators on even and odd sites will correspond to the up and down components of the Dirac spinor $\psi(x)$. As aforementioned, this gives an effective lattice spacing of $2a$, which halves the range of $k_\mu$ to $k_\mu \in [-\frac{\pi}{2a}, \frac{\pi}{2a})$, thus avoiding the doubler at $k_\mu = \pi/a$ [101, 102].

Gauss's law has the same form as Eq. (1.22), but the charge operator is now given by [46, 53, 61]

$$Q_n = \phi_n^\dagger \phi_n - (1 - (-1)^n)/2. \tag{1.35}$$

Similar to Wilson fermions, we can use the unitary transformation with Eq. (1.24) to substitute out the gauge field operators and use the Jordan-Wigner transformation to map the fermionic operators to Pauli operators. The resulting Hamiltonian is given by [61]

$$\begin{aligned}
H_S = &\frac{x}{2}\sum_{n=0}^{N-2}\left(X_nX_{n+1}+Y_nY_{n+1}\right)\\
&+\frac{1}{2}\sum_{n=0}^{N-2}\sum_{k=n+1}^{N-1}(N-k-1+\lambda)Z_nZ_k\\
&+\sum_{n=0}^{N-2}\left(\frac{N}{4}-\frac{1}{2}\left\lceil\frac{n}{2}\right\rceil+l_0(N-n-1)\right)Z_n\\
&+\frac{m_{\text{lat}}}{g}\sqrt{x}\sum_{n=0}^{N-1}(-1)^nZ_n\\
&+l_0^2(N-1)+\frac{1}{2}l_0N+\frac{1}{8}N^2+\frac{\lambda}{4}N,
\end{aligned} \tag{1.36}$$

where the charge operator becomes

$$Q_n = (Z_n + (-1)^n)/2. \tag{1.37}$$

## 1.5. Open quantum systems

An OQS consists of a system that is in general exchanging energy, particles and information with an environment [113–117]. The total Hamiltonian that governs the unitary dynamics of the system and environment together is the sum of $H_S$, $H_E$ and $H_I$. These describe respectively the Hamiltonian of the system, the environment and the interaction between the two.

In Chapter 6, we investigate the time evolution of the Schwinger model within the framework of OQS. To set the stage for this analysis, we first present the theoretical foundations of this approach. As aforementioned, the model shares key features with QCD, such as confinement and charge screening, making it an ideal benchmark model for studying non-perturbative effects in strongly interacting systems. When coupled to an external environment, the Schwinger model serves as a valuable testbed for exploring dissipation and thermalization phenomena in gauge theories, analogous to quarkonia interacting with the quark gluon plasma (QGP), relevant for experiments at the large hadron collider (LHC) and relativistic heavy ion collider (RHIC) [118–121]. By formulating the Schwinger model as an OQS, we can investigate how mesonic excitations, such as the electric flux string or the Schwinger boson, evolve in the presence of a dissipative medium, gaining insights into the interplay between various system parameters, quantum mutual information, and thermalization.

Commonly we are interested in measuring observables on the system $S$, therefore we would like to find an equation for the time evolution of the reduced density matrix [122–125] of the system $\rho_S$ defined by tracing out the environment $\rho_S = \mathrm{Tr}_E(\rho)$. In the rest of this section we will derive this equation and describe the various approximations we will use which follow from [120].

For our setup, the system Hamiltonian $H_S$ will be the staggered fermion Schwinger model of Eq. (1.34), where again for numerical simulations we will be working with the transformed Hamiltonian of Eq. (1.36). The environment Hamiltonian $H_E$ as well as the interaction $H_I$ follow from [126, 127]. They are taken to be of the form

$$H_E = \int dx \left( \frac{1}{2}\Pi^2 + \frac{1}{2} (\nabla\phi)^2 + \frac{1}{2} m_\phi^2 \phi^2 + \frac{1}{4!} g\phi^4 \right) \tag{1.38}$$

$$H_I = \int dx \left( \lambda_I \phi(x) \bar{\psi}(x) \psi(x) \right), \tag{1.39}$$

with $\lambda_I$ determining the strength of the interaction between the system and the environment. Here $H_E$ is the Hamiltonian of a $\phi^4$-theory assumed to be in thermal equilibrium for all times at temperature $T = 1/\beta$, while $H_I$ is a Yukawa interaction Hamiltonian.

The first approximation we make is to take the Markovian limit [113, 120, 128] in which the interaction between the system and environment is weak such that the density matrix is approximated to be for all times in the product state

$$\rho(t) = \rho_S(t) \otimes \rho_E, \tag{1.40}$$

where $\rho_E = e^{-\beta H_E}/\mathrm{Tr}(e^{-\beta H_E})$ is the environment density matrix in the Gibbs state. Equation (1.40) does not imply that there are no excitations in environment caused by the system. It is simply the case that these excitations are assumed here to decay too fast to be resolved.

The second approximation we make is to work in the quantum Brownian motion (QBM) limit [113, 120, 129], which first requires the following definitions to be stated. Firstly, we define the system relaxation time $\tau_R$ by $\tau_R \sim T/\Delta E_I^{(\mathrm{int})^2}$, where $\Delta E_I^{(\mathrm{int})}$ is to be understood here as the energy gap of that Hamiltonian between the ground state and first excited state. This time scale describes how fast the system returns to equilibrium after a perturbation. Similarly the environment correlation time is defined by $\tau_E \sim 1/T$. Finally, the intrinsic time scale of the system is defined by $\tau_S \sim 1/\Delta E_S$, where $\Delta E_S$ is to be understood as the energy gap of the system Hamiltonian between the ground state and first excited state. Equipped with these definitions, the QBM is defined by the separation of time scales $\tau_R \gg \tau_E$, $\tau_S \gg \tau_E$ [113, 120]. The first inequality corresponds to the Markovian limit and suggests that the correlations in the environment decay during the typical time period of the system's relaxation. This inequality makes our product state assumption in Eq. (1.40) more applicable and emanates from the assumption of weak coupling between the system and environment. The second inequality suggests a high temperature limit $T \gg H_S$ which is met by choosing an appropriate value for the free variable $T$.

The evolution of the density matrix of $S$ with the above approximations is given by the

Lindblad master equation [113, 120]

$$\frac{d\rho_S(t)}{dt} = -i\left[H_S, \rho_S(t)\right] + a^2 \sum_{n,m=0}^{N-1} D(n-m)\left(J(m)\rho_S(t)J^\dagger(n) - \frac{1}{2}\left\{J^\dagger(n)J(m), \rho_S(t)\right\}\right), \tag{1.41}$$

in which $D(n-m)$ is the environment two point correlator [70]

$$D(n-m) = \lambda^2 \int_{-\infty}^{\infty} dt_1 \int_{-\infty}^{\infty} dt_2 \mathrm{Tr}_E\left[\phi^{(\mathrm{int})}(t_1, n)\phi^{(\mathrm{int})}(t_2, m)\rho_E\right]. \tag{1.42}$$

This environment correlator is also called the dissipator and only depends on the distance between the two spatial points on the lattice. Finally, the Lindblad jump operators are defined as [126]

$$J(n) = O(n) - \frac{1}{4T}\left[H_S, O(n)\right] \tag{1.43}$$

$$O(n) = (-1)^n \frac{Z_n + 1}{2a}, \tag{1.44}$$

where we have already made use of the Jordan-Wigner transformation. Equation. (1.41) is derived by an expansion in $H_S/T$ up to $\mathcal{O}\left((H_S/T)^2\right)$. The first term in Eq. (1.43) is the leading order and the second term is the next-to-leading order term. They respectively describe decoherence and dissipation [130].

# 2 Tensor network methods

This chapter is dedicated to tensor networks (TNs) [131], a powerful mathematical framework centered on the principle of data compression [132], with a vast range of applications in quantum many-body physics (QMBP) [33, 34, 38, 133], quantum computing [134–138], fluid dynamics [139, 140], machine learning [141–158], and many other areas of science and technology [159–161]. The first two applications are particularly relevant to this thesis.

In QMBP, TNs provide an efficient representation of quantum states, allowing for the exploration of the low-energy spectrum of a Hamiltonian and the subsequent study of the model's phase diagram, with some examples relevant to this thesis found in [48, 60, 61, 162]. They are especially well suited for the Hamiltonian formulation used in this work, which circumvents the sign problem affecting standard Monte Carlo methods [27, 163] when exploring regions of the phase diagram with large chemical potential or topological $\theta$-terms [25, 33]. For pure states, an important advantage of TN simulations is the efficient access to the entanglement entropy structure, which would otherwise be computationally expensive [164, 165]. Beyond pure states, TNs can also perform the time evolution of quantum states, including density matrices in out-of-equilibrium dynamics within the framework of open quantum system (OQS) [166–168].

For quantum computing, TNs are capable of efficiently simulating quantum circuits [136]. This capability can be leveraged alongside quantum computers to cross-check their results [169]. Indeed, in Sec. 3.2, we discuss the presence of noise for quantum computers, which is why current devices are classified as noisy intermediate-scale quantum (NISQ) [170]. Fields such as error mitigation and error correction have been actively developed to counteract this noise, and TNs have found applications in these areas as well [171–173]. Bridging QMBP with quantum computing, TNs serve as a valuable tool in predicting the computational resources required for quantum computers to approach the continuum limit in lattice gauge theories (LGTs) [61, 70].

This chapter is structured as follows. In Sec. 2.1, we introduce the most common type of TN, the matrix product state (MPS). Next, in Sec. 2.2, we demonstrate an important relationship between the entanglement entropy of a quantum state represented by an MPS and its bond dimension. We then introduce, in Sec. 2.3, the operators acting on the space of MPSs, called matrix product operators (MPOs). Additionally, a useful property of MPSs and MPOs, known as the canonical form, is explained in Sec. 2.4. Finally, we introduce the density matrix renormalization group (DMRG) algorithm in Sec. 2.5 and the adaptive time-dependent DMRG (ATD-DMRG) algorithm in Sec. 2.6, two widely used and powerful methods for obtaining the low-energy spectrum of a Hamiltonian and simulating the time evolution of quantum states, respectively [62, 174].

## 2.1. Matrix product states

MPSs are the most commonly used TN ansatz for quantum many-body states in one spatial dimension [29, 30, 175–177]. An MPS represents a rank-$N$ tensor as a product of $N$ rank-3 tensors $A$, expressed as

$$\begin{aligned} |\psi\rangle &\equiv \sum_{\sigma_0\sigma_1\ldots\sigma_{N-1}} \psi_{\sigma_0\sigma_1\ldots\sigma_{N-1}} |\sigma_0\sigma_1\ldots\sigma_{N-1}\rangle && (2.1)\\ &= \sum_{\sigma_0\sigma_1\ldots\sigma_{N-1}} \sum_{\alpha_0\alpha_1\ldots\alpha_{N-2}} A_{\sigma_0\alpha_0} A_{\sigma_1\alpha_0\alpha_1} \cdots A_{\sigma_{N-1}\alpha_{N-2}} |\sigma_0\sigma_1\ldots\sigma_{N-1}\rangle \,. && (2.2)\end{aligned}$$

Since we work with open boundary conditions (OBCs), the first and last tensors are rank-2. The indices $\sigma_n \in [0,1]$ for $n \in [0, N-1]$ are called physical indices, where the subscript $n$ specifies the site number. These indices represent the spin-1/2 degrees of freedom at each lattice site and thus define the Hilbert space of the Hamiltonian in Eq. (1.27) and Eq. (1.36). In the general case of the MPS ansatz these indices have a dimension $d$. The $\alpha_n$ indices, known as bond indices, have a dimension called the bond dimension $D$.

In Eq. (2.1), the tensor $\psi$ contains $2^N$ components. If we assume that all bond indices share the same bond dimension $D$, then in Eq. (2.2), the tensors $A$ store a total of $(N-2)dD^2+2dD$ components. Equating the two sides gives

$$2^N = (N-2)dD^2 + 2dD. \tag{2.3}$$

For this equality to hold, $D$ scales exponentially with $N$. However, if we truncate $D$ to a fixed constant value that does not scale with $N$, we obtain an approximation of $|\psi\rangle$ as a compressed MPS, where the number of components scales only linearly with $N$

$$2^N \to (N-2)dD^2 + 2dD. \tag{2.4}$$

In other words, we neglect an exponential amount of information initially stored in the larger $A$ tensors, which are reduced in size by this compression. Below, we examine which states allow this approximation with minimal or even zero error. First, however, we introduce some TN notation.

TNs offer a convenient diagrammatic notation [178–180], illustrated in Fig. 2.1. The circles in Fig. 2.1($a$) represent the tensors $A$, with their legs indicating tensor indices. When two tensors are contracted over shared indices, their corresponding legs are connected. Fig. 2.1($b$) depicts the diagrammatic representation of the MPS in Eq. (2.2).

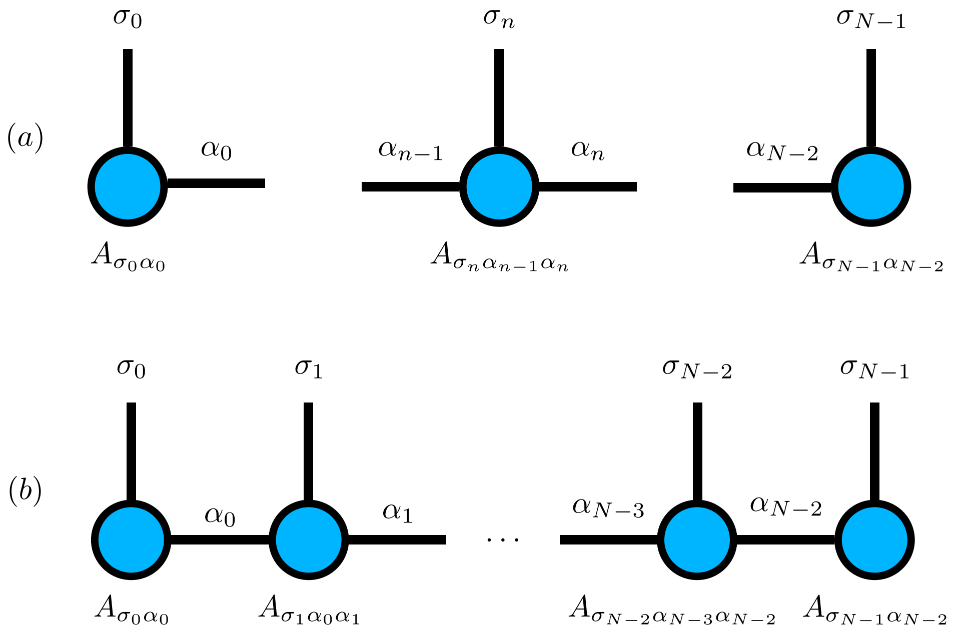
(a)
$\sigma_0$
$\alpha_0$
$A_{\sigma_0\alpha_0}$
$\sigma_n$
$\alpha_{n-1}$
$\alpha_n$
$A_{\sigma_n\alpha_{n-1}\alpha_n}$
$\sigma_{N-1}$
$\alpha_{N-2}$
$A_{\sigma_{N-1}\alpha_{N-2}}$
(b)
$\sigma_0$
$\sigma_1$
$\sigma_{N-2}$
$\sigma_{N-1}$
$\alpha_0$
$\alpha_1$
$\dots$
$\alpha_{N-3}$
$\alpha_{N-2}$
$A_{\sigma_0\alpha_0}$
$A_{\sigma_1\alpha_0\alpha_1}$
$A_{\sigma_{N-2}\alpha_{N-3}\alpha_{N-2}}$
$A_{\sigma_{N-1}\alpha_{N-2}}$

**Figure 2.1:** (*a*)*: Examples of rank-2 and rank-3 tensors. The circles represent tensors $A$, with vertical legs indicating physical indices $\sigma$ and horizontal legs representing bond indices $\alpha$.* (*b*)*: Diagrammatic representation of an matrix product state (MPS) as described in Eq.* (2.2)*. The connected legs signify contractions over the shared indices of the $A$ tensors.*

## 2.2. Entanglement entropy and bond dimension

This section is dedicated to deriving the important relationship between the bond dimension $D$ of an MPS and the bi-partite entanglement entropy of the state it represents [29, 30, 181, 182].

Starting from Eq. (2.1), we divide the system into two subsystems, one spanning sites 0 to $n-1$ and the other from $n$ to $N-1$. The indices within each subsystem are merged into composite indices $I \in [\sigma_0, \dots, \sigma_{n-1}]$ and $J \in [\sigma_n, \dots, \sigma_{N-1}]$, with dimensions $2^n$ and $2^{N-n}$, respectively. This can be written as

$$|\psi\rangle = \sum_{\sigma_0\sigma_1\dots\sigma_{N-1}} \psi_{\sigma_0\sigma_1\dots\sigma_{N-1}} |\sigma_0\sigma_1\dots\sigma_{N-1}\rangle \tag{2.5}$$

$$= \sum_{\sigma_0\sigma_1\dots\sigma_{N-1}} \psi_{(\sigma_0\dots\sigma_{n-1})(\sigma_n\dots\sigma_{N-1})} |\sigma_0\dots\sigma_{n-1}\rangle |\sigma_n\dots\sigma_{N-1}\rangle \tag{2.6}$$

$$= \sum_{IJ} \psi_{IJ} |I\rangle |J\rangle \,. \tag{2.7}$$

Viewing $\psi_{IJ}$ as a matrix, we perform an singular value decomposition (SVD) [183, 184]

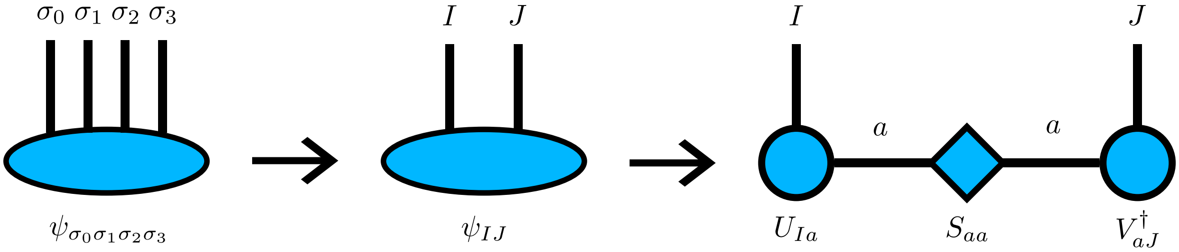
$\sigma_0\ \sigma_1\ \sigma_2\ \sigma_3$
$\psi_{\sigma_0\sigma_1\sigma_2\sigma_3}$
$I$
$J$
$\psi_{IJ}$
$I$
$J$
$a$
$a$
$U_{Ia}$
$S_{aa}$
$V^\dagger_{aJ}$

**Figure 2.2:** *Procedure for performing an singular value decomposition (SVD) on a multi-dimensional tensor, illustrated with a 4-site example. The first step is to reshape the tensor* $\psi_{\sigma_0\sigma_1\sigma_2\sigma_3}$ *into a matrix* $\psi_{IJ}$*, where* $I \in [\sigma_0, \sigma_1]$ *and* $J \in [\sigma_2, \sigma_3]$*. This matrix is then decomposed using the SVD as* $\psi_{IJ} = \sum_a U_{Ia} S_{aa} V^\dagger_{aJ}$*. Here,* $U$ *and* $V$ *are unitary matrices, and* $S$ *is a diagonal matrix containing the singular values.*

between the left ($L$) and right ($R$) indices, $I$ and $J$:

$$\sum_{IJ} \psi_{IJ} \left|I\right\rangle \left|J\right\rangle = \sum_{a=0}^{\min\left(2^n-1, 2^{N-n}-1\right)} S_{aa} \underbrace{\left(\sum_{I=0}^{2^n-1} U_{Ia} \left|I\right\rangle\right)}_{\left|a\right\rangle_L} \underbrace{\left(\sum_{J=0}^{2^{N-n}-1} V^\dagger_{aJ} \left|J\right\rangle\right)}_{\left|a\right\rangle_R} \tag{2.8}$$

$$= \sum_{a=0}^{\min\left(2^n-1, 2^{N-n}-1\right)} S_{aa} \left|a\right\rangle_L \left|a\right\rangle_R , \tag{2.9}$$

where the diagonal matrix $S_{aa}$ stores the singular values in descending order, and $U$, $V^\dagger$ are unitary matrices such that $\psi_{IJ} \equiv \sum_a U_{Ia} S_{aa} V^\dagger_{aJ}$. These matrices satisfy $\sum_I U^*_{Ia'} U_{Ia} = \delta_{a'a}$ and $\sum_J V_{Ja'} V^*_{Ja} = \delta_{a'a}$. The above procedure is illustrated in Fig. 2.2 using TN notation.

Defining $D \equiv \min\left(2^n - 1, 2^{N-n} - 1\right)$ and setting $\lambda_a \equiv S_{aa}$ in Eq. (2.9), we obtain the Schmidt decomposition [185–187]

$$\left|\psi\right\rangle = \sum_{a=0}^{D-1} \lambda_a \left|a\right\rangle_L \left|a\right\rangle_R . \tag{2.10}$$

We can now express the density matrix of this pure quantum state as $\rho = \left|\psi\right\rangle \left\langle\psi\right|$. Tracing out the indices of the right part, and after a few simple manipulations, we obtain the reduced density matrix for the left part

$$\rho_L \equiv \mathrm{Tr}_R\left(\rho\right) = \sum_{a=0}^{D-1} \left|\lambda_a\right|^2 \left|a\right\rangle_L \left\langle a\right|_L . \tag{2.11}$$

The entanglement entropy $S$ between the two subsystems is then given by [164, 188]

$$S \equiv -\mathrm{Tr}_L\left(\rho_L \ln\left(\rho_L\right)\right) \tag{2.12}$$

$$= -\sum_{a=0}^{D-1} \left|\lambda_a\right|^2 \ln\left(\left|\lambda_a\right|^2\right) . \tag{2.13}$$

The maximum entanglement entropy $S$ occurs for a completely mixed state [30], where all $\lambda_a$ are equal, i.e., $\lambda_a = 1/\sqrt{D}$. This yields the fundamental relationship between entanglement entropy and bond dimension

$$S \leq \ln(D)\,. \tag{2.14}$$

From this, we immediately see that a product state, that has zero entanglement entropy at any bi-partition, can be represented by an MPS with $D = 1$, which is the most efficient compression possible according to Eq. (2.4). More generally, the bond dimension $D$ determines the amount of bi-partite entanglement entropy present between two subsystems.

Using Eq. (2.14), we can now understand why MPSs have become a widely used ansatz for many-body quantum states. In many cases, the quantum system of interest is governed by a local and gapped Hamiltonian, meaning it has a finite range of interactions between any two sites and a finite energy gap between the ground state and first excited state. The ground state of such Hamiltonians obeys the area law [189–192], which states that the entanglement entropy between subsystems scales with the area of the boundary rather than the volume. In one spatial dimension, the boundary area remains constant as the system size $N$ increases. Consequently, MPSs can efficiently represent these states with a bond dimension $D$ that does not grow inefficiently with $N$ [174, 188, 193–197]. In fact, the singular values on any given bi-partition of these are law states decay exponentially, allowing for a small bond dimension to represent such states with high precision [29].

## 2.3. Matrix product operators

MPOs are TNs that represent operators acting on an MPS to produce a new MPS [29, 198–201]. As an example, the Hamiltonian of a quantum system can be represented as an MPO [198]. To illustrate this, we use a simple model, such as the Ising model [202–204], to show how we can transform a Hamiltonian of Pauli operators into an MPO.

The MPO expression of an operator $O$ acting on $N$ lattice sites with OBCs is written as [29]

$$\begin{aligned} O &\equiv \sum_{\sigma\sigma'} O^{\sigma'_0 \ldots \sigma'_{N-1}}_{\sigma_0 \ldots \sigma_{N-1}} \left|\sigma'_0 \ldots \sigma'_{N-1}\right\rangle \left\langle \sigma_0 \ldots \sigma_{N-1}\right| \qquad &(2.15)\\ &= \sum_{\sigma\sigma'\alpha} W^{\sigma'_0}_{\sigma_0\alpha_0} W^{\sigma'_1}_{\sigma_1\alpha_0\alpha_1} \ldots W^{\sigma'_{N-2}}_{\sigma_{N-2}\alpha_{N-3}\alpha_{N-2}} W^{\sigma'_{N-1}}_{\sigma_{N-1}\alpha_{N-2}} \left|\sigma'_0 \ldots \sigma'_{N-1}\right\rangle \left\langle \sigma_0 \ldots \sigma_{N-1}\right| \qquad &(2.16) \end{aligned}$$

where we make no distinction between upper and lower indices, and the sum runs over all $\sigma$, $\sigma'$, and $\alpha$ indices. Hence, we see that the MPO is a product of rank-3 and rank-4 tensors $W$, consisting of two physical indices and either one or two bond indices $\alpha$. The corresponding TN notation for the MPO is shown in Fig. 2.3, similar to Fig. 2.1 for the MPS.

Next, we turn to the Ising model Hamiltonian, given by [203]

$$H = -J \sum_{n=0}^{N-2} Z_n Z_{n+1} + g \sum_{n=0}^{N-1} X_n. \tag{2.17}$$

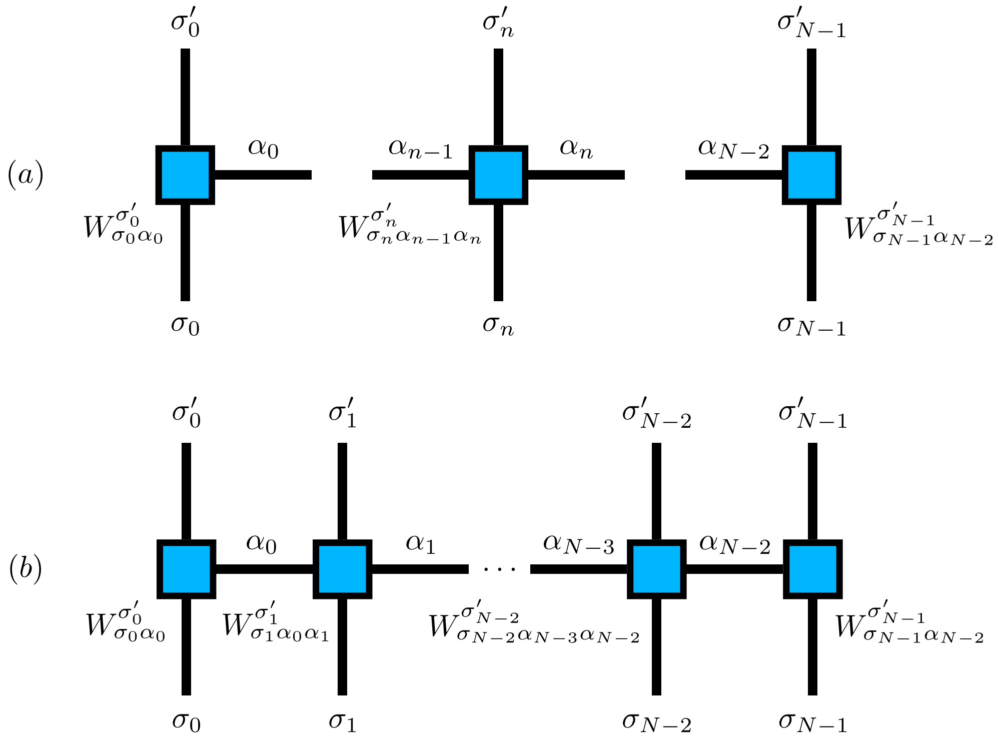
(a)
$\sigma'_0$
$\sigma'_n$
$\sigma'_{N-1}$
$\alpha_0$
$\alpha_{n-1}$
$\alpha_n$
$\alpha_{N-2}$
$W^{\sigma'_0}_{\sigma_0\alpha_0}$
$W^{\sigma'_n}_{\sigma_n\alpha_{n-1}\alpha_n}$
$W^{\sigma'_{N-1}}_{\sigma_{N-1}\alpha_{N-2}}$
$\sigma_0$
$\sigma_n$
$\sigma_{N-1}$
(b)
$\sigma'_0$
$\sigma'_1$
$\sigma'_{N-2}$
$\sigma'_{N-1}$
$\alpha_0$
$\alpha_1$
$\cdots$
$\alpha_{N-3}$
$\alpha_{N-2}$
$W^{\sigma'_0}_{\sigma_0\alpha_0}$
$W^{\sigma'_1}_{\sigma_1\alpha_0\alpha_1}$
$W^{\sigma'_{N-2}}_{\sigma_{N-2}\alpha_{N-3}\alpha_{N-2}}$
$W^{\sigma'_{N-1}}_{\sigma_{N-1}\alpha_{N-2}}$
$\sigma_0$
$\sigma_1$
$\sigma_{N-2}$
$\sigma_{N-1}$

**Figure 2.3:** *(a): Examples of rank-3 and rank-4 tensors. The squares represent tensors $W$, with vertical legs indicating physical indices $\sigma, \sigma'$, and horizontal legs representing bond indices $\alpha$. (b): Diagrammatic representation of an matrix product operator (MPO), as described in Eq. (2.16). The connected legs denote contractions over the shared indices of the $W$ tensors.*

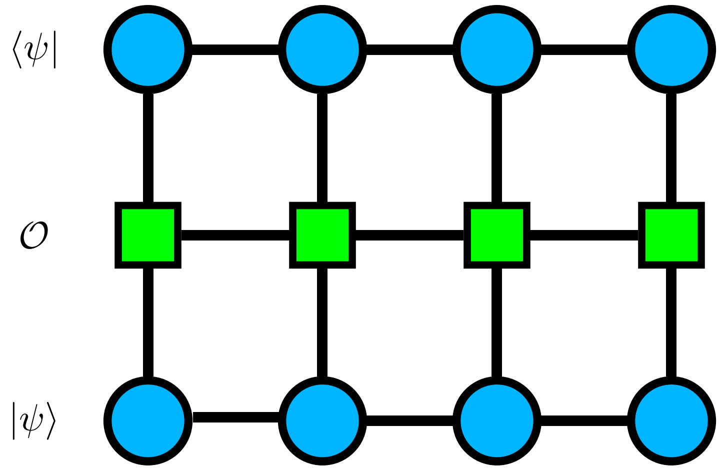

**Figure 2.4:** *The diagram measures the expectation value $\langle\psi|\,\mathcal{O}\,|\psi\rangle$ of an operator $\mathcal{O}$ with respect to the quantum state $|\psi\rangle$. The operator is represented by the green boxes forming the MPO in the middle. The quantum state $|\psi\rangle$ is represented by the blue circles forming the MPS on the bottom and by convention the MPS with its legs facing down represents $\langle\psi|$.*

This Hamiltonian consists of sums of Pauli strings, such as $Z_0Z_1$, which MPOs can represent in a compact and efficient manner [199, 205]. Note that the physical indices $\sigma, \sigma'$ of the $W$ tensors correspond to the indices of the Pauli operators, for example, $(Z_0)^{\sigma'_0}_{\sigma_0}\,(Z_1)^{\sigma'_1}_{\sigma_1}$. For $N = 3$, we clarify that the notation $Z_0Z_1$ implies $Z_0Z_1I_2$, where $I$ denotes the identity operator on the spin-1/2 space. Hence, for $N = 3$, we have

$$H = -J\left(Z_0Z_1 + Z_1Z_2\right) + g\left(X_0 + X_1 + X_2\right). \tag{2.18}$$

This can be expressed in MPO form with the following $W$ tensors:

$$W_{\alpha_0} = \begin{bmatrix} I & Z_0 & gX_0 \end{bmatrix}, \quad W_{\alpha_0\alpha_1} = \begin{bmatrix} I & Z_1 & gX_1 \\ 0 & 0 & -JZ_1 \\ 0 & 0 & I \end{bmatrix}, \quad W_{\alpha_1} = \begin{bmatrix} gX_2 \\ -JZ_2 \\ I \end{bmatrix}. \tag{2.19}$$

Multiplying out these matrices gives the desired Hamiltonian from Eq. (2.18). Further details on how to derive these matrices for general Hamiltonians can be found in [180, 199, 205]. However, throughout this thesis, we make use of the ITensors [206] library, which allows for the automatic conversion of operator strings to MPOs.

To conclude this section we present in Fig. 2.4 how to measure the expectation value of an operator $\mathcal{O}$ with respect to a quantum state $|\psi\rangle$. In this figure, the bra state $\langle\psi|$ notation is introduced. To distinguish it from the ket state $|\psi\rangle$, its legs are by convention placed below the circles.

## 2.4. Canonical form

Before describing the DMRG algorithm in the next section, we first need to define the property of the canonical form for both MPSs and MPOs.

An MPS tensor, say on site $n$, is said to be in left canonical form (LCF) when the corresponding tensor $A$ satisfies the following equation [29]

$$A^{*}_{\sigma_n \alpha_{n-1} \alpha'_n} A_{\sigma_n \alpha_{n-1} \alpha_n} = \delta_{\alpha'_n \alpha_n}, \tag{2.20}$$

where, unless stated otherwise, the Einstein summation convention is used throughout the rest of this thesis. Similarly, for right canonical form (RCF), the equation becomes

$$A^{*}_{\sigma_n \alpha'_{n-1} \alpha_n} A_{\sigma_n \alpha_{n-1} \alpha_n} = \delta_{\alpha'_{n-1} \alpha_{n-1}}. \tag{2.21}$$

For the case of the MPO, a tensor on site $n$ is said to be in LCF when the corresponding tensor $W$ satisfies the following equation [207]

$$W^{*\sigma'_n}_{\sigma_n \alpha_{n-1} \alpha'_n} W^{\sigma'_n}_{\sigma_n \alpha_{n-1} \alpha_n} = \delta_{\alpha'_n \alpha_n}, \tag{2.22}$$

and for the RCF, it satisfies

$$W^{*\sigma'_n}_{\sigma_n \alpha'_{n-1} \alpha_n} W^{\sigma'_n}_{\sigma_n \alpha_{n-1} \alpha_n} = \delta_{\alpha'_{n-1} \alpha_{n-1}}. \tag{2.23}$$

The above equations are summarized diagrammatically in Fig. 2.5. In this figure, subplots (a), (b), (c), and (d) correspond to Eq. (2.20), (2.21), (2.22), and (2.23), respectively. When some sites of the MPS are in LCF and others in RCF, we refer to this as a mixed canonical form (MCF).

## 2.5. Density matrix renormalization group

Equipped with the concepts of MPSs, MPOs, and canonical form, we can now explain the DMRG algorithm [29, 174]. This algorithm is designed to find the ground state of a given MPO, which, in our case, represents the Hamiltonian of a quantum system. It is a variational algorithm that adjusts the entries of the tensors in an MPS ansatz to minimize its energy with respect to the Hamiltonian, thereby reaching the ground state. The energy is given by

$$E = \frac{\langle\psi| H |\psi\rangle}{\langle\psi|\psi\rangle}, \tag{2.24}$$

with the corresponding TN diagram shown in Fig. 2.6.

First the ansatz is initialized in some state, which can be a random state, and the components of the tensors form the variational parameters to be optimized. As we will discuss below Eq. (2.26), we choose a LCF gauge for the initial state. The algorithm then sweeps through

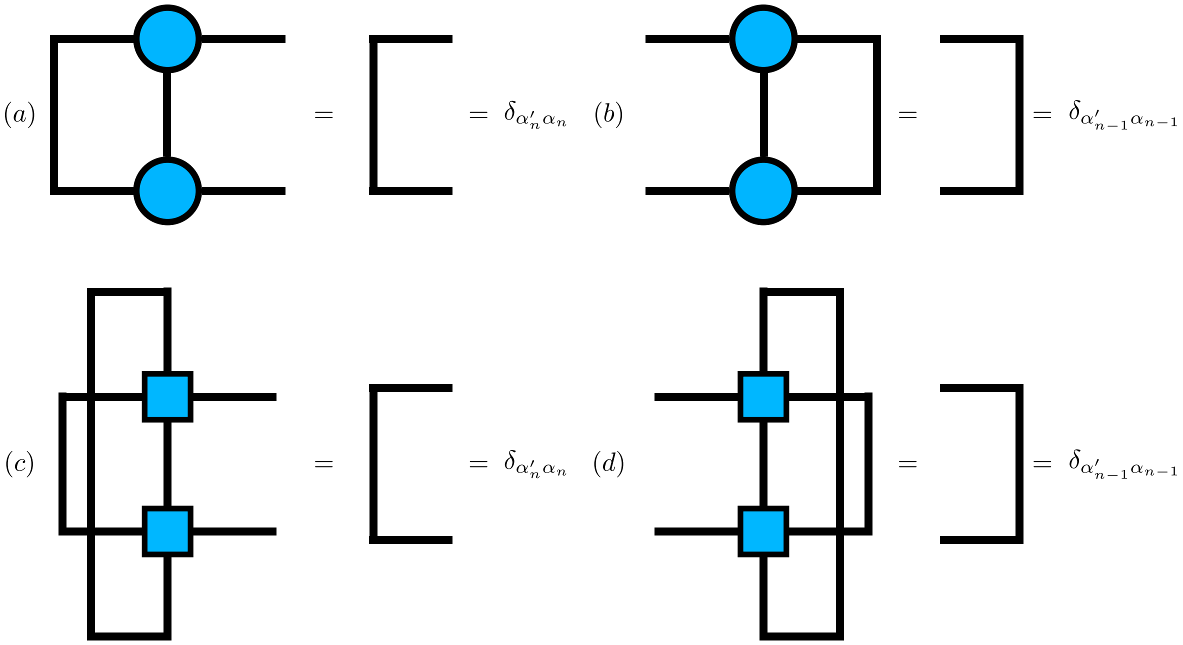
(a)
=
= $\delta_{\alpha'_n \alpha_n}$
(b)
=
= $\delta_{\alpha'_{n-1} \alpha_{n-1}}$
(c)
=
= $\delta_{\alpha'_n \alpha_n}$
(d)
=
= $\delta_{\alpha'_{n-1} \alpha_{n-1}}$

**Figure 2.5:** (*a*): *Left canonical form (LCF) for an matrix product state (MPS) site, corresponding to Eq.* (2.20). (*b*): *Right canonical form (RCF) for an MPS site, corresponding to Eq.* (2.21). (*c*): *LCF for an matrix product operator (MPO) site, corresponding to Eq.* (2.22). (*d*): *RCF for an MPO site, corresponding to Eq.* (2.23).

the sites of the MPS ansatz from left to right and from right to left, in pairs of two sites. It replaces the tensors of the MPS on these two sites to minimize the energy with respect to these specific sites. In Fig. 2.6, we consider the case where sites $n$ and $n+1$ are being optimized. The figure defines the tensors $P_n$ and $N_n$, with which we can express the energy as

$$E = \frac{\left(A_n^* A_{n+1}^*\right) P_n \left(A_n A_{n+1}\right)}{\left(A_n^* A_{n+1}^*\right) N_n \left(A_n A_{n+1}\right)}. \tag{2.25}$$

To find the new tensors for the two sites being optimized that minimize the energy, we set the derivative of the energy with respect to these tensors to zero, leading to the following equation

$$\frac{\partial E}{\partial \left(A_n^* A_{n+1}^*\right)} = 0 \implies P_n \left(A_n A_{n+1}\right) = E N_n \left(A_n A_{n+1}\right). \tag{2.26}$$

If we keep the tensors on the left of site $n$ in LCF and those on the right of site $n+1$ in RCF such that the MPS ansatz has MCF, then $N_n$ becomes the identity by the definitions given in Eq. (2.20), (2.21), and the corresponding diagrammatic notation in Fig. 2.5. Thus, the final optimization equation for the DMRG algorithm becomes

$$P_n(A_n A_{n+1}) = E(A_n A_{n+1}), \tag{2.27}$$

where in practice, $P_n$ can be reshaped into a matrix, and its eigenstate with the lowest eigenvalue can be computed using an algorithm such as Lanczos [208], which gives the solution

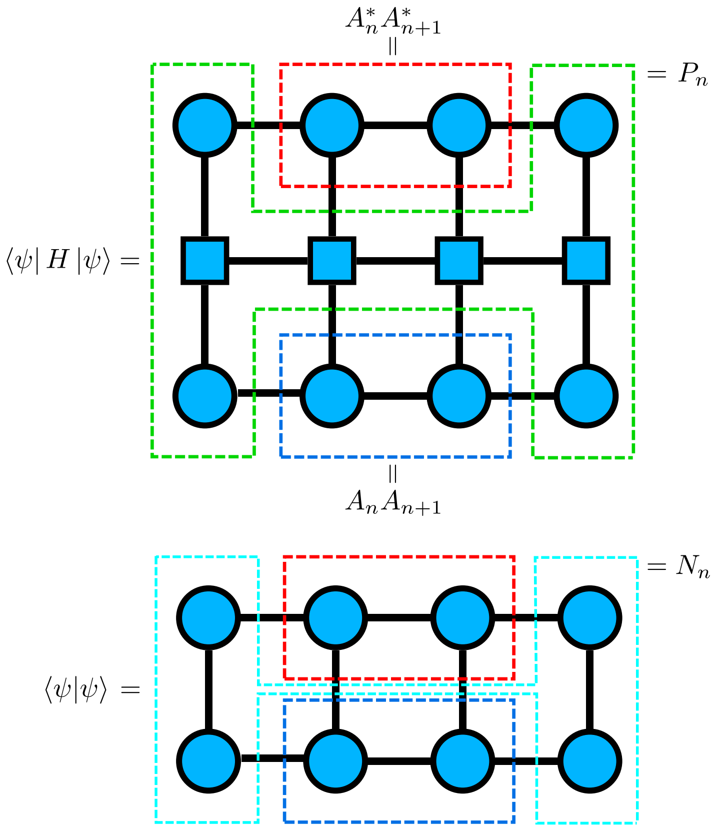
$A_n^* A_{n+1}^*$
$\|$
$= P_n$
$\langle\psi| H |\psi\rangle =$
$\|$
$A_n A_{n+1}$
$= N_n$
$\langle\psi|\psi\rangle =$

**Figure 2.6:** *The top diagram defines $P_n$ inside the green box, while the bottom diagram defines $N_n$ inside the cyan box. These two tensors are used to derive the optimization formula in Eq.* (2.26) *within the density matrix renormalization group (DMRG) algorithm. The division of the top by the bottom diagram gives the energy $E = \langle\psi| H |\psi\rangle / \langle\psi|\psi\rangle$ to be minimized by the DMRG.*

for the new tensors $A_n$ and $A_{n+1}$.

Before replacing the tensors, we can control the bond dimension between sites $n$ and $n+1$ by performing an SVD on the solution from Lanczos and truncating to a given bond dimension. This approximation minimizes the Euclidean distance between the original and the final tensor [29, 209], while also separating the sites $n$ and $n+1$ into two tensors that replace the ones in our MPS ansatz. Crucially, by keeping our MPS in MCF, as mentioned above, this minimizes the Euclidean distance between the original and approximated MPS. In other words, the approximation resulting from the SVD truncation is globally optimal [29]. Intuitively, since the sites to the left of site $n$ are in LCF, they reduce to the identity in the Euclidean distance formula. The same applies to the sites to the right of site $n+1$ in RCF, meaning the formula becomes independent of the sites other than $n$ and $n+1$. The bond dimension can either be determined by setting a fixed cutoff or by choosing a singular value tolerance $\epsilon$. In the latter case, the ratio of the sum of the squares of the neglected singular values to the sum of the squares of all singular values must not exceed this cutoff at any given SVD truncation [206].

The next step in the algorithm is to continue to sites $n+1$ and $n+2$ and repeat the process, sweeping through the MPS until the fractional change in energy $\eta$ falls below a given input threshold or the number of sweeps reaches its maximum input limit. This completes the DMRG algorithm, and the optimized MPS ansatz represents the ground state of the Hamiltonian MPO.

To find the first excited state, we take the MPS ansatz optimized to the ground state $|\mathrm{GS}\rangle$ and modify the Hamiltonian as follows [60, 210]

$$H \to H' = H + \lambda \left|\mathrm{GS}\right\rangle \left\langle\mathrm{GS}\right| , \tag{2.28}$$

where $\lambda$ is a generic Lagrange multiplier that needs to be larger than the gap between the ground and first excited state of $H$. The ground state of $H'$ is then the first excited state of $H$, which can be found using the DMRG algorithm. Throughout this thesis, we use the implementation of the ITensors library [206] when employing the DMRG algorithm.

## 2.6. Adaptive time-dependent DMRG

Beyond DMRG, which is an algorithm that finds the low-energy spectrum states of Hamiltonians, we will make use in Ch. 6 of an algorithm that is able to perform time evolution of quantum states according to some equation of motion. This is called the ATD-DMRG [211–213], and we will specifically use it within the context of OQSs to perform the time evolution of the system's reduced density matrix according to the Lindblad master equation in Eq. (1.41).

Since we will use ATD-DMRG specifically for Eq. (1.41), our explanation of the algorithm will focus on this context. It is convenient to multiply this equation by the lattice spacing $a$, expressing all variables and operators in dimensionless form

$$\begin{aligned}\frac{d\rho_S(t/a)}{d(t/a)} =& - i\left[aH_S, \rho_S(t/a)\right] \\ &+ \sum_{n,k=0}^{N-1} aD(n-k)\left(aJ(k)\rho_S(t/a)aJ^\dagger(n) - \frac{1}{2}\left\{aJ^\dagger(n)aJ(k), \rho_S(t/a)\right\}\right).\end{aligned} \tag{2.29}$$

Moving forward from this point, we will suppress the lattice spacing $a$. Writing Eq. (2.29) as $\dot{\rho}_S(t) = \mathcal{L}\rho_S(t)$, it has the formal solution

$$\rho_S(t) = e^{t\mathcal{L}}\rho_S(t=0), \tag{2.30}$$

where the Liouvillian superoperator $\mathcal{L}$ that generates the dynamics is defined by [214]

$$\begin{aligned}\mathcal{L} =& - iH_S \otimes I + iI \otimes H_S \\ &+ \sum_{n,k=0}^{N-1} D(n-k)\left(J(k)\otimes J^\dagger(n) - \frac{1}{2}J^\dagger(n)J(k)\otimes I - \frac{1}{2}I\otimes J^\dagger(n)J(k)\right),\end{aligned} \tag{2.31}$$

which then gives the time evolution of the system's density matrix $\rho_S(t)$ through Eq. (2.30).

The density matrix is an operator, hence, it is represented by an MPO. The exponential of Eq. (2.31) acts on $\rho_S(t=0)$ as shown in Eq. (2.30). We can then understand the meaning of the tensor product in Eq. (2.31) as follows. Operators to the left/right of the tensor product symbol act on the $\sigma'/\sigma$ indices respectively, where an example of the $\sigma$ indices is shown in Fig. 2.3. To be able to apply all operators in Eq. (2.31) with one TN contraction, we reshape our MPO for $\rho_S(t)$ into an MPS using SVD. This transformation is in the same spirit as how a matrix can be converted to a vector and shown schematically in Fig. 2.7. It brings the $\sigma'/\sigma$ indices to the even/odd sites of the MPS, where the first site is considered the zeroth site. In Fig. 2.8 we show how measuring observables is performed after this transformation from MPO to MPS.

In order to be able to approximate the action of $e^{t\mathcal{L}}$ on $\rho_S(t)$, we split the operator $\mathcal{L}$ into three groups that we call even $\mathcal{L}_E$, odd $\mathcal{L}_O$, Taylor $\mathcal{L}_T$, and employ the Trotterization scheme [215]

$$e^{\tau\mathcal{L}} \approx e^{\frac{\tau}{2}\mathcal{L}_E}e^{\frac{\tau}{2}\mathcal{L}_T}e^{\tau\mathcal{L}_O}e^{\frac{\tau}{2}\mathcal{L}_T}e^{\frac{\tau}{2}\mathcal{L}_E} + \mathcal{O}\left(\tau^3\right). \tag{2.32}$$

The even and odd are groups of operators spanning four sites. The Taylor group encompasses all other operators that cannot be part of the even or odd groups. For instance, the Taylor group encompasses interactions that extend across the entire lattice, originating from terms like those in the second line of Eq. (1.36). These groups are shown in Fig. 2.9.

The even and odd group operators $e^{\frac{\tau}{2}\mathcal{L}_E}$, $e^{\tau\mathcal{L}_O}$, are then represented exactly as rank-8 tensors as shown by the green and blue boxes of Fig. 2.9, whereas the Taylor group operator

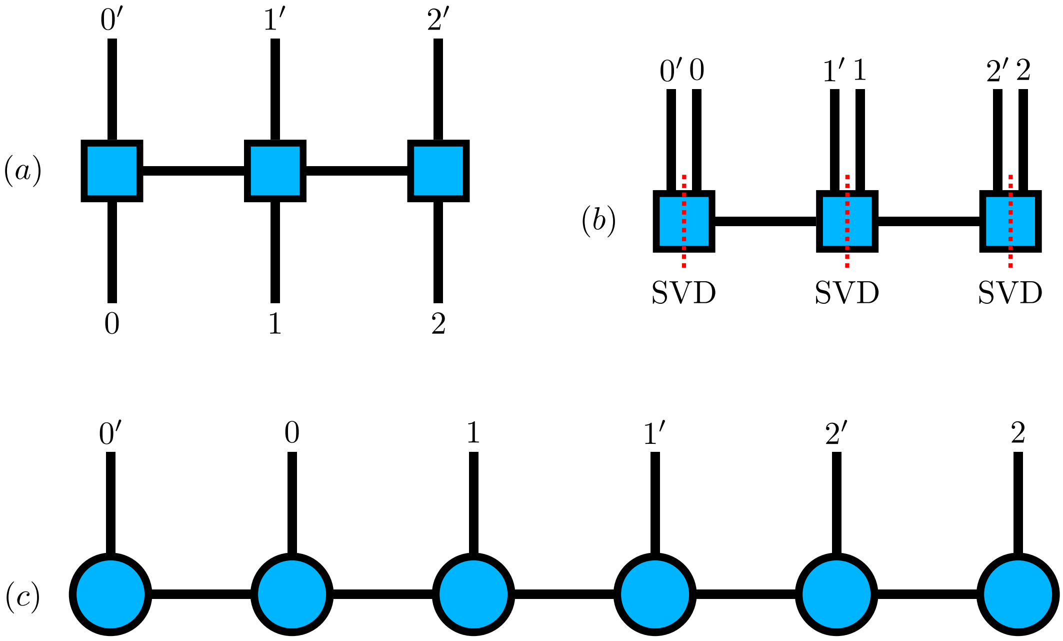

**Figure 2.7:** $(a)$: *Initial matrix product operator (MPO) representing the system's density matrix* $\rho_S(t)$. $(b)$: *Separating the legs on each site with singular value decomposition (SVD).* $(c)$: *matrix product state (MPS) representing* $\rho_S(t)$ *equivalent to the MPO in* $(a)$.

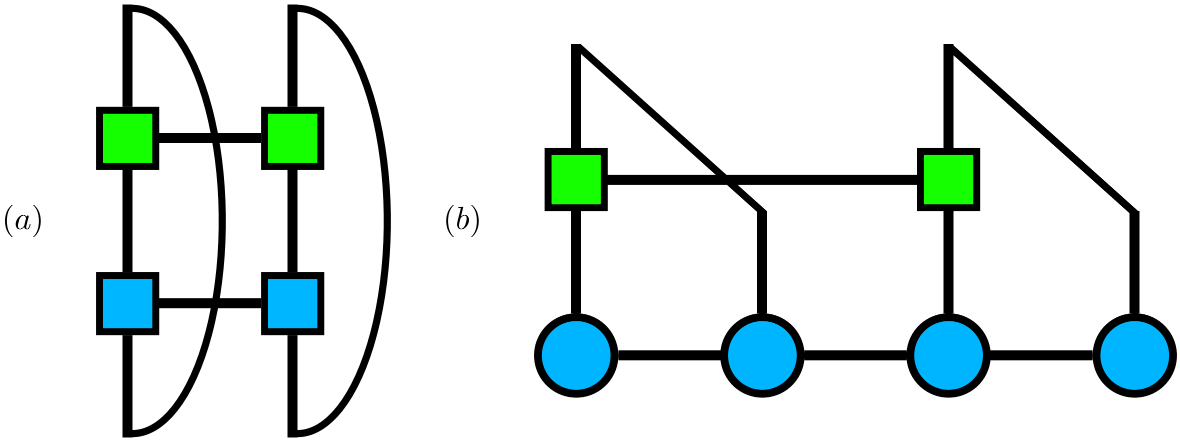

**Figure 2.8:** $(a)$: *Measuring the expectation value* $\mathrm{Tr}(O\rho_S(t))$ *with the top matrix product operator (MPO) (green boxes) representing a generic operator* $O$ *and the bottom MPO (blue boxes) representing the system's density matrix* $\rho_S(t)$. $(b)$: *The equivalent contraction to* $(a)$ *after the transformation of* $\rho_S(t)$ *from MPO to matrix product state (MPS) (blue circles) shown in Fig. 2.7.*

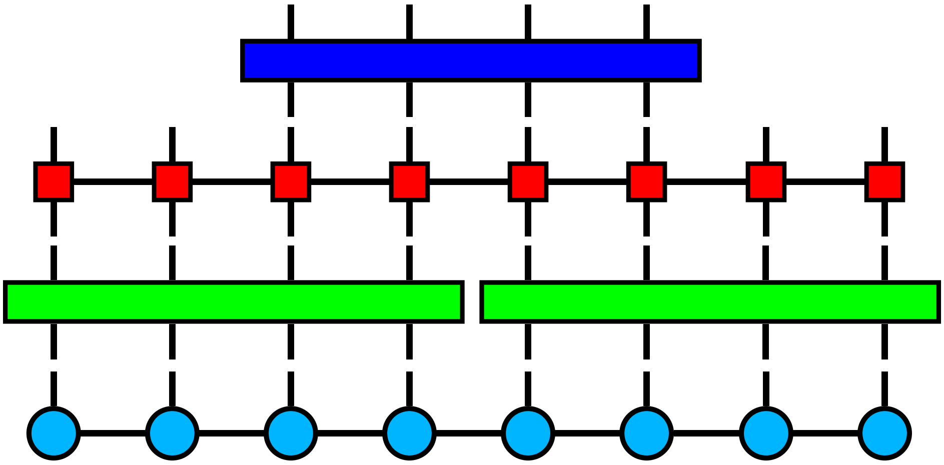

**Figure 2.9:** *Schematic drawing example of the even group (bottom green boxes), Taylor group (middle red boxes) and odd group (top blue box) for $\mathcal{L}$ in Eq. (2.31) at $N = 4$. These groups are applied to the MPS at the very bottom representing $\rho_S$ as required by Eq. (2.32), although here only $e^{\tau\mathcal{L}_O}e^{\frac{\tau}{2}\mathcal{L}_T}e^{\frac{\tau}{2}\mathcal{L}_E}$ is shown.*

is Taylor expanded as

$$e^{\tau\mathcal{L}_T} \approx 1 + \sum_{j=1}^{\kappa} \frac{(\tau\mathcal{L}_T)^j}{j!}. \tag{2.33}$$

We express the right-hand side of Eq. (2.33) as a global MPO with two singular value cutoffs, $\epsilon_1$ and $\epsilon_2$, shown with red boxes in Fig. 2.9. The ITensors Julia library [206] enables the automatic conversion of $\mathcal{L}_T$ into an MPO while applying a singular value truncation, which we denote as $\epsilon_1$. This cutoff ensures that the ratio of the sum of squares of the discarded singular values to the total sum of squares of all singular values does not exceed $\epsilon_1$ during any SVD truncation. The second cutoff, $\epsilon_2$, is used when multiplying $\mathcal{L}_T$ onto itself to compute powers of this operator as required for the right-hand side of Eq. (2.33).

Now the goal of ATD-DMRG is to apply the right-hand side of Eq. (2.32) to $\rho_S(t = 0)$, thus obtaining $\rho_S(\tau)$. The fundamental principle of the algorithm is to maintain the MCF of the MPS after each multiplication step [213]. This guarantees that the SVD truncation applied after every multiplication of either a four-site tensor or the global Taylor MPO remains optimal. The process is shown in Fig. 2.9 and begins with the even group, where the first operation involves multiplying the four-site tensor spanning from site 0 to site 3. At this stage, the MPS is in RCF.

Subsequently, we apply the second green four-site tensor covering sites 4 to 7. Before performing this step, the MPS sites from 0 through 3 are converted to LCF using a QR decomposition without truncation. No specific canonical form needs to be enforced before applying the global Taylor MPO. However, once the global Taylor MPO is applied, the process continues with the first four-site tensor of the odd group, which extends from site 2 to site 5. To accommodate this, the MPS sites 0 and 1 are transformed into LCF, while sites 6 and 7 are placed in the RCF before multiplication.

This structured approach is systematically followed for all four-site tensors in the odd group and is generally maintained throughout the full implementation of Eq. (2.32). Repeating this sequence for multiple iterations enables the system to evolve to a desired total time $t$ and this completes the algorithm.

# 3 | Quantum computing methods

Quantum computing is an emerging and rapidly advancing field, with a diverse range of applications spanning quantum simulations [33, 61, 77, 80, 81, 83, 169, 216–222], cryptography [39, 223–225], optimization [226–228], materials science [229–233], chemistry [234–236], quantum communication [237], machine learning [238–242], and more [243–246]. Unlike classical computing, quantum computing harnesses the power of quantum entanglement and superposition. These quantum phenomena enable quantum computers to execute certain algorithms theoretically more efficiently than their classical counterparts [39]. Relevant to this thesis, quantum computing also facilitates the efficient representation of quantum states within the context of quantum many-body physics (QMBP) [247]. The quantum computing framework is inherently suited to the Hamiltonian formulation [39, 248, 249], which, as discussed in Ch. 2, allows it to circumvent the sign problem that affects conventional Monte Carlo methods [27, 163]. In contrast to tensor networks (TNs), quantum computing can efficiently represent states with arbitrary levels of entanglement entropy [250], making it a promising alternative to both TNs and Monte Carlo techniques.

In Ch. 5, we utilize the variational quantum eigensolver (VQE) algorithm [251] to determine the ground states of the Hamiltonians in Eq. (1.27) and Eq. (1.36). This algorithm facilitates the exploration of phase space in high-energy physics models [252], such as the Schwinger model [61]. It thus holds promise for being able to investigate the parts of the quantum chromodynamics (QCD) phase diagram [216] which are currently beyond the reach of existing methods, such as in the large baryon chemical potential regime [24]. To explain this algorithm, we first introduce quantum circuits and their notation in Sec. 3.1.1. In Sec. 3.1.2, we describe how observable expectation values are measured, before moving to the core routine of the VQE algorithm in Sec. 3.1.3.

Given the inherent errors associated with quantum computers particularly in the noisy intermediate-scale quantum (NISQ) era [253], we employ in Ch. 5 several error mitigation techniques, which are discussed in Sec. 3.2. Specifically, Sec. 3.2.1 provides a brief overview of the twirled readout error extinction (TREX) algorithm for readout error mitigation [254]. We then turn to zero noise extrapolation (ZNE) in Sec. 3.2.2, which is a method for mitigating incoherent errors [255]. To address coherent errors, we employ Pauli twirling [256], explained in Sec. 3.2.3, and conclude the chapter with a discussion of the dynamical decoupling method in Sec. 3.2.4 [257].

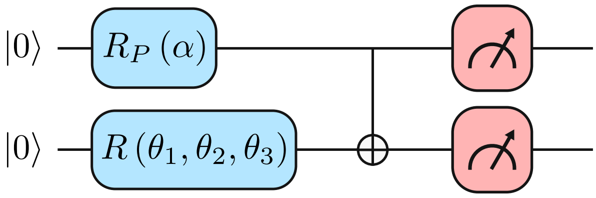

**Figure 3.1:** *A quantum circuit of two qubits. The states $|0\rangle$ specify the initial state of the qubits. The qubits are spin-1/2 degrees of freedom, hence, can be in the general normalized state $|\psi\rangle = \alpha|0\rangle + \beta|1\rangle$. In other words, their basis consists of the eigenvectors of the Pauli $Z$ operator. Actions on these qubits are placed on the horizontal lines. These actions are unitary operators called gates. Here we have the gate $R_P(\alpha) = \exp\{-i\alpha P/2\}$ with $P \in \{X, Y, Z\}$ as a parameterized gate. The parameter $\alpha$ can be varied to change the action of the gate. We also define the parametric gate $R(\alpha, \beta, \gamma) = R_X(\gamma)R_Z(\beta)R_X(\alpha)$. The third gate is called the CNOT gate which has the action of flipping the state of the qubit on which the cross is placed, if the qubit from which the line of gate starts from is in the state $|1\rangle$. Finally, the two boxes at the end represent measurement of the qubits in the $Z$ basis. This collapses the wavefunction of the qubit into either $|0\rangle$ or $|1\rangle$.*

## 3.1. Variational quantum eigensolver

### 3.1.1. Quantum circuits

The basis on which any quantum algorithm runs, including the VQE, is the quantum circuit. A quantum circuit represents a quantum state and its basis consists of qubits, which are commonly degrees of freedom described by a two-state quantum system. The qubits may start in the simple product state $|0...0\rangle$ or more generally in some initial state $|\psi_{in}\rangle$. To reach other desired states, we act on the qubits with unitary operators called gates. In Fig. 3.1 we introduce the standard quantum circuit diagrammatic notation and the relevant gates we will use in Ch. 5. An important aspect of some of our gates is that they are parameterized gates. This implies a parameter, such as an angle, controls their action. An example of parameterized quantum gates are the Pauli rotation gates $R_P(\alpha) = \exp\{-i\alpha P/2\}$, with $P \in \{X, Y, Z\}$ and $\alpha$ being the real phase parameterizing the gate. Another important gate shown in Fig. 3.1 is the CNOT gate which acts on two qubits and has the potential to create quantum entanglement.

### 3.1.2. Measuring observables

During the algorithm routine of the VQE which we will turn to shortly, we will need to make measurements of the energy observable of the quantum state represented by the quantum circuit with respect to our Hamiltonians. These Hamiltonians consist of Pauli operators, so we begin by looking at the procedure to measure the expectation value of an operator-string made up of $I$ and $Z$.

The quantum circuit state can be expanded in the qubit basis as

$$|\psi\rangle = \sum_{i=0}^{2^N-1} c_i |i\rangle . \tag{3.1}$$

In the example of $N = 2$ qubits, the notation would imply $|0\rangle = |0\rangle \bigotimes |0\rangle = |00\rangle$, $|1\rangle = |01\rangle$, $|2\rangle = |10\rangle$, $|3\rangle = |11\rangle$. Say our observable is $ZI$, then we want to calculate

$$\langle\psi| ZI |\psi\rangle = \sum_{i,i'} (ZI)_{i'i} c^*_{i'} c_i \langle i'|i\rangle = \sum_i (ZI)_{ii} |c_i|^2 . \tag{3.2}$$

Since $ZI$ is diagonal in our measurement basis, we know the elements of $(ZI)$ on the diagonal. To measure $|c_i|^2$ we need to prepare the quantum state many times and gather statistics on how frequently each bit-string is measured after the wavefunction collapses. The number of times we do this is called the number of shots. This allows us to measure our desired observable with an accuracy inversely proportional to the square root of the number of shots. This scaling behavior follows from the statistical nature of quantum measurements. The empirical probability of observing each outcome follows a binomial distribution, which, for a large number of shots $S$, can be approximated by a normal distribution with standard deviation scaling as $1/\sqrt{S}$.

Now we examine how we would measure observables which are not diagonal in the measurement basis. All we have to do in this case is to diagonalize all the operators in the given operator-string that are not diagonal and measure with respect to the modified state. To understand this concretely, we take without loss of generality the following example for one qubit

$$\langle\psi| X |\psi\rangle = \left(\langle\psi| H^\dagger\right) \left(HXH^\dagger\right) (H |\psi\rangle) \tag{3.3}$$

$$= \langle\psi'| HXH^\dagger |\psi'\rangle = \langle\psi'| Z |\psi'\rangle , \tag{3.4}$$

where $H$ is the Hadamard gate given by

$$H = \frac{1}{\sqrt{2}} \begin{bmatrix} 1 & 1 \\ 1 & -1 \end{bmatrix} . \tag{3.5}$$

This gate has the properties $HH^\dagger = I$ and $HXH^\dagger = Z$, which we have made use of in Eq. (3.3). We have seen above how to measure the last equality of Eq. (3.4), hence, we obtain the value of the first expression of Eq. (3.3).

Our Hamiltonian in Eq. (1.27) and in Eq. (1.36) is made up of a lot of Pauli operator-strings, hence, for each one we could perform the above techniques and calculate the expectation value of the sum using the expectation values of the individual terms. In practice, terms that commute with each other can be measured simultaneously, since they can be simultaneously diagonalized.

This concludes the machinery we need to run the VQE algorithm. We thus turn now to outlining the main routine that drives this algorithm.

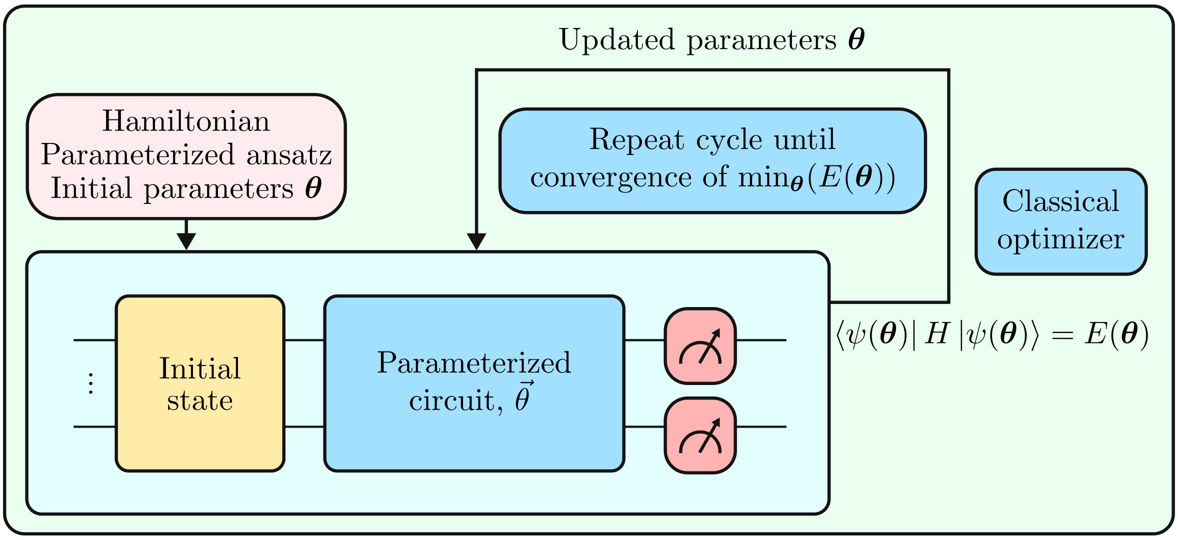
Updated parameters $\boldsymbol{\theta}$
Hamiltonian
Parameterized ansatz
Initial parameters $\boldsymbol{\theta}$
Repeat cycle until convergence of $\min_{\boldsymbol{\theta}}(E(\boldsymbol{\theta}))$
Classical optimizer
Initial state
Parameterized circuit, $\vec{\theta}$
$\langle\psi(\boldsymbol{\theta})|\, H\, |\psi(\boldsymbol{\theta})\rangle = E(\boldsymbol{\theta})$

**Figure 3.2:** *The variational quantum eigensolver (VQE) routine, as described in Sec. 3.1.3, takes as input a Hamiltonian, a parameterized quantum circuit (PQC) ansatz, and an initial set of parameters* $\boldsymbol{\theta}$*. The algorithm begins by preparing a fixed initial state and subsequently applying the parameterized circuit to this state. The energy expectation value with respect to the resulting quantum state is then measured and passed to a classical optimizer, which iteratively updates the parameters to minimize the energy. This optimization cycle continues until the energy converges to a desired threshold.*

### 3.1.3. Algorithm routine

The VQE is an optimization algorithm with the goal of optimizing a parameterized quantum circuit (PQC) such that it converges to a representation of the ground state of an input Hamiltonian, specifically for our case the Hamiltonian of Eq. (1.36). The algorithm begins by selecting an initial quantum state $|\psi_{in}\rangle$ for the qubits, which remains fixed throughout the optimization. A parametric ansatz, composed of parameterized quantum gates, is then chosen, with initial parameter values set at the start of the algorithm. These parameters are iteratively updated during the VQE routine, progressively refining the ansatz toward the ground state of the Hamiltonian. The optimization process relies on a classical optimizer, which, based on energy measurements discussed in Sec. 3.1.2, updates the parameters to minimize the system's energy. Figure 3.2 gives a diagrammatic representation of the algorithm's routine.

In our results presented in Ch. 5, we employ the limited-memory Broyden-Fletcher-Goldfarb-Shanno with box constraints (L-BFGS-B) optimizer [258], a quasi-Newton method well suited for optimizing PQCs. The L-BFGS-B algorithm efficiently updates parameters using gradient information while enforcing bounds on parameter values. Given a quantum circuit with parameters $\boldsymbol{\theta} = (\theta_1, \theta_2, \ldots, \theta_n)$, the goal is to minimize the expectation value of the observable $H$

$$C(\boldsymbol{\theta}) = \langle\psi(\boldsymbol{\theta})|H|\psi(\boldsymbol{\theta})\rangle. \tag{3.6}$$

To achieve this, the optimizer estimates the gradient $\nabla C(\boldsymbol{\theta})$ using either the parameter-shift rule or finite difference methods. A low-rank approximation of the Hessian matrix is constructed from past gradient evaluations, providing second-order information to guide parameter updates. The parameters evolve iteratively following

$$\boldsymbol{\theta}_{k+1} = \boldsymbol{\theta}_k - \alpha_k H_k^{-1} \nabla C(\boldsymbol{\theta}_k), \tag{3.7}$$

where $H_k^{-1}$ is the approximated inverse Hessian, and $\alpha_k$ is a step size determined via line search. If an updated parameter exceeds the predefined bounds $[\theta_{\min}, \theta_{\max}]$, it is projected back into the feasible range, which gives more stability in the optimization process. The algorithm continues iterating until the norm of the gradient $\|\nabla C(\boldsymbol{\theta})\|$ falls below a chosen threshold, indicating convergence.

Using L-BFGS-B for the VQE framework, we have at each iteration the evaluation of the energy multiple times to estimate the gradient of the cost function. The optimizer then updates the ansatz parameters as discussed above. The algorithm continues until the gradient norm $\|\nabla C(\boldsymbol{\theta})\|$ falls below a predefined threshold or the maximum number of iterations is reached.

## 3.2. Error Mitigation

Quantum computations are inherently susceptible to various types of errors due to noise sources such as thermal fluctuations, imperfect gate operations, and environmental disturbances. These errors can significantly degrade the accuracy of quantum algorithms, particularly on current NISQ devices. To enhance the reliability of quantum computations, effective error mitigation techniques are essential. In this section, we explore several strategies developed to mitigate different types of errors, including readout errors, incoherent noise, and coherent errors.

The subsections below describe the specific error mitigation techniques employed in Ch. 5. First, in Sec. 3.2.1, we present the TREX algorithm, a method for mitigating readout errors, which arise due to bit-flip errors during the measurement process. Next, Sec. 3.2.2 introduces ZNE, a technique designed to address incoherent noise by extrapolating results from circuits with varying noise levels to estimate the noiseless expectation values. In Sec. 3.2.3, we discuss Pauli twirling, which is used to mitigate coherent errors by transforming error channels into incoherent ones through the application of random Pauli gates. Finally, in Sec. 3.2.4, we explore the technique of dynamical decoupling, which mitigates decoherence in quantum circuits by applying controlled pulse sequences to suppress environmental noise during idle periods of qubits.

### 3.2.1. Readout Error Mitigation

As discussed in Sec. 3.1.2, measuring observables in a quantum circuit requires performing measurements that collapse the wavefunction into a bit-string. However, during this process, noise can introduce bit-flip errors, causing qubits to transition between the states $|0\rangle$ and $|1\rangle$ before measurement. As a result, a bit in the measured bit-string may be flipped. For instance, a qubit in state $|1\rangle$ may lose energy to its environment and decay to $|0\rangle$, while thermal noise may excite a qubit from $|0\rangle$ to $|1\rangle$. These errors, known as readout errors, can be effectively mitigated.

In our quantum simulations presented in Ch. 5, we employ the TREX [254] algorithm, implemented in the Qiskit library used for our simulations. The key idea behind TREX is to apply Pauli $X$ gates before measurement on randomly selected qubits and then classically invert these operations by flipping the corresponding bits in the measured bit-string. This procedure is performed for both the initial state $|0...0\rangle$ and the target state $|\psi\rangle$, repeating the process for a predefined number of runs. Once completed for these two states, the acquired data can be applied to any observable [254].

This technique, known as measurement twirling, effectively diagonalizes the readout-error transfer matrix [254], simplifying its inversion and thereby mitigating measurement errors. As a result, TREX is a robust and efficient method for readout error mitigation, making it particularly well-suited for NISQ devices.

### 3.2.2. Zero Noise Extrapolation

In addition to readout errors, another significant source of noise in quantum circuits is incoherent noise [259, 260]. To address this, we implement the ZNE algorithm [255, 261]. This technique amplifies the circuit's noise to different levels and measures the desired observable expectation value at each noise level. From these measurements, an extrapolation is performed to estimate the expectation value at the zero-noise level, which serves as an approximation to the noiseless result.

To amplify the noise, the circuit, described by the unitary $U$, can undergo a global folding with $UU^\dagger U$ [255], corresponding to a noise level of three. Higher noise levels, such as five, can be achieved by extending this approach. The noise levels are then used for the extrapolation to zero noise, yielding a more accurate estimate of the observable expectation.

An alternative method for noise amplification is local folding, or gate folding [255], which involves repeating specific gates within the circuit $U$ while preserving their original action. For example, a CNOT gate is both unitary and Hermitian, so adding two additional CNOTs after the first one amplifies the noise without altering the gate's physical effect. Noise can also be amplified by extending the duration of gate applications, such as prolonging the application of a microwave pulse that physically implements a gate in the circuit [262].

### 3.2.3. Pauli Twirling

The ZNE algorithm can only address incoherent errors, hence, to mitigate coherent errors we use the technique of Pauli twirling. This method transforms coherent quantum error channels into incoherent ones [256, 263–265]. Specifically, Pauli twirling involves inserting random single-qubit Pauli gates before and after a two-qubit gate. The purpose of these random gates is to average out the coherent errors induced by the gate, ensuring that the resulting operation behaves logically like the original two-qubit gate, but with the error channel now incoherent. The random Pauli gates are selected from the set $\{I, X, Y, Z\}$ and are applied probabilistically.

When multiple CNOT gates overlap, the sequence of single-qubit operations can often be simplified by merging consecutive gates. This reduces the total gate count and minimizes the overall circuit depth. Once the twirling is applied, the expectation value of the observables is averaged over many random instances of twirled circuits. The randomness introduced by the Pauli gates results in statistical averaging that turns coherent errors into incoherent ones, which are generally easier to mitigate. As a result, Pauli twirling effectively reduces the impact of coherent errors and improves the accuracy of the final measurement outcomes.

### 3.2.4. Dynamical Decoupling

Dynamical decoupling mitigates decoherence in quantum systems, which is a primary challenge in maintaining quantum information. Decoherence typically occurs during extended periods when qubits are idle, making them susceptible to noise and error accumulation. Crosstalk between neighboring qubits is a significant source of decoherence, as unwanted interactions can cause qubits to lose their quantum coherence. This is particularly problematic when the idle time of a qubit is comparable to its decoherence time, $T_2$ [39].

To mitigate this effect, dynamical decoupling employs a series of controlled pulse sequences that dynamically interrupt the qubit's evolution, effectively averaging out errors induced by environmental interactions [257]. These pulse sequences include operations such as spin-flip cycles, which are applied during idle periods to prevent or suppress the detrimental effects of decoherence. One commonly used sequence is the XX sequence, where two X-gates are applied to the qubit at evenly spaced intervals during the idle period. These pulses counteract the influence of unwanted interactions, such as magnetic field fluctuations or crosstalk from neighboring qubits.

The effectiveness of dynamical decoupling lies in its ability to protect qubits from noise without requiring constant active control. By applying pulse sequences at regular intervals, the qubits remain in a coherent state for longer durations, thereby increasing the fidelity of quantum computations.

# 4 Computing the mass shift of the lattice Schwinger model

In order to reach the continuum limit at fixed physical volume in lattice gauge theories (LGTs), one must extrapolate observables to their zero lattice spacing value while following lines of constant physics. This includes maintaining a fixed fermion mass. However, in the case of the Schwinger model studied in this chapter, the fermion mass undergoes a shift that depends on the number of lattice sites $N$, the inverse squared lattice spacing in units of the coupling $x = 1/(ag)^2$, the background electric field $l_0$, and, for Wilson fermions, the Wilson parameter $r$. It is therefore crucial to quantify how the mass varies with these parameters to ensure it remains fixed during continuum extrapolations. This quantification is fundamental to lattice quantum chromodynamics (QCD) to match continuum extrapolations with experimental data [266].

In this chapter, we present a method for measuring this mass shift (MS) in the Hamiltonian formulation using the electric field density (EFD) observable. Additionally, we propose the energy gap between the ground and first excited states as another means of determining the MS. Agreement between these two methods serves as a crosscheck, validating our approach. Throughout this chapter, we employ matrix product states (MPSs) to represent quantum states and matrix product operators (MPOs) to represent operators. Moreover, we utilize the density matrix renormalization group (DMRG) algorithm discussed in Sec. 2.5 to obtain the ground states of the relevant Hamiltonians.

The results presented here primarily focus on Wilson fermions, adopting a slightly different convention for the Hamiltonian given in Eq. (1.27), as clarified in Sec. 4.1. The method for computing the MS is detailed in Sec. 4.2, followed by an exploration of its dependence on various parameters in Sec. 4.3. In Sec. 4.4, we demonstrate our approach by performing the continuum extrapolation of the Schwinger boson mass and the EFD. The analytical solutions for these observables, derived within mass perturbation theory, are provided in Eq. (1.6) and Eq. (1.7), respectively. Finally, we give a brief demonstration for the EFD method with staggered fermions in Sec. 4.5.1, and further employ staggered fermions to introduce the gap method for computing the MS in Sec. 4.5.2. Both MS methods with staggered fermions are compared to a theoretical prediction for the MS [267].

This chapter's findings have already been published mainly in [59, 60], and for the energy gap method in [53], respectively as

Angelides, T., Funcke, L., Jansen, K., Kühn, S. “Computing the MS of Wilson and staggered fermions in the lattice Schwinger model with matrix product states Phys. Rev. D, 108 (1), 014516 (2023).

Takis Angelides et al. “Mass Renormalization of the Schwinger Model with Wilson and Staggered Fermions in the Hamiltonian Lattice Formulation”. In: PoS LATTICE2022 (2023), p. 046. doi: 10.22323/1.430.0046.

Guo, Y., Angelides, T., Jansen, K., Kühn, S. “Concurrent VQE for Simulating Excited States of the Schwinger Model” arXiv preprint arXiv:2407.15629 (2024).

## 4.1. Wilson fermions Hamiltonian

While Eq. (1.27) is used in Ch. 5 and Ch. 6, in this chapter, we adopt the convention from [60], where the results have been published. The key difference lies in the mapping given in Eq. (1.25). Specifically, in [60] and throughout this chapter, we take

$$\phi_{n,\alpha} \to \chi_{2n-2+\alpha}. \tag{4.1}$$

This leads to the Wilson Hamiltonian

$$\begin{aligned}
H_W = {} & ix(r-1)\sum_{n=1}^{N-1}\left(\sigma^-_{2n}\sigma^+_{2n+1} - \sigma^+_{2n}\sigma^-_{2n+1}\right) \\
& + ix(r+1)\sum_{n=1}^{N-1}\left(\sigma^+_{2n-1}Z_{2n}Z_{2n+1}\sigma^-_{2n+2}\right) - ix(r+1)\sum_{n=1}^{N-1}\left(\sigma^-_{2n-1}Z_{2n}Z_{2n+1}\sigma^+_{2n+2}\right) \\
& + l_0\sum_{n=1}^{2N-2}\left(N - \left\lceil\frac{n}{2}\right\rceil\right)Z_n + \frac{1}{2}\sum_{n=1}^{2N}\sum_{k=n+1}^{2N}\left(N - \left\lceil\frac{k}{2}\right\rceil + \lambda\right)Z_nZ_k \\
& + 2i\left(\frac{m_{\text{lat}}}{g}\sqrt{x} + xr\right)\sum_{n=1}^{N}\left(\sigma^-_{2n-1}\sigma^+_{2n} - \sigma^+_{2n-1}\sigma^-_{2n}\right) \\
& + l_0^2(N-1) + \frac{1}{4}N(N-1) + \frac{\lambda N}{2}.
\end{aligned} \tag{4.2}$$

The primary distinction from Eq. (1.27) is that, when setting the Wilson parameter to its standard choice of $r = 1$, the remaining term in the second line of Eq. (4.2) now involves four Pauli operators instead of two.

As discussed in Sec. 1.3, Wilson fermions explicitly break chiral symmetry, leading to an additive mass renormalization [60, 102, 106]. This effect is directly visible in the fourth line of Eq. (4.2), where the Wilson term modifies the mass term at the Hamiltonian level. We express the renormalized mass as

$$\frac{m_{\text{r}}}{g} = \frac{m_{\text{lat}}}{g} + \text{MS}(N, x, l_0, r). \tag{4.3}$$

Although this section focuses on Wilson fermions, in Sec. 4.5.1, we demonstrate that our method for measuring the MS is equally applicable to staggered fermions. In that case, the Wilson parameter is omitted from the dependence of the MS in Eq. (4.3).

## 4.2. Measuring the mass shift

The first method we use to measure the MS relies on the vacuum expectation value of the EFD, which we refer to as the EFD method. To compute the EFD, we use Eq. (1.24) together with Eq. (1.26), which we reiterate here for convenience

$$L_n = \epsilon_0 + \sum_{k=0}^{n} Q_k, \tag{4.4}$$

$$Q_n = (Z_{2n} + Z_{2n+1})/2. \tag{4.5}$$

. To construct the EFD observable, we evaluate it at the middle link of the lattice to mitigate boundary effects due to the use of open boundary condition (OBC), which implies evaluating Eq. (1.24) at $n = \lceil N/2 \rceil - 1$. For staggered fermions, as discussed in Sec. 4.5.1, we instead take the average over two central links to account for the staggering of charges. By combining Eq. (1.24) with Eq. (1.26), the EFD operator becomes a sum of Pauli operators that can be expressed as an MPO. The expectation value is then computed as outlined in Sec. 2.3.

We begin by measuring the EFD for various negative values of $m_{\text{lat}}/g$ close to zero while keeping all other parameters fixed. Since this method requires simulating negative mass values, standard Monte Carlo techniques would suffer from the sign problem. This provides another advantage of using MPS for our simulations. From Eq. (1.7), we expect that in the continuum limit, the EFD should vanish at $m_{\text{r}}/g = 0$. Consequently, the measured EFD also vanishes at $m_{\text{r}}/g = 0$, but this will correspond to a nonzero value of $m_{\text{lat}}/g$. This value of $m_{\text{lat}}/g$ thus represents the negative of the MS. Following Eq. (1.7), we fit a quadratic function to the EFD as a function of $m_{\text{lat}}/g$ and determine the point where it crosses the horizontal axis, yielding its zero value.

An example of this procedure for $x = 10$, $l_0 = 0.1$, and different volume sizes $N/\sqrt{x}$ is shown in Fig. 4.1, reproduced from [60]. The figure shows the EFD against $m_{\text{lat}}/g$, where $\mathcal{F}/g$ on the $y$-axis follows the notation in [60]. The data confirm that the EFD crosses the horizontal axis at a nonzero $m_{\text{lat}}/g$, yielding the negative of the MS. As the volume increases, the MS decreases and converges to a finite value.

The error bars in Fig. 4.1 stem from the termination condition of the DMRG algorithm and the extrapolation of the EFD to infinite bond dimension $D$. The former contributes an error to the EFD expectation value given by its value multiplied by $\sqrt{\eta}$, where $\eta$ is the tolerance for the fractional energy change during DMRG sweeps, as explained in Sec. 2.5. The bond dimension extrapolation was explicitly demonstrated in [61] and is shown in Fig. 4.2, where the notation $\langle L_W \rangle$ was used for the EFD of Wilson fermions, as seen on the $y$-axis.

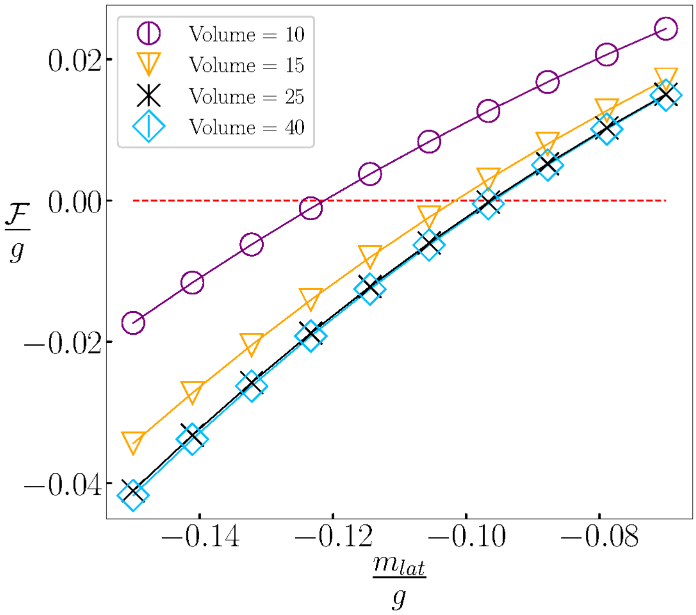

**Figure 4.1:** *$\mathcal{F}/g$ (electric field density (EFD)) versus lattice mass $m_{lat}/g$. The markers represent data for different physical volumes $N/\sqrt{x} = 10$ (purple circles), 15 (yellow triangles), 25 (black crosses), and 40 (blue squares), demonstrating the presence of finite-volume effects for the mass shift (MS). Following Eq. (1.7), the EFD vanishes for $m_r/g = 0$; therefore, the intercepts of the data curves with $\mathcal{F}/g = 0$ (red dashed line) correspond to minus the MS for a given volume. Note that the error bars are much smaller than the markers and thus, are not visible.*

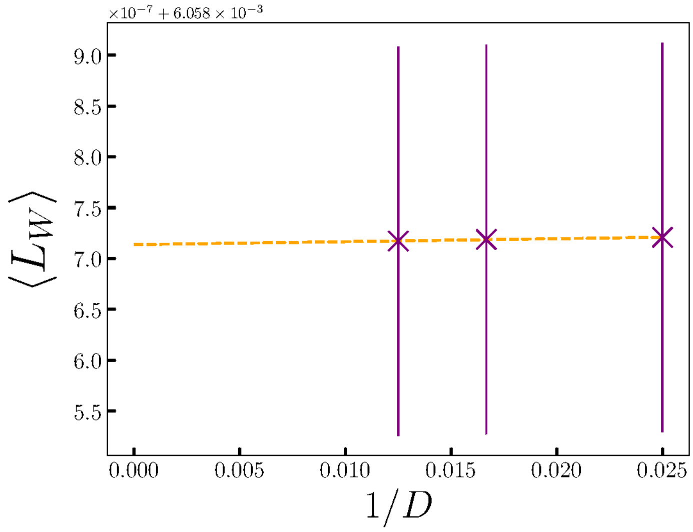

**Figure 4.2:** *$\langle L_W \rangle$ (electric field density (EFD)) against inverse bond dimension $1/D$ to extrapolate to $D \to \infty$ with $D = 40, 60, 80$. This example is for Wilson fermions at $N = 100$, $l_0 = 0.1$, $m_{lat}/g = -0.08236266$. Similar behavior was observed for staggered fermions as well. The error bars are emanating from the variational algorithm to compute the relevant ground states. As shown by the calculation on the top of the y-axis, the points are all closely converged to the value corresponding to the $D \to \infty$ limit.*

To extrapolate to $D \to \infty$, we perform a linear fit using the three largest bond dimensions. The central value is taken as the average of the extrapolated value from the fit and the EFD at the highest calculated $D$, while the uncertainty is approximated as half the difference between these values. Smaller $D$ solutions serve as initial ansätze for larger $D$, with $D = 20$ initialized from a random MPS. This bond dimension extrapolation methodology is consistently applied throughout this thesis.

## 4.3. Parameter dependence of mass shift

Equipped with the EFD method for measuring the MS, we now investigate its dependence on various model parameters, including volume and lattice spacing. Analyzing these relationships not only reveals their functional dependence but also provides deeper insights. For instance, it reinforces theoretical predictions, such as the periodicity of the model in the topological $\theta$-parameter.

### 4.3.1. Volume

To investigate the volume dependence of the MS, we set $x = 10$ and $l_0 = 0.1$, then compute the MS for different volumes $N/\sqrt{x}$, following the procedure outlined in Sec. 4.2. The results are presented in Fig. 4.3 from [60]. Initially, the MS exhibits a strong dependence on lattice volume, but it eventually stabilizes once the volume reaches approximately $N/\sqrt{x} \approx 30$. This pronounced dependence at smaller volumes is likely caused by finite-volume effects on the EFD, as explained below.

In a lattice with OBC and for state in the vanishing total charge sector, the electric field takes the value $l_0$ at both boundaries. Since the electric field across the system is governed by the fermionic charge distribution via Eq. (1.24), where the charge can only assume values $-1, 0, or 1$, a certain number of links near the left and right boundaries are necessary to establish a bulk electric field differing from $l_0$. For small volumes, a well-defined bulk region may not form, leading to finite-size effects in the EFD, which in turn influence the MS.

### 4.3.2. Lattice spacing

To extrapolate observables to the continuum limit, it is essential to evaluate their values at different lattice spacings $ag$ while keeping the renormalized mass $m_r/g$ fixed. This necessitates determining how the MS varies as a function of $ag$.

To investigate this dependence, we set $l_0 = 0.125$ and choose a volume of $N/\sqrt{x} = 30$, a value sufficiently large to suppress significant finite-size effects, as demonstrated in Sec. 4.3.1. Figure 4.4 presents our results for the MS as a function of the lattice spacing. The data indicate that, to first order, the MS exhibits a linear dependence on $ag$. Notably, we observe that the MS decreases as the continuum limit is approached, consistent with the expectation

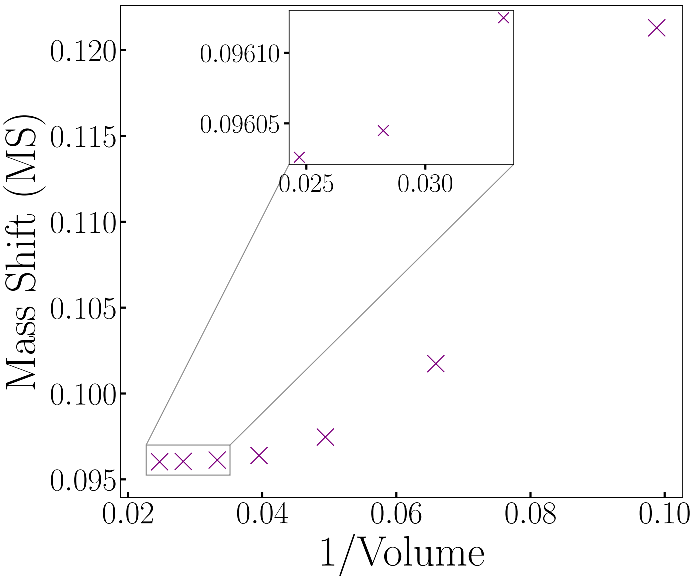

**Figure 4.3:** *Mass shift (MS) versus inverse volume. The markers show data for volumes* $N/\sqrt{x}$ *between 10 and 40, where* $x = 10$ *and* $l_0 = 0.1$ *are fixed. The MS exhibits a plateau for volumes* $N/\sqrt{x} \gtrsim 30$*, with a relative difference in the MS of* $\sim 0.01\,\%$ *for the largest two volumes of 35 and 40 (see inset). The error bars are much smaller than the markers and thus are not visible.*

that the MS vanishes in the continuum limit once the infinite volume limit is also additionally taken.

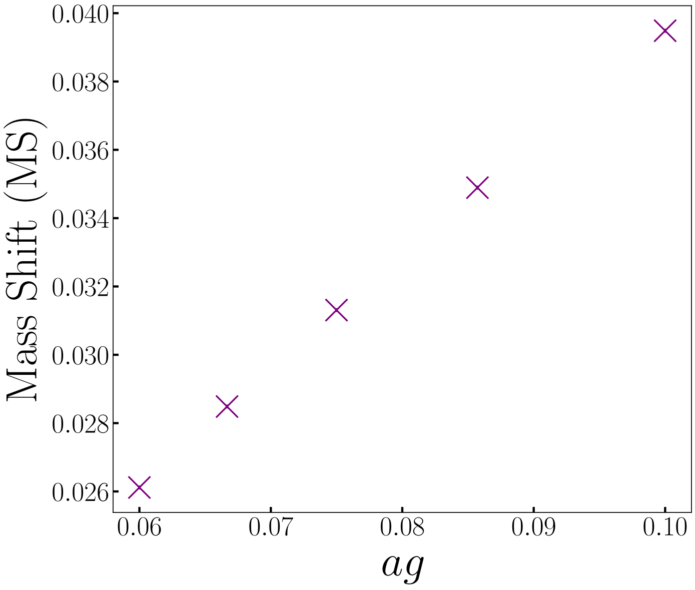

**Figure 4.4:** *Mass shift (MS) as a function of the lattice spacing* $ag$*. We fix* $l_0 = 0.125$ *and* $N/\sqrt{x} = 30$*, with* $N$ *ranging from 300 to 500. To first order, the* $ag$*-dependence of the MS is linear. As before, the error bars are much smaller than the markers and thus are not visible.*

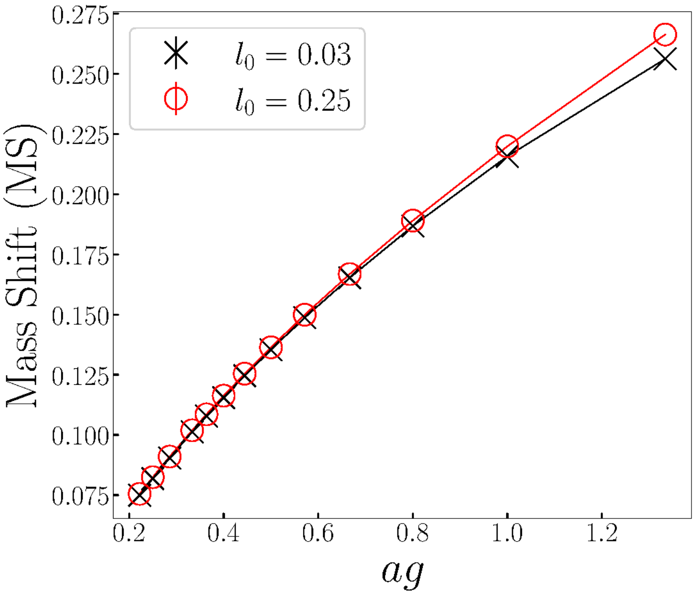

**Figure 4.5:** *Mass shift (MS) versus lattice spacing* $ag = 1/\sqrt{x}$ *for two different values of the background field,* $l_0 = \theta/(2\pi) = 0.03$ *(black crosses) and* $0.25$ *(red circles), demonstrating that the MS is different when* $l_0 = \theta/2\pi$ *varies. The volume is fixed to* $N/\sqrt{x} = 20$*, with* $N$ *ranging from 25 to 90. As before, the error bars are much smaller than the markers and thus are not visible.*

### 4.3.3. $\theta$-parameter

As discussed in Sec. 1.1, the $\theta$-parameter becomes unphysical in the continuum limit when the fermion mass vanishes. This phenomenon arises due to the axial anomaly, as reviewed in Sec. 1.1. However, on the lattice, the anomaly is not exact, leading to a residual dependence of the MS on $\theta$ when measured at $m_r/g = 0$ [46]. This effect is evident in our numerical results presented in Fig. 4.5, which illustrates the variation of the MS with lattice spacing $ag$ for two distinct values of the background field, $l_0 = \theta/2\pi$, at a fixed physical volume of $N/\sqrt{x} = 20$.

To further analyze this dependence, Fig. 4.6 depicts the difference in MS between the two chosen values of $l_0$

$$\Delta\text{MS} \equiv \text{MS}|_{l_0=0.25} - \text{MS}|_{l_0=0.03}. \tag{4.6}$$

For large lattice spacings, $ag \sim 1$, a significant $\Delta$MS is observed. However, as $ag$ decreases, this discrepancy diminishes and becomes negligible for $ag \lesssim 0.3$. This behavior is consistent with the expectation that the axial anomaly is restored in the continuum limit. It is important to note that the dependence of the MS on $l_0$ vanishes strictly in the infinite-volume limit. At finite volume, such as $N/\sqrt{x} = 20$ used here, a small residual dependence is expected, which is reflected in Fig. 4.6.

The Schwinger model exhibits periodicity in $\theta$ with a period of $2\pi$, or equivalently, in $l_0$ with a period of 1 [56], as discussed in Sec. 1.1. To verify whether this periodicity is reflected in the MS, we examine its behavior over a full period of $l_0$ from 0 to 1. As shown in Fig. 4.7, our numerical results confirm this expected periodicity. Specifically, the MS increases for

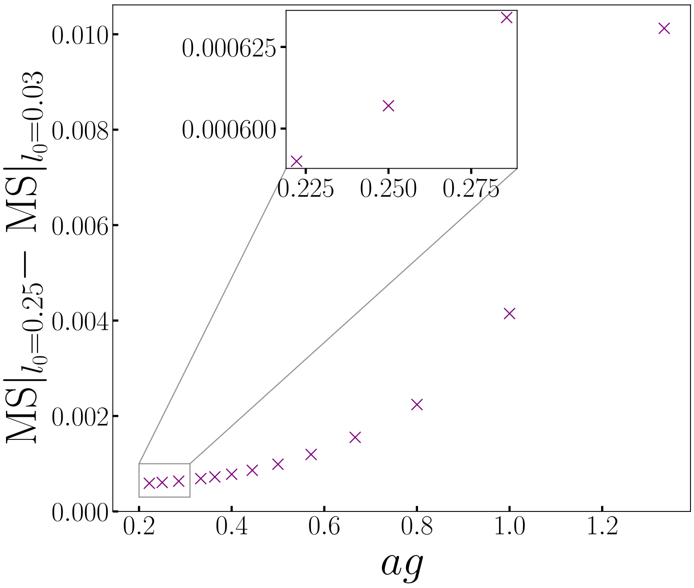

**Figure 4.6:** *Difference in mass shift (MS) between two different values of the background field, $l_0 = \theta/(2\pi) = 0.25$ and $0.03$, see Eq. (4.6), as a function of the lattice spacing $ag$. The volume is fixed to $N/\sqrt{x} = 20$, with $N$ ranging from 25 to 90. The inset shows data for $x = 1/(ag)^2 = 12.25$, 16, and 20.25, which demonstrate that the $\theta$-dependence of the mass shift (MS) becomes negligible for small ag. As before, the error bars are much smaller than the markers and thus are not visible.*

$l_0 < 0.5$, reaches a maximum at $l_0 = 0.5$, and then decreases for $l_0 > 0.5$, exhibiting symmetry about $l_0 = 0.5$, or equivalently, around $\theta = \pi$.

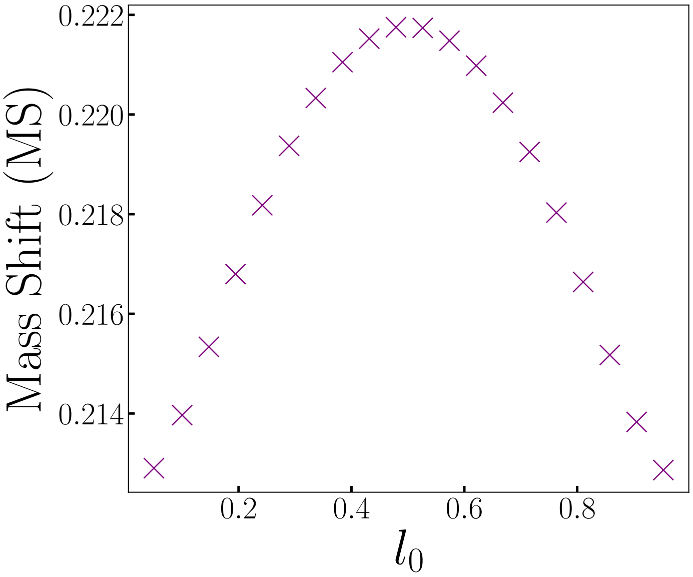

**Figure 4.7:** *Mass shift (MS) versus background electric field $l_0$. The field $l_0 = \theta/2\pi$ is swept over a full period between 0 and 1, and the MS shows the expected periodicity in $l_0$. The data points correspond to $l_0 \in [0.01, 0.9526]$, $N = 100$, and $x = 1$. As before, the error bars are much smaller than the markers and thus are not visible.*

### 4.3.4. Wilson parameter

The Hamiltonian in Eq. (1.20) exhibits a spurious symmetry under the transformation $\psi \to \gamma_5 \psi$, $m_{\text{lat}}/g \to -m_{\text{lat}}/g$, and $r \to -r$. The term "spurious" here indicates that this symmetry holds only when the Wilson parameter $r$ is also transformed. Evaluating Eq. (4.3) at $m_r/g = 0$, this symmetry implies that the MS is antisymmetric under $r \to -r$, leading to the relation

$$\text{MS}(N, x, l_0, r) = -\text{MS}(N, x, l_0, -r).$$

With our MPS approach, we can directly verify this property by analyzing the model for $r = \{-1, 1\}$, as well as for both positive and negative values of $m_{\text{lat}}/g$, while keeping $N$, $x$, and $l_0$ fixed. Our numerical results, presented in Fig. 4.8, confirm this expected behavior. Specifically, the MS obtained for $r = 1$ matches that for $r = -1$, up to the expected negative sign.

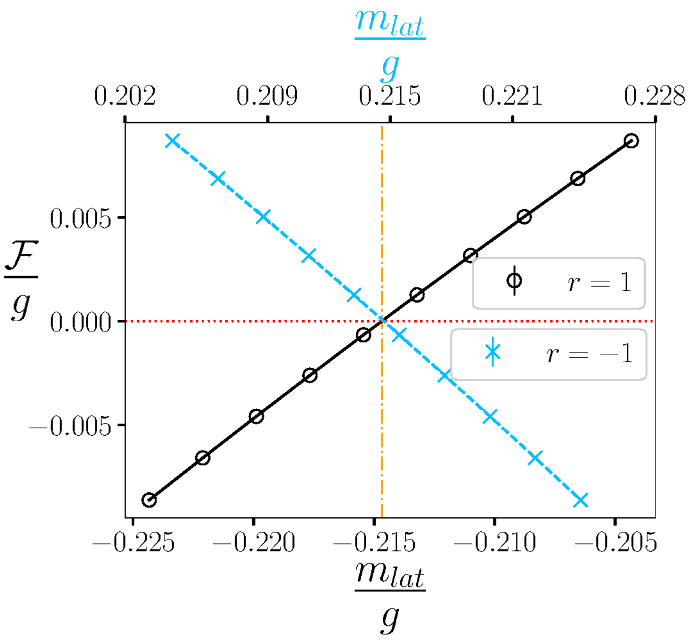

**Figure 4.8:** *$\mathcal{F}/g$ (electric field density (EFD)) as a function of the lattice mass $m_{lat}/g$ for the Wilson parameter $r = 1$ (black solid line with lower x-axis) and $r = -1$ (blue dashed line with upper x-axis). We fix $N = 100$, $x = 1$, and $l_0 = 0.125$. The horizontal red dotted line indicates $\mathcal{F}/g = 0$, and the orange dash-dotted vertical line passes the intersection point of the blue and black lines with the red dotted line. The intersection is at a value of $m_{lat}/g = 0.214681$ for $r = -1$ (upper x-axis) and $m_{lat}/g = -0.214681$ for $r = 1$ (lower x-axis). As before, the error bars are much smaller than the markers and thus are not visible.*

## 4.4. Continuum extrapolation

The following sections demonstrate the improvement in continuum extrapolations when incorporating the MS. Specifically, the EFD and Schwinger boson mass observables are extrapolated to the continuum at finite physical volume, and subsequently compared to continuum mass perturbation theory results.

### 4.4.1. Electric Field Density

We begin by analyzing the EFD in the continuum limit and comparing our numerical results with the perturbative prediction from Eq. (1.7). To do this, we fix the volume at $N/\sqrt{x} = 20$ and set $l_0 = 0.125$. After computing the MS for various values of $ag$, we extrapolate our lattice results to the continuum limit, ensuring that the renormalized mass $m_r/g$ remains constant.

Figure 4.9 illustrates this extrapolation procedure and contrasts two approaches. One approach incorporates the MS (black crosses), while the other simply keeps $m_{\text{lat}}/g$ fixed (green triangles). The difference between these two approaches highlights the significance of incorporating the MS. Without it, substantial lattice artifacts appear, making the extrapolation to $ag \to 0$ more challenging and introducing larger uncertainties in the final result. In contrast, when the MS is included, the data points are much closer to the continuum limit, as evidenced by the significantly reduced discrepancy between the extrapolated value of the EFD and the smallest $ag$ data point.

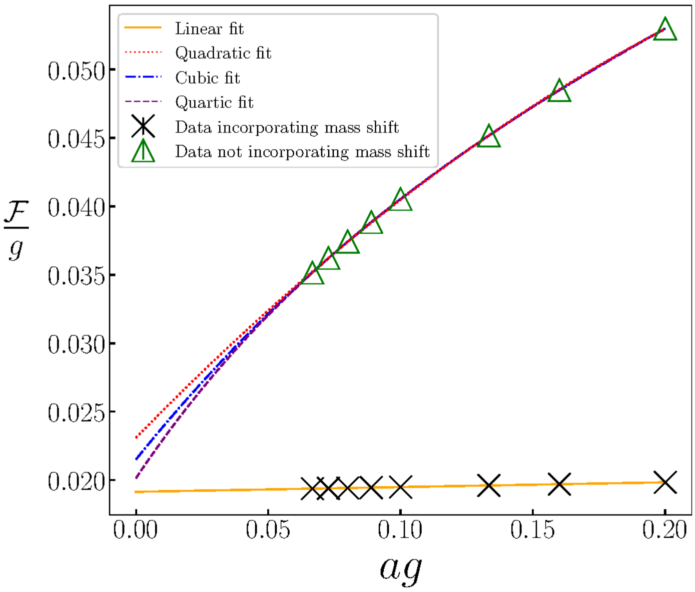

**Figure 4.9:** *$\mathcal{F}/g$ (electric field density (EFD)) as a function of lattice spacing $ag$. Black crosses represent data incorporating the mass shift (MS) for $m_r/g = 0.03$, while green triangles correspond to data without the MS, keeping $m_{lat}/g = 0.03$ fixed. We set $l_0 = 0.125$ and $N/\sqrt{x} = 20$. For data that include the MS, a linear fit suffices, as expected from the $\mathcal{O}(ag)$ scaling behavior of non-improved Wilson fermions [268]. In contrast, for data without the MS, we estimate $\mathcal{F}/g$ at $ag \to 0$ by fitting quadratic, cubic, and quartic polynomials and computing a weighted average of their $y$-intercepts. We use mean squared errors (MSEs) as weights and determine the uncertainty of each intercept using the method in Sec. 4.2. The final error is obtained by adding individual uncertainties in weighted quadrature. Error bars are too small to be visible.*

By repeating this analysis for multiple mass values, we investigate how the EFD behaves in the continuum, as shown in Fig. 4.10. This figure presents data both with and without the MS. The dataset that does not account for the MS exhibits significantly larger uncertainties, particularly for small values of $m/g$. Here, $m/g$ refers to $m_{\rm r}/g$ for the data that incorporate the MS, and to $m_{\rm lat}/g$ otherwise. While these data points are consistent with the perturbative prediction from Eq. (1.7) within error bars, their central values consistently exceed the theoretical expectation. In contrast, when the MS is incorporated, the results show significantly smaller error bars, despite using the same lattice sizes and computational resources as in the other dataset. At small $m/g$, the agreement with the perturbative prediction is excellent. As expected, at larger values of $m/g$, perturbation theory becomes less reliable, and our numerical results begin to deviate from the perturbative formula.

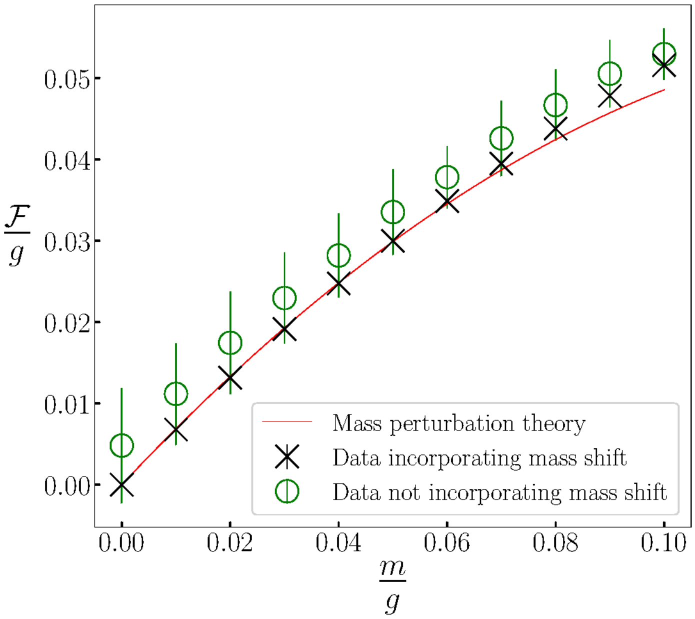

**Figure 4.10:** *$\mathcal{F}/g$ (electric field density (EFD)) extrapolated to the continuum as a function of mass $m/g$. The black crosses correspond to data that incorporate the mass shift (MS), where $m/g$ represents the renormalized mass $m_r/g = m_{lat}/g+$ MS. Green circles represent data where the MS is ignored, with $m/g = m_{lat}/g$. The red curve denotes the continuum perturbative prediction from Eq. (1.7), where $m/g$ refers to the continuum mass. The extrapolation to $ag = 0$ is performed using eight points with $N \in [100, 300]$, keeping $l_0 = 0.125$ and $N/\sqrt{x} = 20$ fixed. Error bars for the black crosses are too small to be visible.*

## 4.4.2. Schwinger Boson Mass

Next, we investigate the vector mass gap of the theory, also known as the Schwinger boson mass, in the case where $m_r/g = 0$. Using our dimensionless Hamiltonian from Eq. (4.2), and denoting $E_0$ and $E_1$ as the energies of the ground and first excited states, respectively, the

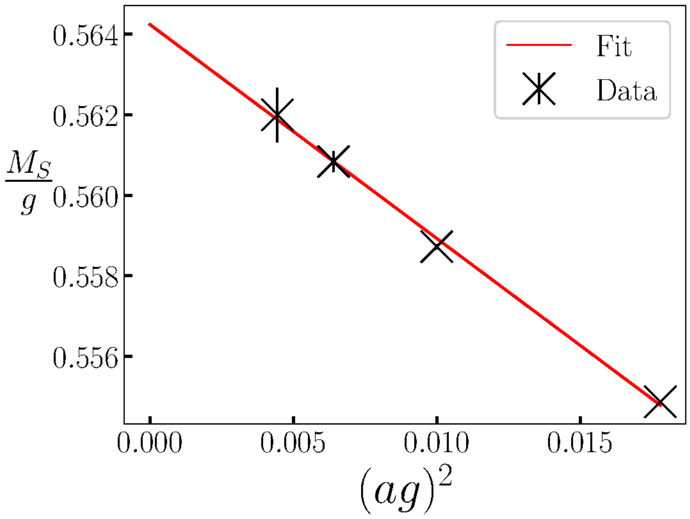

**Figure 4.11:** *Schwinger boson mass (vector mass gap), $M_S/g$, as a function of the squared lattice spacing, $(ag)^2$. The data points (black crosses) correspond to $l_0 = 0.125$ and $m_r/g = 0$, with a fixed volume of $N/\sqrt{x} = 40$ for $N \in [300, 600]$. A quadratic fit in $ag$ (red line) yields an extrapolated value of $M_S/g = 0.5642 \pm 0.0011$, which aligns with the theoretical expectation $M_S/g = 1/\sqrt{\pi} \approx 0.5641$ from Eq. (1.6).*

Schwinger boson mass in units of the coupling constant is given by [210]

$$\frac{M_S}{g} = \frac{1}{2\sqrt{x}}(E_1 - E_0) - \frac{2m_r}{g}. \tag{4.7}$$

To reach the continuum limit, we compute this quantity for various values of $ag$ and extrapolate to $ag \to 0$, following a procedure similar to that used for the EFD. Figure 4.11 presents the extrapolation results for $m_r/g = 0$ and $l_0 = 0.125$.

For the extrapolation, we use a quadratic fit in $ag$, shown as the red line in Fig. 4.11. This choice is justified for two reasons. First, for non-improved Wilson fermions [268], observables such as energy and EFD exhibit $\mathcal{O}(ag)$ corrections, as illustrated in Fig. 4.9. Second, Eq. (4.7) introduces an additional factor of $ag$ in our dimensionless formulation, which results in leading-order corrections that scale as $(ag)^2$. Using this quadratic fit, we obtain an extrapolated value of $M_S/g = 0.5642 \pm 0.0011$, which is in excellent agreement with the theoretical prediction $M_S/g = 1/\sqrt{\pi} \approx 0.5641$ from Eq. (1.6).

## 4.5. Staggered fermions

In the following subsections we explore the EFD method as applied to staggered fermions. Further, we go beyond the EFD method and introduce another observable which can be used to measure the MS, namely the energy gap between the ground and first excited states. The two methods to compute the MS are then compared against each other and to theoretical predictions.

### 4.5.1. Electric field density method for staggered fermions

This section extends our method for computing the MS beyond the case of Wilson fermions, specifically applying it to staggered fermions given by Eq. (1.36), which are commonly used in LGT simulations with tensor network (TN) and quantum computing.

A recent analytical study [267] derived the additive mass renormalization for staggered fermions in a system with periodic boundary conditions. This derivation relied on a discrete chiral symmetry, which consists of a one-site translation combined with a shift of $\theta$ by $\pi$. The resulting MS is given by

$$\frac{m_r}{g} = \frac{m_{\text{lat}}}{g} + \frac{1}{8\sqrt{x}}. \tag{4.8}$$

Applying Eq. (4.8) ensures that the Hamiltonian preserves the remnant discrete chiral symmetry described above. This symmetry originates from the chiral anomaly discussed in Sec. 1.1. Specifically, the anomaly implies via Eq. (1.11) that, in the massless limit, $H_S$ in Eq. (1.34) with a nonzero $\theta$-parameter is unitarily equivalent to $H$ with $\theta = 0$. The chiral symmetry then maps $H_S$ at $\theta$ to $H_S$ at $\theta+\pi$, but only when the bare lattice mass is set to $m_{\text{lat}}/g = -1/(8\sqrt{x})$, ensuring that the renormalized mass satisfies $m_{\text{r}}/g = 0$. This requirement directly leads to the MS presented in Eq. (4.8).

Following the procedure outlined in Sec. 4.2, we numerically compute the MS by identifying the point where the EFD vanishes, corresponding to $m_r/g = 0$. Figure 4.12 shows our results for staggered fermions using OBC. For smaller system sizes, deviations from Eq. (4.8) are observed, which is expected due to the effects from boundary conditions. However, as the system size increases, the boundary effects diminish, and the data converge toward the theoretical prediction.

### 4.5.2. Energy gap method

Beyond the EFD method for computing the MS, we present in [53] an alternative approach, referred to as the gap method, which utilizes the energy gap of the model. The advantage of this method to the EFD method, is that it can be applied at $\theta = 0, \pi$, which are relevant points in the phase diagram. The demonstration from [53] for the gap method uses staggered fermions as given in Eq. (1.36).

In the continuum Schwinger model, mass perturbation theory predicts that, at $m_{\text{r}}/g = 0$, the Schwinger boson mass satisfies $M_S/g = 1/\sqrt{\pi}$, as given by Eq. (1.6). To determine the MS, we determine the value of $m_{\text{lat}}/g$ for which $\frac{M_S}{g} - 1/\sqrt{\pi}$ vanishes, corresponding to the condition $m_{\text{r}}/g = 0$. Consequently, this value of $m_{\text{lat}}/g$ directly yields the negative of the MS.

On the lattice, we use the following equation, which was introduced in a previous section

$$\frac{M_S}{g} = \frac{E_1 - E_0}{2\sqrt{x}} - 2\frac{m_{\text{r}}}{g}, \tag{4.9}$$

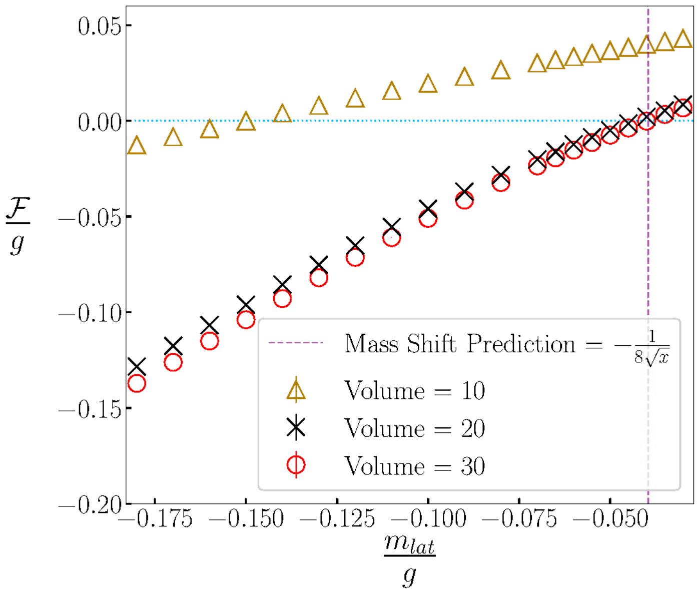

**Figure 4.12:** *$\mathcal{F}/g$ (electric field density (EFD)) as a function of the lattice mass $m_{lat}/g$ for staggered fermions, with $x = 10$ and $l_0 = 0.125$. The horizontal blue dotted line marks the point where the EFD vanishes, while the vertical purple dashed line represents the theoretical prediction for the mass shift (MS) from Ref. [267]. Different markers indicate data for various physical volumes: $N/\sqrt{x} = 10$ (yellow triangles), 20 (black crosses), and 30 (red circles). The error bars, stemming from the extrapolation in bond dimension, are too small to be visible.*

where $E_0$ and $E_1$ are the energies of the ground and first excited states, respectively, for the Hamiltonian under consideration.

In [53], where we introduced this method, we computed the point at which $\frac{M_S}{g} - 1/\sqrt{\pi}$ becomes zero by employing the bisection method [269]. This can be expressed in equation form with a given fixed $m_{\text{lat}}/g$ as

$$\frac{M_S}{g}(m_{\text{lat}}/g) = 1/\sqrt{\pi}. \tag{4.10}$$

Additionally, we applied the bisection method to compute the MS using the EFD, with the details of the algorithm provided in [53]. Figure 4.13 compares the MS values computed using the gap and EFD methods for various values of $1/\sqrt{x}$, with the data extrapolated to infinite volume for $l_0 = 0, 0.08$. On the $y$-axis, the MS is denoted as $m_s/g$ following [53]. The theoretical prediction for the MS of staggered fermions from [267] is also included. As $x$ increases, all three MS values converge, and the extrapolated values in the figure's legend are consistent with the MS approaching zero at infinite volume in the continuum limit.

Finally, we have employed the concurrent variational quantum eigensolver (cVQE) algorithm to compute the ground and first excited states, enabling the computation of the MS on a quantum computer. The details of this algorithm are outside the scope of this thesis and can be found in [53]. In Figure 4.14, we directly present the results of this computation, where the observable $\frac{M_S}{g} - 1/\sqrt{\pi}$ is plotted against $m_{\text{lat}}/g$, for $l_0 = 0, 0.08$, at $x = 1$, and a fixed volume

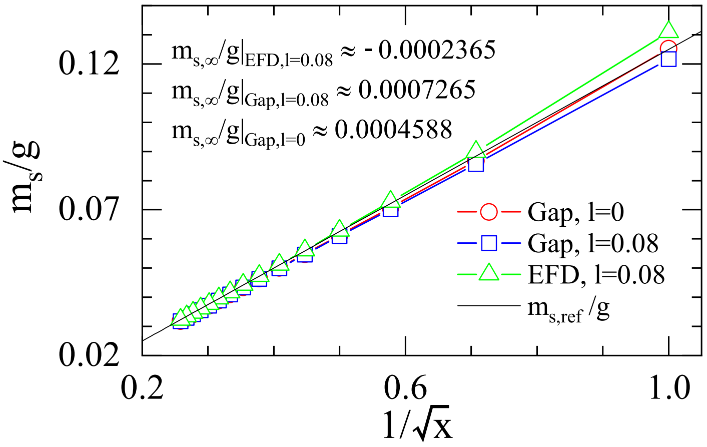

**Figure 4.13:** *The behavior of $m_s/g$ (mass shift (MS)) as a function of $1/\sqrt{x}$ for $l_0 = 0$ (red circles) and $l_0 = 0.08$ (blue squares), where $l \equiv l_0$ for this plot. The mass shift (MS) is estimated using the gap method by solving Eq. (4.10) for various $N$ using matrix product state (MPS), followed by extrapolation to infinite volume for a fixed $x$. For comparison, results from the electric field density (EFD) method are also shown for $l_0 = 0.08$ (green triangles). The black line represents the analytically computed value $1/(8\sqrt{x})$ from Ref. [267] for periodic boundary conditions.*

of $N/\sqrt{x} = 40$. The figure also compares results from two different amounts of layers in the cVQE ansatz, which is the number of times the motif ansatz is repeated to form the complete parameterized ansatz, in line with the variational quantum eigensolver (VQE) described in Sec. 3.1.3. Although the cVQE here has been simulated with TN methods, it demonstrates the capability of quantum computing algorithms for computing the MS. The figure shows good agreement between the cVQE results and those obtained from MPS with DMRG. We note that, following the convention of [53], the notation $\Delta(m_{\text{lat}}/g) = E_1 - E_0$ is used on the figure's $y$-axis.

In conclusion, the EFD method for measuring the MS only requires the calculation of the ground state, in comparison to the gap method which additionally requires the calculation of the first excited state. On the other hand, the EFD method cannot be applied at $\theta = 0, \pi$, where the EFD is zero for all masses. This is an advantage to the gap method which can indeed be applied at these $\theta$ values that are commonly relevant due to the phase transitions at $\theta = \pi$.

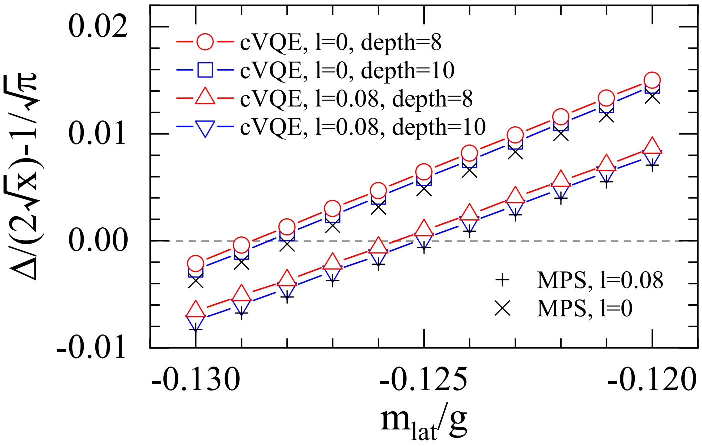

**Figure 4.14:** *Results for $\Delta/(2\sqrt{x}) - 1/\sqrt{\pi}$ versus $m_{lat}/g$ for 40 physical qubits and $x = 1$ from concurrent variational quantum eigensolver (cVQE) (open symbols) and a direct matrix product state (MPS) calculation ($\times$, $+$) for comparison, where $\Delta$ is the energy gap $E_1 - E_0$. The red circles (blue squares) and red triangles (blue lower triangle) correspond to results for $l_0 = 0$ and $l_0 = 0.08$, respectively, for eight (ten) layers of the ladder ansatz from Fig. 3(b). The black "$\times$" ("$+$") represent data from a direct MPS calculation with bond dimension $D = 40$, serving as the reference value for $l_0 = 0$ ($l_0 = 0.08$). The dashed line marks $\Delta/(2\sqrt{x}) - 1/\sqrt{\pi} = 0$, and its intersection with the cVQE data provides an estimate of the mass shift (MS), up to a minus sign.*

# 5 | First-order phase transition of the Schwinger model with a quantum computer

In this chapter, we investigate the feasibility of studying the phase structure of the Schwinger model [87] with a topological $\theta$-term using noisy intermediate-scale quantum (NISQ) devices. Understanding phase diagrams is crucial in physics, particularly in the context of quantum chromodynamics (QCD), where they provide insights into matter under extreme conditions, with implications for the early universe and neutron stars [270]. Given the rich theoretical background introduced in Sec. 1.1, the Schwinger model serves as an ideal benchmark for developing and validating novel computational techniques. Moreover, quantum computing presents an alternative to Monte Carlo and tensor network (TN) approaches [220, 222], offering key advantages such as avoiding the sign problem, which is an inherent limitation of Monte Carlo methods [24, 271], and having the potential to efficiently represent highly entangled quantum states that would be challenging with TN techniques, as discussed in Sec. 2.1.

Beyond the successful demonstrations of quantum simulations [77, 80–83, 169, 217–219], applying quantum computing to the lattice Schwinger model raises several open questions. First, since the theory must be discretized on a finite lattice, multiple fermion discretization schemes exist, and determining the most efficient scheme given available computational resources is nontrivial. Second, assessing the minimum system sizes required for a reliable continuum extrapolation is essential for evaluating the practicality of near-term quantum devices.

To address these challenges, we analyze two fermion discretization schemes introduced earlier in this thesis, namely staggered and Wilson fermions, to determine their relative advantages as applied to the lattice Schwinger model. We employ the variational quantum eigensolver (VQE) [251] and develop a protocol for mapping this problem onto a quantum circuit. Originally introduced as an alternative to quantum phase estimation [272], the VQE is well suited to the capabilities of current and near-term quantum hardware. We validate our VQE approach through noiseless classical simulations on system sizes ranging from 6 to 12 qubits, optimizing the ansatz and gate configurations to efficiently capture the relevant ground states. Once the optimal ansatz-gate combination and variational parameters are established, we prepare ground states across the first-order phase transition shown in Fig. 1.2 using IBM's quantum devices.

Additionally, we demonstrate that employing state of the art error mitigation techniques discussed in Sec. 3.2, including zero-noise extrapolation [255], readout error mitigation [254], Pauli twirling [265], and dynamical decoupling [257], enables accurate results from quantum measurements. Finally, to determine the system sizes required for a reliable continuum extrapolation on quantum hardware, we leverage matrix product state (MPS). By performing numerical simulations of intermediate system sizes, we conduct continuum extrapolations and compare the results with analytical predictions.

This chapter is organized as follows. In Sec. 5.1, we introduce the key observables used to track the first-order phase transition. In Sec. 5.2, we describe the parametric circuits employed as ansätze for the VQE. The error mitigation techniques utilized in quantum hardware calculations are detailed in Sec. 5.6. We present the performance results of the selected ansätze in Sec. 5.3, followed by an analysis of lattice effects on the position of the first-order phase transition in Sec. 5.4. Finally, in Sec. 5.5, we report the results of state preparation on quantum hardware and the measurement of relevant observables, while Sec. 5.7 provides the final results for the continuum limit calculations.

The chapter's findings have already been published in [61] as

Angelides, T., et al. "First-order phase transition of the Schwinger model with a quantum computer". *npj Quantum Information* 11.1 (2025), p. 6. doi: 10.1038/s41534-024-00950-6.

## 5.1. Observables

As discussed in Sec. 1.1, moving across the first-order phase transition shown in Fig. 1.2 at large $m_\mathrm{r}/g$, reduces the electric field by one unit and raises the particle number (PN) by two. This motivates tracking the electric field density (EFD) and PN, as we change $l_0$ at fixed $m_\mathrm{lat}/g$. Since our calculations in this chapter are not focused on continuum extrapolations, we make the approximation $m_\mathrm{r}/g = m_\mathrm{lat}/g$, except for Sec. 5.7, where we perform continuum extrapolations with MPS.

For Wilson fermions, the EFD, given the notation $L_W$ is taken to be

$$\begin{aligned} L_W = l_0 + L_{\lceil \frac{N}{2} \rceil - 1} &= l_0 + \sum_{k=0}^{\lceil N/2 \rceil - 1} Q_k \\ &= l_0 + \frac{1}{2} \sum_{k=0}^{\lceil N/2 \rceil - 1} (Z_{2k} + Z_{2k+1}), \end{aligned} \tag{5.1}$$

which follows from Eq. (1.24). The PN for Wilson fermions, given the notation $P_W$, can be calculated from the operator

$$P_W = N + \frac{1}{2} \sum_{n=0}^{N-1} \left( X_{2n} X_{2n+1} + Y_{2n} Y_{2n+1} \right). \tag{5.2}$$

This operator does not generally commutes with the Hamiltonian. However, it does commute with the Hamiltonian in the absence of the kinetic term, which can be considered the infinite mass limit. Consequently, in this heavy mass regime, the integer eigenvalues of $P_W$ are expected to be good quantum numbers [66]. Each of the two components in the sum of Eq. (5.2) contributes at least $-1$, meaning that the total sum, including the prefactor, has a minimum value of $-N$. This corresponds to the negative of the number of two-component Dirac spinor lattice sites. Therefore, with the first term $N$, the minimum value of this operator is shifted to 0.

For staggered fermions, the EFD, denoted as $L_S$, is given by

$$\begin{aligned} L_S &= l_0 + \frac{1}{2}\left(L_{N/2-2} + L_{N/2-1}\right) \\ &= l_0 + \frac{1}{2}\left(\sum_{k=0}^{N/2-2} Q_k + \sum_{k=0}^{N/2-1} Q_k\right) \\ &= l_0 + \frac{1}{4} + \frac{1}{2}\sum_{k=0}^{N/2-2} Z_k + \frac{1}{4} Z_{N/2-1}. \end{aligned} \tag{5.3}$$

Similarly, the PN operator takes the form

$$P_S = \frac{N}{2} + \frac{1}{2}\sum_{n=0}^{N-1}(-1)^n Z_n. \tag{5.4}$$

In the absence of particles, i.e., when the system is in a state where spins are down on even sites and up on odd sites, the sum in Eq. (5.4) contributes $-1$ for every site. Conversely, when spins are up on even sites and down on odd sites, the sum contributes $+1$. The first term in Eq. (5.4) ensures that $P_S$ remains positive semi-definite.

## 5.2. Parametric circuits

In order to evaluate the performance of different discretization schemes for the VQE, we consider two distinct parametric ansätze and two types of parametric gates, as illustrated in Fig. 5.1 from [61]. The ansatz architectures, referred to as "brick" and "ladder", are shown in Fig. 5.1$(c, d)$ respectively, and employ either SO(4) gates or $R_{XX+YY}$ gates. The decomposition of these gates into CNOT and Pauli rotation gates is depicted in Fig. 5.1$(a, b)$ respectively.

We choose SO(4) instead of SU(4) gates because the Hamiltonians used for this chapter are real, meaning their ground states are also real. These are given explicitly in Eq. (1.27) and Eq. (1.36). Thus, we can restrict our ansätze to the real subspace of the Hilbert space. While SO(4) gates are more expressive due to their additional tunable parameters, they do not conserve the total charge, as they can implement any two-qubit orthogonal operation that may alter the charge. In contrast, using the algebra of Pauli operators, one can verify that the total charge operator commutes with $R_{XX+YY}$, ensuring charge conservation. Consequently,

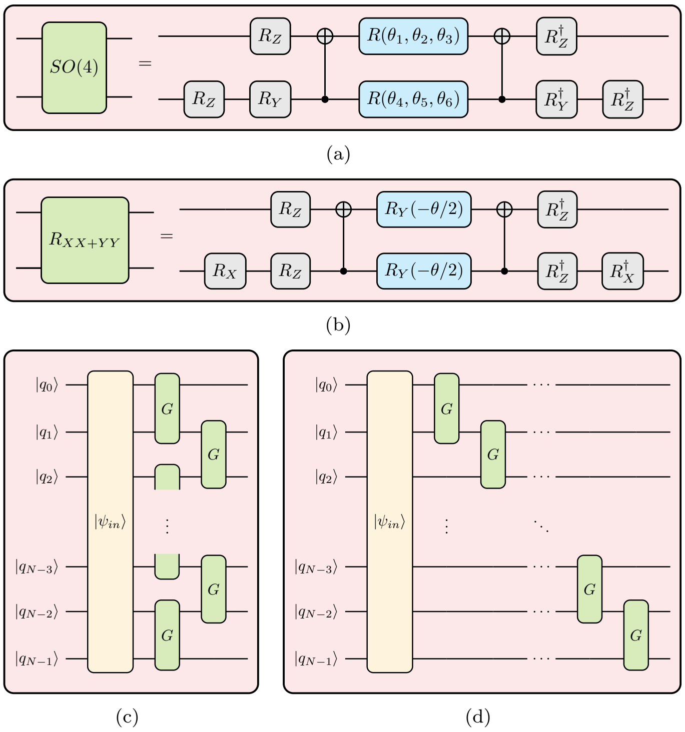
$SO(4)$
=
$R_Z$
$R_Z$
$R_Y$
$R(\theta_1, \theta_2, \theta_3)$
$R(\theta_4, \theta_5, \theta_6)$
$R_Z^\dagger$
$R_Y^\dagger$
$R_Z^\dagger$
(a)
$R_{XX+YY}$
=
$R_Z$
$R_X$
$R_Z$
$R_Y(-\theta/2)$
$R_Y(-\theta/2)$
$R_Z^\dagger$
$R_Z^\dagger$
$R_X^\dagger$
(b)
$|q_0\rangle$
$|q_1\rangle$
$|q_2\rangle$
$|q_{N-3}\rangle$
$|q_{N-2}\rangle$
$|q_{N-1}\rangle$
$|\psi_{in}\rangle$
G
(c)
$|q_0\rangle$
$|q_1\rangle$
$|q_2\rangle$
$|q_{N-3}\rangle$
$|q_{N-2}\rangle$
$|q_{N-1}\rangle$
$|\psi_{in}\rangle$
G
(d)

**Figure 5.1:** *Decomposition of a generic SO(4) gate depending on the six parameters* $\theta_1, \dots, \theta_6$ *(a) the* $R_{XX+YY}(\theta) = R_{Z_0} \exp(-i\theta(XX+YY)/2) R_{Z_0}^\dagger$ *(b), into CNOT and Pauli rotation gates. The* $R_{Z_0}$ *rotations in the definition of* $R_{XX+YY}(\theta)$ *restrict the state to the real subspace. Boxes acting on a single qubit correspond to Pauli rotation gates,* $R_P(\alpha) = \exp\{-i\alpha P/2\}$ *with* $P \in \{X, Y, Z\}$*. Single-qubit gates where the argument is omitted refer to rotations around an angle* $\pi/2$*,* $R_P(\pi/2)$*. The light blue boxes represent the parameterized gates which are* $R(\alpha, \beta, \gamma) = R_X(\gamma) R_Z(\beta) R_X(\alpha)$ *in (a) and* $R_Y(\theta)$ *in (b). Panel (c) and (d) illustrate one layer of the brick and ladder ansatz, respectively, both following a non-parametric part for preparing the initial state* $|\psi_{in}\rangle$ *(yellow box). The first layer in the brick ansatz has a CNOT-depth of* $4$ *whereas in ladder it is* $2n-2$*, where* $n$ *is the number of qubits, and in both cases it increases by* $4$ *with each layer.*

when employing SO(4) gates, we must explicitly enforce charge neutrality by adding a penalty term to the Hamiltonians as introduced in Sec. 1.3

$$\lambda \left( \sum_{n=0}^{N-1} Q_n \right)^2 . \tag{5.5}$$

The Lagrange multiplier $\lambda$ must be chosen sufficiently large to ensure a ground state with vanishing total charge. On the other hand, the $R_{XX+YY}$ gate naturally preserves the total charge but is generally less expressive.

Throughout our simulations, we initialize the parameters for the parametric portion of the ansatz randomly within the interval $[0, 0.001)$ to keep the circuit close to the identity, ensuring the VQE starts from a state near the initial state $|\psi_{in}\rangle$ forming the non-parametric part of the circuit.

For Wilson fermions, we test three possible initial states $|\psi_{in}\rangle$, adopting the one that yields the best fidelity in the VQE. As discussed in Sec. 1.1, for $m/g \gg 1$ and $\theta < \pi$, the continuum Hamiltonian is expected to be dominated by the mass term, with a ground state approximated by the ground state of that term. The lattice analog for the Wilson case is

$$\left( \frac{|01\rangle - |10\rangle}{\sqrt{2}} \right)^{\otimes N} . \tag{5.6}$$

This state carries no net charge and serves as a suitable initial state for large masses before the first-order phase transition occurs.

For $\theta > \pi$, the continuum model predicts the creation of a particle-antiparticle pair, with a negative (positive) charge forming on the left (right) boundary. On the lattice, this corresponds to the state

$$|11\rangle \left( \frac{|01\rangle - |10\rangle}{\sqrt{2}} \right)^{\otimes (N-2)} |00\rangle , \tag{5.7}$$

which approximates the expected state after the phase transition. Additionally, we test a generic charge-neutral initial state, $|10\rangle^{\otimes N}$. In all cases, a simple linear mapping of the logical qubits $|\sigma_l\rangle$ in the model Hamiltonian to the physical qubits $|q_l\rangle$ of the hardware is applied.

For staggered fermions, the charge-neutral ground state at large $m/g \gg 1$ corresponds to $|10\rangle^{\otimes N/2}$, making it a viable choice for $|\psi_{in}\rangle$ when $\theta < \pi$. For $\theta > \pi$, a charge pair forms, with the negative (positive) charge residing on odd (even) sites. This places the charges at sites 1 and $N-2$, leading to the state

$$|11\rangle \, |10\rangle^{\otimes (N-2)/2} \, |00\rangle . \tag{5.8}$$

This state can be efficiently prepared from $|10\rangle^{\otimes N/2}$ by applying an SO(4) or $R_{XX+YY}$ gate between qubits 1 and $N-2$. However, the ansätze shown in Fig. 5.1 do not include direct two-qubit interactions between these qubits. To address this, we modify the standard linear mapping of logical qubits to physical hardware qubits, using the transformation:

$$\begin{aligned} |q_0\rangle \otimes |q_1\rangle \otimes \cdots \otimes |q_{N-1}\rangle \equiv |\sigma_{(N-2)/2+1}\rangle \otimes \cdots \otimes |\sigma_{N-3}\rangle \otimes |\sigma_{N-1}\rangle \\ \otimes |\sigma_{N-2}\rangle \otimes |\sigma_1\rangle \otimes |\sigma_0\rangle \otimes |\sigma_2\rangle \otimes \cdots \otimes |\sigma_{(N-2)/2}\rangle \,. \end{aligned} \tag{5.9}$$

This mapping ensures a direct two-qubit gate between logical qubits 1 and $N-2$. For $m/g \ll 1$, where the ground state partially screens the electric field, there are no expectations that would motivate any other mapping, and thus we use $|10\rangle^{\otimes N/2}$ with the standard linear mapping.

To assess the ansätze for different discretizations, we first simulate the VQE classically. We employ the limited-memory Broyden-Fletcher-Goldfarb-Shanno with box constraints (L-BFGS-B) optimizer [258] with two heuristic warm-start stages. In the first stage, all variational parameters within a layer are grouped and optimized collectively over 2000 iterations, leveraging approximate translation invariance. Despite open boundary conditions (OBCs) breaking exact translation symmetry, this serves as a reasonable approximation. In the second stage, each parameter is optimized independently over 100,000 iterations to evaluate the full expressive power of each ansatz. In practice, convergence typically occurs within a few hundred iterations.

For deeper circuits, we adopt a progressive warm-start approach. After optimizing an ansatz with $k$ layers, its optimal warm-start parameters are used to initialize the first $k$ layers in the warm-start stage of the optimization of an ansatz with $k+1$ layers.

## 5.3. Comparison of parametric circuits with VQE

To assess the ability of our ansatz to accurately represent the ground states, we perform classical simulations of the VQE in the absence of noise, following the procedure outlined in Sec. 3.1.3 and Sec. 5.2. We then focus on two regimes, with the first being a large mass ratio of $m_{\text{lat}}/g = 10$, where the first-order quantum phase transition is expected, and the second being $m_{\text{lat}}/g = 0$, which is significantly below the critical mass and should therefore exhibit no transition as $l_0$ varies. Throughout this section, we fix the lattice volume at $N/\sqrt{x} = 30$.

We first analyze the case of Wilson fermions, where both the brick and ladder ansatz yield similar performance. The use of SO(4) gates generally results in slightly higher fidelities compared to $R_{XX+YY}$ gates, irrespective of the mass. Given that the brick ansatz has a lower CNOT-depth than the ladder ansatz for the same number of layers, it is better suited for NISQ devices. Thus, we focus on the brick ansatz with SO(4) gates for the Wilson discretization.

For $m_{\text{lat}}/g = 10$, using the two product states described in Sec. 5.2 as initial states before and after the transition, the VQE achieves fidelities exceeding 0.99 with a single layer of the brick ansatz for all system sizes considered. Figure 5.2 from [61] presents the results for the EFD, $\langle L_W\rangle$, and the PN, $\langle P_W\rangle$, as functions of $l_0$ for system sizes $N = 3, 4, 5, 6$, corresponding to 6, 8, 10, and 12 qubits, respectively. The VQE results exhibit a clear discontinuity in both

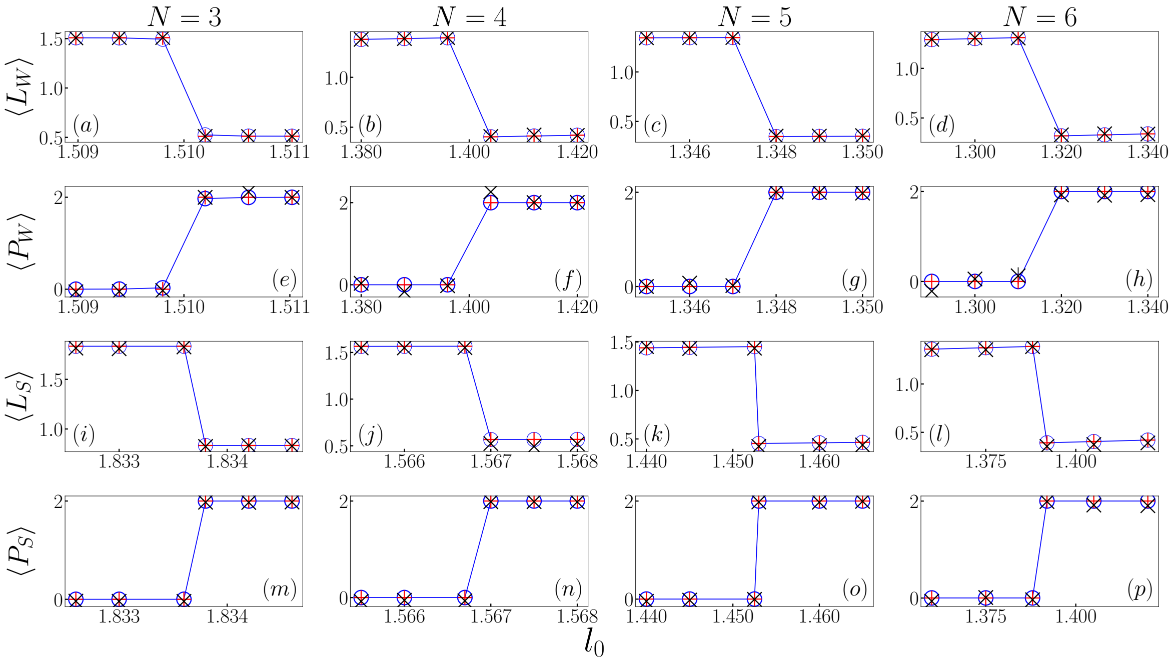

**Figure 5.2:** *Electric field density (EFD) $\langle L_{W,S} \rangle$ and particle number (PN) $\langle P_{W,S} \rangle$ against $l_0$ with data from quantum hardware (black crosses), as compared to the noiseless expectation values (red pluses) and exact diagonalization (blue circles) for Wilson and staggered fermions respectively. The staggered fermions in this case have the same number of qubits as the Wilson fermions. Hence, while the title of each column specifies the $N$ for Wilson fermions, for staggered it is taken to be double that value. The lattice mass for these data is set to $m_{lat}/g = 10$, so that we are above the second order phase transition of Fig. 1.2, without having to account for the mass shift (MS). Therefore, we can observe the first-order phase transition. Note that the error bars, which are discussed in Sec. 5.4, are much smaller than the y-scale and thus, are not visible.*

quantities, signaling the remnant of the first-order phase transition. The transition occurs at values of $l_0$ significantly larger than the continuum prediction, $l_0 = 1/2$. However, as $N$ increases, the transition point shifts toward smaller values of $l_0$, a behavior attributable to finite volume and lattice spacing effects, which we discuss in detail in Sec. 5.4. Specifically, increasing $N$ while keeping the volume constant effectively reduces the lattice spacing, bringing the result closer to the continuum limit. Comparison with exact diagonalization results shows excellent agreement, reflecting the high fidelities achieved. This agreement arises because, for $m_{\text{lat}}/g = 10$, the true ground states before and after the transition are close to the product states used as initial states, requiring only a single ansatz layer to achieve near-perfect overlap.

For $m_{\text{lat}}/g = 0$, the ground state is more complex, requiring additional ansatz layers for similar fidelity levels. Generally, two layers of the brick ansatz with SO(4) gates provide optimal performance, achieving fidelities above 0.99. In some cases, the $R_{XX+YY}$ gates perform slightly better, and in a few instances, a single ansatz layer suffices. Figure 5.3 from [61] summarizes the EFD and PN results for this mass regime. Unlike the large-mass case, both quantities exhibit smooth variations, consistent with expectations for masses below

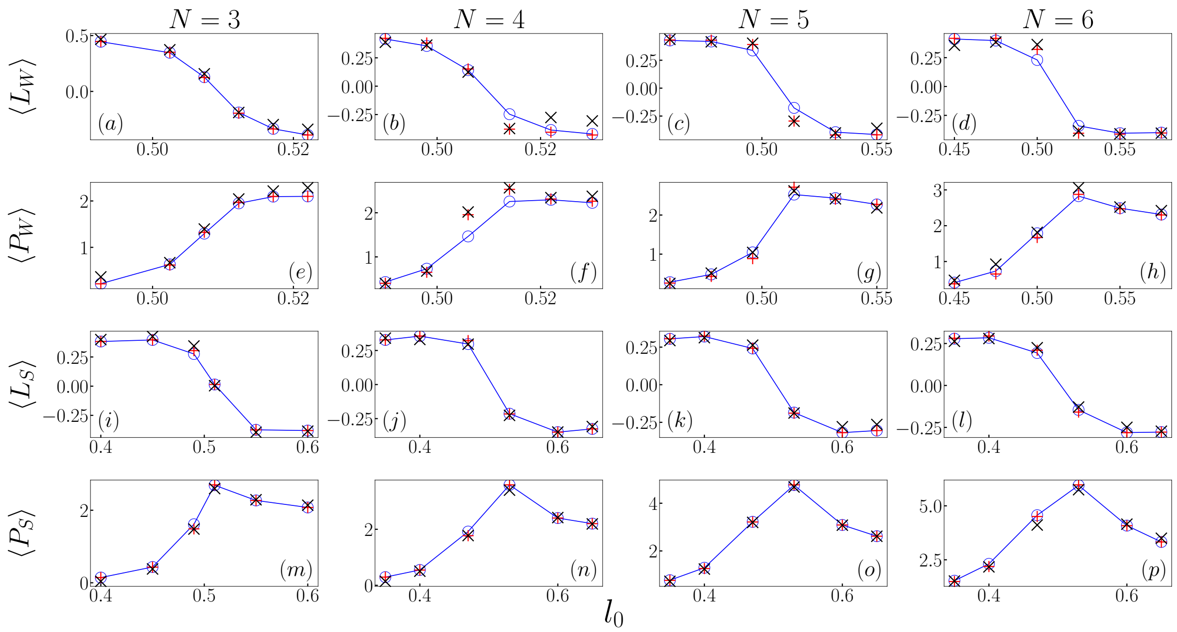

**Figure 5.3:** *The description for this figure follows Fig. 5.2, however the lattice mass here is set to* $m_{lat}/g = 0$*, so that we are below the second order phase transition and thus observe no first-order phase transition as expected. Note that the error bars are much smaller than the y-scale and thus, are not visible. The blue circles represent the exact diagonalization, red pluses the noiseless simulations and black crosses the quantum hardware results.*

the critical value. However, for some values of $l_0$, particularly near $l_0 = 1/2$ and larger $N$, the VQE does not fully converge to the exact diagonalization results (see Figs. 5.3($b - d$), ($f$)), with fidelities around 0.85 in these cases. The larger slope observed near $l_0 = 1/2$ for larger $N$ suggests that, despite choosing a small lattice mass, finite-size effects and additive mass renormalization bring the system close to the first-order transition. Consequently, at $l_0 = 1/2$, the presence of two states with nearly degenerate energy complicates VQE convergence. Nonetheless, across a broad range of parameters, our classical VQE simulations show good agreement with exact diagonalization.

For staggered fermions, we employ the initial states and qubit mappings discussed in Sec. 5.2. In this case, ansätze using $R_{XX+YY}$ gates consistently yield higher fidelities than those with SO(4) gates. When using SO(4) gates, we frequently observe that the final optimized parameters tend to zero, effectively reducing the ansatz to its non-parametric part, which prepares the $|10\rangle^{\otimes N/2}$ state. In contrast, with $R_{XX+YY}$ gates, both architectures perform comparably well, achieving fidelities above 0.99. Due to its lower CNOT-depth, we focus on the brick ansatz for the staggered discretization.

For $m_{\text{lat}}/g = 10$, the staggered fermion results qualitatively resemble those of Wilson fermions, as shown in Fig. 5.2. The characteristic discontinuities in the EFD and PN confirm the presence of a first-order quantum phase transition. Notably, for the staggered discretization, the transition occurs at larger $l_0$ values than in the Wilson case, despite matching the qubit count. Since the total volume remains fixed at $N/\sqrt{x} = 30$, the staggered discretization effectively has a smaller lattice spacing. The observed shift in the transition location might be attributed to a larger additive mass renormalization, or to larger finite size effects affecting the observables of staggered fermions. Similar to the Wilson case, increasing $N$ shifts the transition to smaller $l_0$ values, as detailed in Sec. 5.4. Once again, exact diagonalization results exhibit excellent agreement with the simulated VQE using a single ansatz layer, demonstrating that our circuit and qubit mapping capture the essential physics of the model in the large-mass regime.

For $m_{\text{lat}}/g = 0$, the increased complexity of the ground state requires two ansatz layers to maintain high fidelities. Figure 5.3 shows the results for the brick ansatz with two layers. The observables are now changing smoothly with $l_0$, indicating the absence of a first-order transition at this mass. Interestingly, in the staggered case, the VQE results match exact diagonalization nearly perfectly across the entire parameter range studied, with no noticeable deviations.

In summary, our findings for Wilson fermions suggest that the brick ansatz with SO(4) gates, combined with an appropriate initial state, is generally the most efficient choice. Moreover, the required resources for achieving high-fidelity approximations show little dependence on system size within the studied range. In the staggered case, the brick ansatz with $R_{XX+YY}$ gates consistently performs well across all parameters explored. Similar to the Wilson case, we observe no strong dependence on system size, suggesting the feasibility of scaling our approach to larger systems.

## 5.4. Lattice effects on the phase transition

Here, we derive an analytical expression for the location of the first-order phase transition in the lattice Schwinger model, focusing on the regime where $m/g \gg 1$, i.e., the limit in which the kinetic term is negligible.

We begin by mapping the electric field energy to its lattice counterpart. The electric field operator can be made dimensionless using the coupling $g$ between the fermions and gauge fields, i.e., $E \to gL_n$. The corresponding mapping from the continuum electric field energy to its lattice version is given by

$$\int_{-\infty}^{\infty} \frac{E^2}{2} dx \to a \sum_{n=0}^{N-2} \frac{g^2 L_n^2}{2}. \tag{5.10}$$

Our derivation remains independent of the specific lattice fermion formulation, making the result general and applicable to both Wilson and staggered formulations. The key insight is that at the first-order phase transition, denoted by $l_0^*$, the ground state exhibits a two-fold degeneracy.

To the left of the phase transition, where $l_0 < l_0^*$, the ground state contains no charges, and the total electric field on each link is $l_0$. Consequently, the total energy $E_{l_0<l_0^*}$ is given solely

by the electric field contribution

$$E_{l_0<l_0^*} = a(N-1)g^2\frac{l_0^2}{2}, \tag{5.11}$$

where we have used the fact that a lattice with open boundaries contains $N-1$ links.

To the right of the phase transition, where $l_0 > l_0^*$, the ground state consists of a negative charge at the left edge and a positive charge at the right edge, connected by an electric flux string that reduces the total electric field by one unit. This results in an electric field of $l_0 - 1$ on each link. The total energy is then given by the sum of the electric field energy and the mass energy contribution of $2m_\mathrm{r}$ from the two charges

$$E_{l_0>l_0^*} = a(N-1)g^2\frac{(l_0-1)^2}{2} + 2m_r. \tag{5.12}$$

In Sec. 1.1, where the continuum model was discussed, we ignored the energy $2m_\mathrm{r}$ of the Dirac sea. For the lattice case, we have to take it into account, which can be trivially seen from the fact that the first term on the right hand side of Eq. (5.14) can be ignored in the infinite volume limit. Equating Eq. (5.11) and Eq. (5.12) at $l_0 = l_0^*$ and solving for $l_0^*$ yields

$$l_0^* = 2\frac{m_\mathrm{r}}{g}\frac{\sqrt{x}}{N-1} + \frac{1}{2}. \tag{5.13}$$

In the limit of large $N$, this expression simplifies to

$$l_0^* \approx 2\frac{m_\mathrm{r}}{g}\frac{\sqrt{x}}{N} + \frac{1}{2}, \tag{5.14}$$

where $\frac{\sqrt{x}}{N}$ represents the dimensionless inverse volume. Taking the infinite-volume limit, we recover the continuum result $l_0^* = 1/2$, as expected.

Substituting for the volume as $N/\sqrt{x} = 30$ and expressing the renormalized mass in terms of the lattice mass with a MS, we obtain

$$l_0^* = 2\left(\frac{m_\mathrm{lat}}{g} + \mathrm{MS}\right)\frac{1}{30-ag} + \frac{1}{2}. \tag{5.15}$$

Since the MS decreases as $ag$ decreases [60, 267], which is also shown in Fig. 4.4, and the factor $1/(30-ag)$ also decreases as $ag \to 0$, the first term in Eq. (5.15) decreases, bringing the transition point closer to the continuum limit. Thus, we observe that on finite lattices, $l_0^*$ is generally shifted to values larger than 1/2, approaching the continuum prediction as the lattice spacing decreases.

To further illustrate Eq. (5.13) using staggered fermions, we present in Fig. 5.4 from [61] the dependence of the phase transition point $l_0^*$ on $1/N$ for $x = 7, 9$, ensuring we remain above the dimensionless physical volume threshold of 30. Without loss of generality, we consider a small renormalized mass $m_\mathrm{r}/g = 0.5$, near the second-order phase transition, where $l_0^*$ is expected to be close to 0.5 according to Eq. (5.13), and then double this value to $m_\mathrm{r}/g = 1$.

To determine $l_0^*$ for each combination of $N, x$, and $m_\mathrm{r}/g$, we employ the bisection method [269] with the EFD observable, first computing the ground state as a MPS. The variational algorithm terminates when the relative energy change is below $10^{-11}$, with the bond dimension set sufficiently high to ensure that the cutoff on singular values, set to $10^{-15}$, does not saturate the bond dimension. As a result, errors due to neglected singular values below $10^{-15}$ are negligible.

Any value of $l_0$ yielding a positive EFD is considered to be below $l_0^*$, and vice versa. The algorithm terminates once the difference between the left and right $l_0$ values falls below $10^{-9}$. To maintain a fixed renormalized mass, we compute the MS iteratively using again the bisection method with the EFD observable, initializing the search with left and right values of $m_\mathrm{lat}/g$ that bracket the zero-crossing of the EFD. The algorithm terminates when the uncertainty in $m_\mathrm{lat}^*/g$, representing minus the MS, is below $10^{-9}$.

From Fig. 5.4, we observe that as $m_\mathrm{r}/g$ decreases, $l_0^*$ approaches 0.5. Furthermore, increasing $x$ raises $l_0^*$ while steepening its gradient, whereas increasing $N$ reduces $l_0^*$, all in agreement with Eq. (5.13).

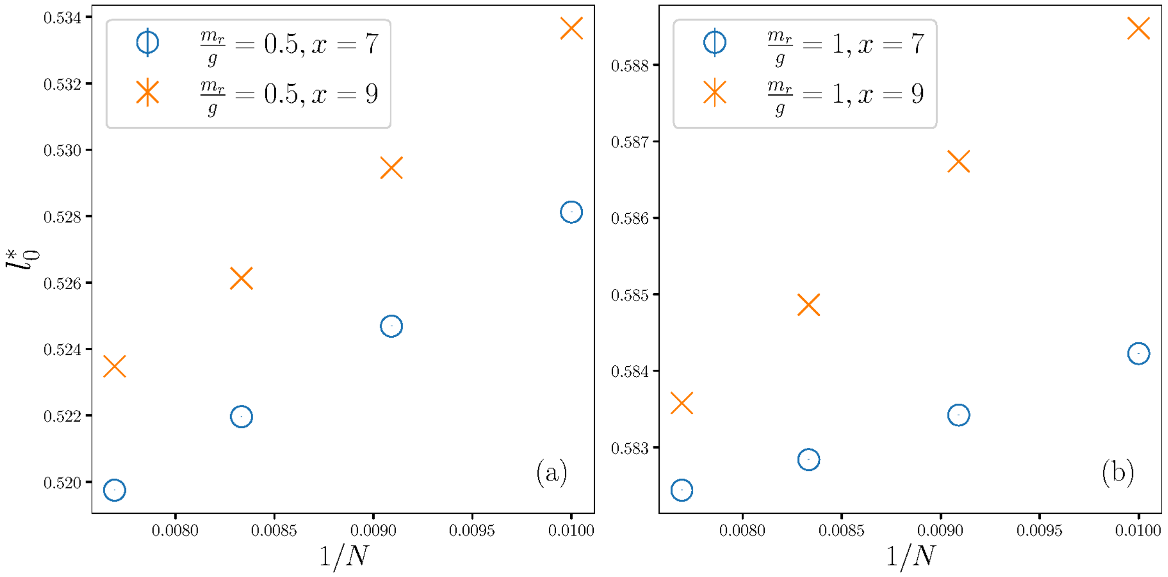

**Figure 5.4:** *The phase transition point $l_0^*$ as a function of $1/N$ for $x = 7, 9$ and $m_r/g = 0.5$ (a), 1 (b). The error bars, estimated via the bisection method described in the main text, are smaller than the scale of the y-axis and are therefore not visible.*

## 5.5. Inference runs on quantum hardware

In Sec. 5.3 it was demonstrated that our VQE ansatz efficiently captures the relevant ground states with a small number of layers. To further establish the feasibility of this approach on current and near-term quantum hardware, we perform inference runs on quantum devices. Specifically, we prepare the ansatz circuit using the optimized parameters obtained at the end of the classical VQE simulation and execute it on a quantum device, measuring both the EFD and the PN. For these inference runs, we utilize IBM's quantum devices *ibm_hanoi*, *ibm_cusco*, and *ibm_nazca*, performing $10^4$ measurements in the computational basis. The results for both fermion discretizations, after applying the error mitigation techniques discussed in Sec. 5.6, are shown in Fig. 5.2 and Fig. 5.3, alongside the data from the simulated ideal VQE and exact diagonalization.

Overall, the results obtained from the quantum hardware exhibit good agreement with the noise-free VQE simulations, apart from a few discrepancie, as for example the third point in Fig. 5.3($f$) that has a 3.1% relative distance between the result from the noise-free VQE and the hardware run. Several factors may contribute to these deviations. Notably, we observed that measurements taken immediately after hardware calibration were generally closer to the simulated results, whereas those performed several hours after calibration displayed larger deviations. Additionally, the case $m_{\mathrm{lat}}/g = 0$ shows a few data points that deviate more significantly from the corresponding noise-free results compared to the higher mass case $m_{\mathrm{lat}}/g = 10$. This discrepancy can be attributed to the fact that the circuits for $m_{\mathrm{lat}}/g = 0$ were one layer deeper, increasing their susceptibility to noise.

Having demonstrated that our ansatz can be reliably executed on current and near-term quantum hardware for system sizes of 6–12 qubits, in the next section we look into more detail the error mitigation techniques utilized.

## 5.6. Error mitigation

To evaluate the performance of the error mitigation procedure, we present in Fig. 5.5 from [61] histograms of the absolute errors for both the unmitigated and mitigated results of the PN and the EFD. The absolute error, plotted on the $x$-axis, represents the absolute difference between the values obtained from the simulated VQE and those measured on the quantum device, with or without mitigation. In the case of the EFD in the Wilson formulation and the PN in the staggered formulation, Figs. 5.5($a, d$) reveal a clear improvement. Specifically, the mitigated values (blue bars) are more concentrated around smaller errors and have a higher probability of matching the expected result than the unmitigated values (red translucent bars).

For the EFD in the staggered formulation and the PN in the Wilson discretization, we observe a slightly different trend. Figures 5.5($b$) and 5.5($c$) indicate that the probability of measuring the exact result has decreased compared to the unmitigated case. However, the overall distribution of errors after mitigation exhibits a reduced width and is more concentrated at smaller values, indicating an improvement in precision. This behavior can be explained by the fact that ZNE does not always guarantee an improvement and, in some cases, can slightly worsen the final result. Detailed examples of ZNE extrapolations are provided in Fig. 5.6 from [61]. Despite these variations, we generally observe a beneficial effect of error mitigation, as the expected error is reduced across all cases.

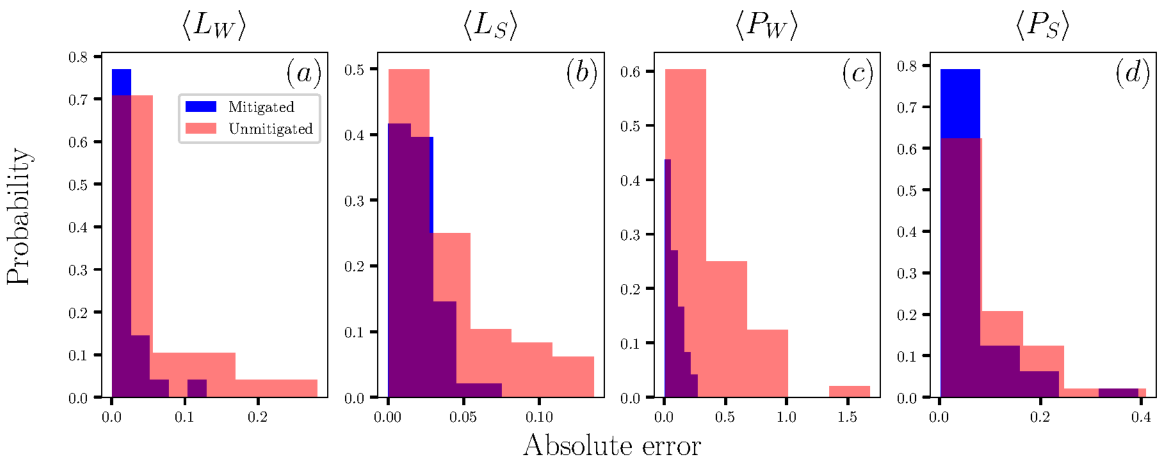

**Figure 5.5:** *Histograms for the absolute errors of the mitigated and unmitigated data for the electric field density (EFD) for the Wilson* $(a)$ *and the staggered discretization* $(b)$ *as well as the particle number (PN) for the Wilson fermions* $(c)$ *and the staggered formulation* $(d)$*. Blue bars represent the absolute error between the hardware data after zero noise extrapolation (ZNE) and the simulated VQE, while red bars represent the absolute error between unmitigated hardware data and the simulated VQE. Each subplot includes all* $N, m_{lat}/g, l_0$*.*

To conclude this section we turn to Fig. 5.6, and provide the technical details of the ZNE employed in our inference runs. Our implementation utilizes global folding with noise factors of 1, 3, and 5, collecting 10,000 shots for each circuit. The noise factors for global folding were explained in Sec. 3.2.

To obtain the final zero-noise extrapolated expectation value, we first compute preliminary extrapolated values using three distinct fitting approaches. These consist of a linear fit to noise factors 1, 3, and 5, a linear fit to noise factors 1 and 3, and a second-order polynomial fit to noise factors 1, 3, and 5. The final extrapolated value is then computed as a weighted average of these preliminary values, where the weights are determined by the variance of each fit. This variance arises from the fitting procedure itself, which is performed on data points that inherently possess a variance. Each data point in a fit, corresponding to a specific noise factor, represents the average over 10 twirls used in the Pauli twirling error mitigation technique described in Sec. 3.2. The associated error of each point within a fit is derived from this averaging process. Specifically, the error for each of the 10 twirls before averaging is estimated as the square root of the variance of the measurement divided by the number of shots.

In Fig. 5.6, we illustrate specific examples of ZNE fits for selected parameters. The figure includes representative cases where ZNE successfully improved the expectation value of the observable, as well as cases where no significant improvement was achieved.

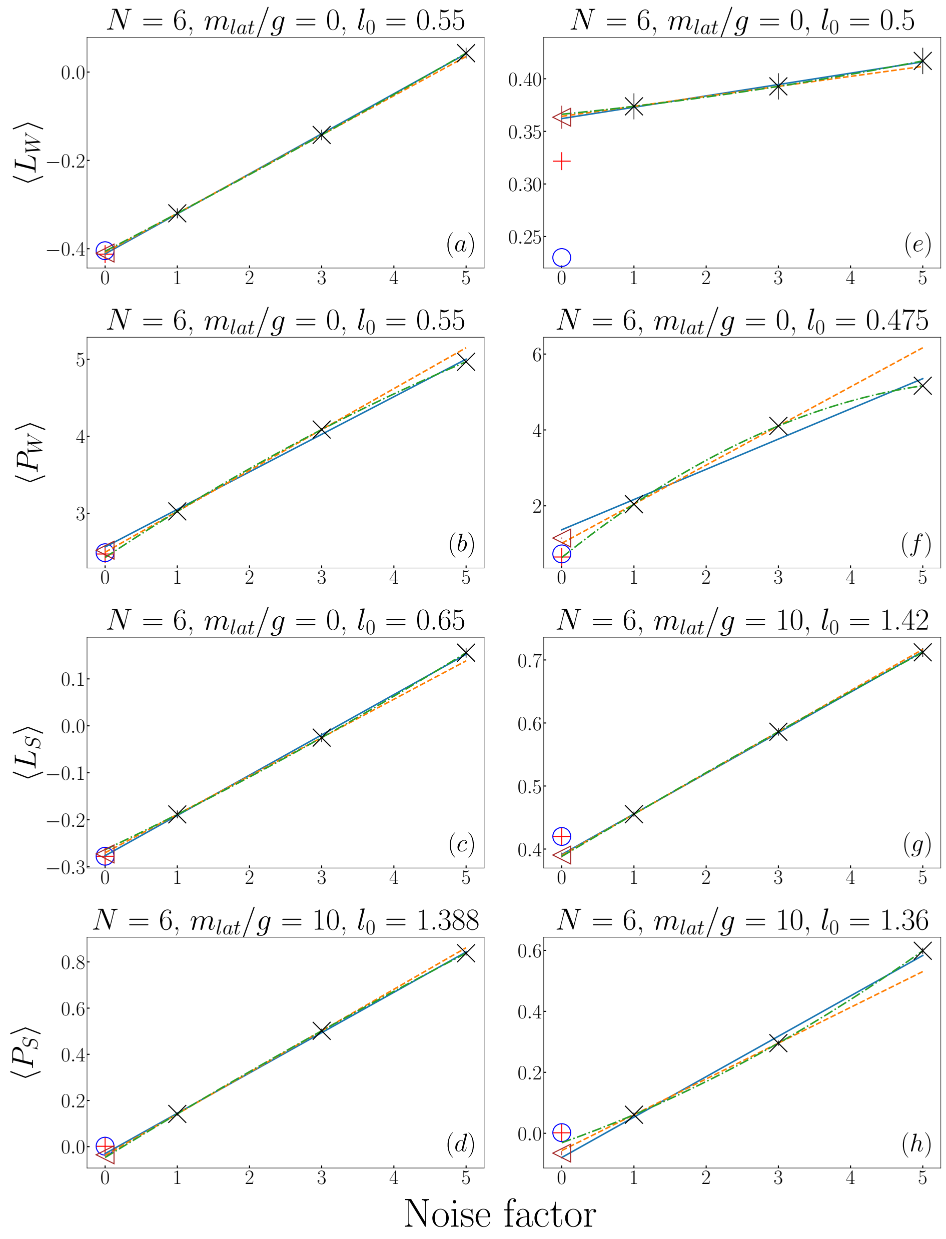

**Figure 5.6:** *Electric field density (EFD) $\langle L_{W,S} \rangle$ and particle number (PN) $\langle P_{W,S} \rangle$ against noise factor for zero noise extrapolation (ZNE) on the data (black crosses) obtained from quantum hardware for different parameters specified in the titles of each subplot with Wilson and staggered fermions. The red pluses are noiseless values of the observables and the blue circles are the exact diagonalization results. For the fits we fit a first-order polynomial to either all points (blue continuous line) or to points with noise factor 1, 3 (dashed orange line). We also fit a second order polynomial to all points (green dotted dashed line). The brown triangle is the weighted average of the extrapolated points of these 3 fits. The plots on the left $(a - d)$ are showing examples where the ZNE helped take the expectation values measured closer to the noiseless result, while on the right $(e - h)$ we show occasions where the ZNE might not be able to improve the result. However, overall the results of the main text indicate that ZNE can significantly improve the results. The calculation of the error bars is described within this Appendix and where they are not visible, they are smaller than the markers and y-scale.*

## 5.7. Continuum extrapolation with MPS

To investigate the system sizes required for a reliable extrapolation to the continuum limit and to compare the performance of both fermion discretizations in approaching this limit, we employ MPS simulations as discussed in Sec. 2.5. We consider a fixed lattice volume of $N/\sqrt{x} = 30$ and restrict the number of physical sites to $N \in [70, 80, 90, 100]$. This setup allows us to study the fixed-volume continuum limit, $ag \to 0$, using computational resources that should be accessible on current and near-term quantum hardware.

To follow a trajectory of constant renormalized mass towards the continuum limit, we determine the MS for each value of $N$ and $l_0$ based on the approach outlined in Ch. 4. We focus on a small renormalized mass, $m_r/g = 0.01$, as large masses yield ground states that are closer to product states, whereas small masses present a more challenging regime. Specifically, we analyze the EFD, since for this observable, our continuum extrapolations can be directly compared to the predictions from mass perturbation theory in Eq. (1.7).

After bond dimension extrapolations of the EFD, exemplified in Ch. 4 by Fig. 4.2, we extrapolate this observable to $ag = 0$ as shown in Fig. 5.7. For the Wilson case, we take the extrapolated value of the linear fit and assign an approximated error to it which is taken to be the difference between that value and the extrapolated value of a quadratic fit. For the staggered case, it was observed that second-order polynomial fits were more suitable and that they converge faster to the continuum. Therefore, we keep the extrapolated value of the quadratic fit and again approximate the error as in the Wilson case. To avoid boundary effects, the EFD for Wilson fermions is measured using the middle link, and for staggered fermions, the four middle links are measured to also reduce the staggering effect.

Figure 5.8 presents the continuum extrapolated results for the EFD obtained from each discretization, alongside the mass perturbation theory prediction. To compare the performance of the staggered and Wilson formulations, we consider two possible choices. One choice is fixing the same value of $x = 1/(ag)^2$ for both discretizations, which results in the staggered formulation requiring half the number of qubits compared to Wilson. The other choice is fixing the number of qubits for both discretizations, leading to twice the number of physical sites in the staggered case and, consequently, a finer lattice spacing for the same lattice volume.

For the staggered formulation, we further compare results obtained using the theoretically predicted MS from Eq. (4.8), for which we give the notation $\mathrm{MS}_t$, to those obtained by measuring the MS following the EFD method of Ch. 4. For the results that use the MS from the EFD method we give the notation $\mathrm{MS}_L$. This yields four possible combinations of the above considerations, all of which are displayed in Fig. 5.8.

In general, the most accurate results for both Wilson and staggered fermions are obtained when using $\mathrm{MS}_L$ and the same value of $x$ as Wilson. When the staggered formulation retains the same number of qubits as Wilson but uses $\mathrm{MS}_L$, the accuracy deteriorates slightly, primarily because computational resources, such as bond dimension $D$, remain fixed as in the same-$x$ scenario, even though the staggered formulation involves a larger $N$. Additionally,

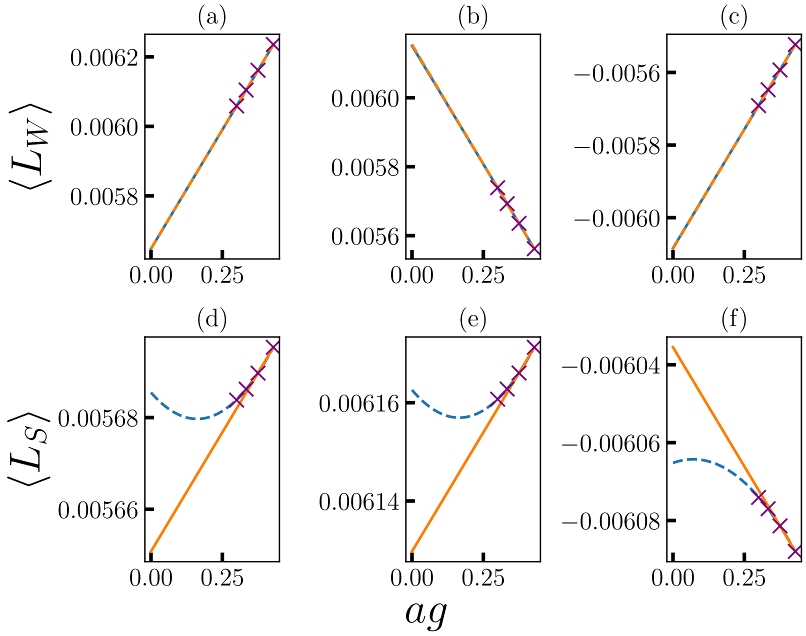

**Figure 5.7:** *Electric field density (EFD) $\langle L_{W,S} \rangle$ against ag to extrapolate to the continuum limit with fixed volume $N/\sqrt{x} = 30$, fixed $m_r/g = 0.01$, using $N = 70, 80, 90, 100$. The continuous orange line is a linear fit and the dashed blue line is a second order polynomial fit. $(a - c)$ is showing Wilson fermions for $l_0 = 0.1, 0.4, 0.6$ respectively and $(d - f)$ the same for staggered fermions with the same x as Wilson fermions and the EFD method for the mass shift (MS) [60]. The error bars emanate from the variational algorithm to compute the relevant ground states and the extrapolation in bond dimension. They are much smaller than the markers and thus, are not visible.*

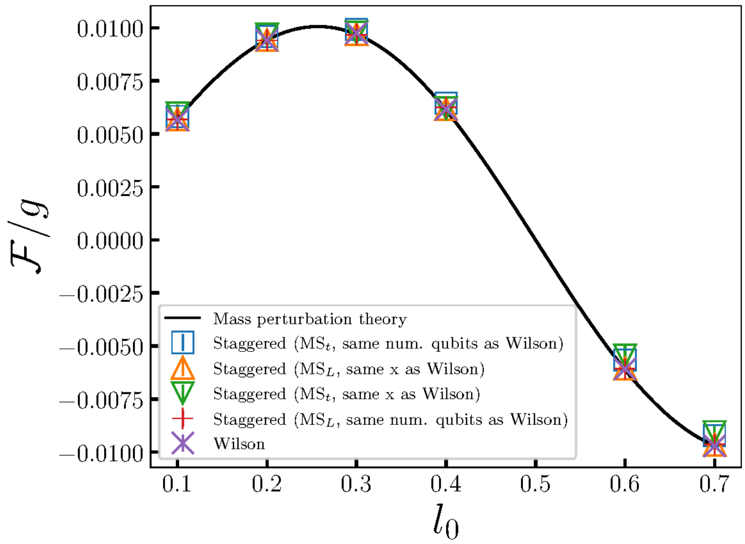

**Figure 5.8:** *Electric field density (EFD) $\mathcal{F}/g$ against $l_0$ for Wilson fermions and staggered fermions at $m_r/g = 0.01$. The following mean squared error (MSE) values are the MSE of each of the data as compared to the continuum mass perturbation theory prediction for the EFD $\mathcal{F}/g$ given in Eq. (1.7). For staggered fermions with $MS_t$ and same $x$ (number of qubits as Wilson), the MSE is $1.041 \times 10^{-6}$ ($6.16 \times 10^{-7}$), and respectively for $MS_L$ $6.143 \times 10^{-9}$ ($2.617 \times 10^{-8}$). For Wilson fermions the MSE is $7.926 \times 10^{-9}$. The error bars emanate from the errors in the variational algorithm to compute the relevant ground states, the extrapolation in bond dimension and in lattice spacing.*

staggered fermions employing $\mathrm{MS}_t$ fail to achieve the best performance, as $\mathrm{MS}_t$ does not account for the dependence of the MS on $l_0$. This discrepancy is particularly evident at larger values of $l_0$, where deviations from perturbation theory become more pronounced in Fig. 5.8. In Table 5.1, we provide a quantitative analysis of these deviations by presenting the absolute difference between the points in Fig. 5.8 and the mass perturbation theory predictions. Similar $l_0$ dependence effects in the massless Schwinger model with staggered fermions were previously also reported in Fig. 7 of Ref. [273].

Overall, we conclude that even with these modest computational resources, the extracted data closely aligns with continuum theory, both qualitatively and quantitatively. However,

| $l_0$ | 0.1 | 0.2 | 0.3 | 0.4 | 0.6 | 0.7 |
|---|---|---|---|---|---|---|
| Wilson | 4.45001467e-05 | 1.00338853e-05 | 5.58001106e-05 | 3.04735487e-05 | 3.64867975e-05 | 2.17138610e-05 |
| Staggered ($\mathrm{MS}_t$, same num. qubits as Wilson)} | 0.00012783 | 0.00016672 | 0.00022494 | 0.0003207 | 0.00045197 | 0.00046271 |
| Staggered ($\mathrm{MS}_L$, same x as Wilson) | 6.97181950e-06 | 4.86364083e-06 | 1.14145910e-05 | 4.21571198e-05 | 5.52293937e-05 | 3.33572489e-05 |
| Staggered ($\mathrm{MS}_t$, same x as Wilson) | 2.91080596e-04 | 2.63562909e-04 | 8.61951831e-05 | 1.03764598e-04 | 6.79235186e-04 | 6.37947680e-04 |
| Staggered ($\mathrm{MS}_L$, same num. qubits as Wilson) | 2.05654489e-05 | 1.75062880e-05 | 1.54209990e-05 | 1.40152738e-04 | 5.40892433e-05 | 5.13089222e-05 |

**Table 5.1:** *This table corresponds to the absolute error with respect to the results from mass perturbation theory for the data presented in the main text. For staggered fermions that use the theoretically predicted MS, $MS_t$, the error tends to grow with $l_0$ due to the fact that the $MS_t$ does not account for an $l_0$ dependence.*

neglecting the MS leads to significantly larger error bars, as shown in Fig. 5.9. Thus, when approaching this problem with digital quantum computing, careful consideration of the MS will be essential to obtain reliable continuum limit results, even with relatively small system sizes up to $100 - 200$ qubits.

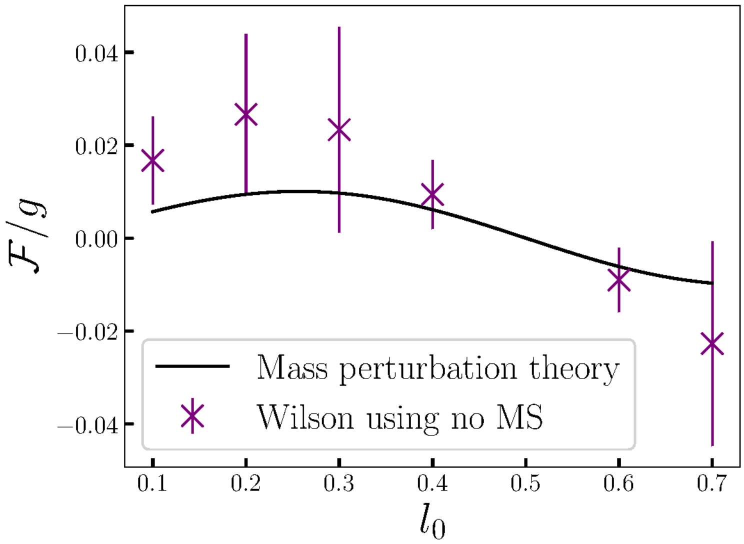

**Figure 5.9:** *Electric field density (EFD)* $\mathcal{F}/g$ *against* $l_0$ *for Wilson fermions using no mass shift (MS) at* $m_r/g = m_{lat}/g = 0.01$. *The MSE is calculated as in the main text and found here to be* $7.939 \cdot 10^{-4}$. *The error bars emanate from the errors in the variational algorithm to compute the relevant ground states, the extrapolation in bond dimension and in lattice spacing.*

# 6 | Open quantum systems

Open quantum system (OQS) apply to the cases in which a quantum system interacts with an external environment, which affects its evolution through energy, particle, and information exchanges [113–117]. As every experiment of quantum phenomena necessarily involves open systems to some degree, and since quantum field theories (QFTs) [274] describe nature effectively, it becomes essential to develop and investigate open QFTs.

A well-known example of an open QFT arises in heavy-ion collisions at the large hadron collider (LHC) and the relativistic heavy ion collider (RHIC), where a dense, hot medium known as the quark gluon plasma (QGP) forms. Within this plasma, bound states of heavy quarks, called quarkonia (e.g., bottomonium and charmonium), propagate [25, 118–120]. Here, the quarkonium constitutes the system, and the QGP serves as the environment [275]. The color-charge screening in the QGP reduces the quarkonium binding strength [9], leading to a suppression in bound quarkonia yields [276]. This effect makes quarkonia excellent probes for studying the properties of QGP [9, 277–279]. Changes in the mass of the quarkonium influence its size, which in turn affects its screening, dissociation, and thermalization properties. Prior research has explored these phenomena using master equation techniques, which allow for a representation of the quantum state while limiting the Hilbert space dimension [280, 281].

To investigate meson thermalization in a hot medium, we use the Schwinger model as a simplified toy model of quantum chromodynamics (QCD), due to its similar features like confinement and charge screening [63, 282]. We implement the model within a tensor network (TN) framework [34, 131, 220, 283, 284], which has been successfully employed in both equilibrium and dynamical studies of the Schwinger model [40–53, 60]. This helps us overcome the traditional challenges posed by the Monte Carlo sign problem [25] and the limitations of perturbative methods at strong coupling.

For the numerical simulations, we follow the approach outlined in Sec. 1.5 and Sec. 2.6, including suppressing the lattice spacing $a$ for dimensionless parameters, and using $m_{\text{lat}}$ as $m$ for simplicity. To the best of our knowledge, this represents the first application of TN techniques to lattice gauge theory (LGT) within the OQS framework. In our study, we simulate dynamics resembling quarkonia in the QGP by investigating the behavior of a string and the Schwinger boson in a hot environment. We use the electric field as an observable to monitor thermalization and explore how parameters such as temperature $T$, mass $m$, background electric field $l_0$, and environmental dissipation strength $D$ affect the dynamics.

Additionally, we assess thermalization through mutual information, drawing from quantum information theory [39], which offers insights that correspond with experimental and numerical investigations of quarkonia in QGP.

While progress has been made, studies of the Schwinger model as an OQS remain limited. In [70], the authors simulate the time evolution of the Dirac vacuum for $N = 2$ using an IBM quantum device, and extend the simulations to $N = 8$ via a classical simulator to examine finite-size effects. The phenomenon of string breaking in open versus closed systems is investigated in [126], showing significant differences in the dynamics between isolated and dissipative systems. Furthermore, [127] introduces neural density operators that leverage neural networks to represent the density matrix, allowing for the simulation of string dynamics up to $N = 32$ with multiple interacting strings.

Nonetheless, several important questions remain unanswered, such as the impact of truncating the gauge degrees of freedom, the role of external fields in string dynamics, and the behavior of the Schwinger boson, which is the theory's stable particle. Previous studies have often truncated the gauge degrees of freedom Hilbert space to a limited number of states per link, which may alter the physics observed as compared to the non-truncated case. Moreover, the effect of an external background electric field on string behavior in OQS has not yet been explored.

Our work seeks to address these questions by studying an open lattice Schwinger model without truncating the gauge degrees of freedom, as outlined in Eq. (1.36). In addition, we examine the Schwinger boson, the stable meson-like particle of the theory [56, 285], and introduce an external background electric field that influences string dynamics in OQS. Including this external field could have practical relevance for future experimental studies of quarkonia in QGP. Finally, by extending our simulations to $N = 100$, we demonstrate the feasibility of applying our method to larger system sizes, an essential step in connecting numerical simulations to experimental results and the continuum limit of lattice field theory.

The chapter is organized as follows. In Sec. 6.1, we introduce the initial state representing a meson-like string composed of a positive-negative charge pair and simulate its time evolution in a hot medium. Section 6.1.1 explores how thermalization depends on various parameters. In Sec. 6.1.2, we show results that highlight the relationship between thermalization time and mutual information. Section 6.1.3 investigates how the thermalization time varies with the temperature of the environment, and Sec. 6.1.4 demonstrates how our simulations scale to larger system sizes. Lastly, in Sec. 6.2, we present results on the time evolution of the Schwinger boson.

The chapter's findings have already been published in [62] as

Angelides, T. et al. “Meson thermalization with a hot medium in the open Schwinger model”. J. High Energ. Phys. 2025, 195 (2025) doi: 10.1007/JHEP04(2025)195.

## 6.1. String thermalization

In this section, we present the results of the time evolution of the string state, initially prepared from the Dirac vacuum, which represents the absence of charge. The Dirac vacuum is an eigenstate of the Hamiltonian in Eq. (1.36) in the infinite mass limit and can be represented as the product state $|01..01\rangle$. To create a string of electric flux, we flip the spins at the positions $N/2-2$ and $N/2+1$, where the index $n$ starts from 0. This spin flip introduces a positive charge at the site $N/2-2$ and a negative charge at $N/2+1$, as can be checked from Eq. (1.35). The state is then evolved under the influence of the hot environment, and we track the relevant observables.

In this chapter, we fix $D(n-k) = D\delta_{n,k}$ [70] for the time evolution described by the Lindblad master equation in Eq. (2.29), where $D$ denotes the strength of the environment dissipator. Additionally, for the parameters detailed in Sec. 2.6, we set $x = 1$, $\epsilon = 10^{-11}$, $\epsilon_1 = \epsilon_2 = 10^{-9}$, $\kappa = 2$, and $\tau = 0.01$, except in Sec. 6.1.4, where we use $x = 4$ and $\tau = 0.001$ due to the larger $N$ values considered.

To isolate the dynamics of the string, we perform the time evolution for the Dirac vacuum state and subtract the corresponding observables from those of the string state. These subtracted observables provide a clearer picture of the string dynamics. An example of this is the electric field as a function of the link number, which is represented by the expectation value of the operator in Eq. (1.24), $F(n) \equiv \langle L_n \rangle$. The subtracted electric field (SEF) is denoted as $\Delta F(n)$.

Figure 6.1$(a)$ shows an example of the SEF as a function of time for $N = 12$. Initially, the electric flux is confined, but it gradually spreads out over time and eventually reaches a thermal equilibrium. The middle link at $n = 5$ exhibits the longest thermalization time, which we will use to define the thermalization time. The corresponding subtracted charge, $\Delta Q(n)$, is shown in Fig. 6.1$(b)$. The initial unit charges are clearly observed at the sites where the spins were flipped, and as time progresses, these charges spread and become less localized.

### 6.1.1. Dependence on $D$, $l_0$ and $m$

Given the definitions of the previous section, we start to investigate in this subsection the thermalization time $\mathcal{T}$ of the string as we vary the parameters $m$, $l_0$, and $D$. Regardless of the initial configuration, whether it is the Dirac vacuum or a state with an electric flux string, both states eventually converge to the same steady state determined by the Lindblad operator, which is independent of the initial condition [70, 126]. Therefore, thermalization is considered complete once the SEF reaches zero. Our empirical data consistently show that the SEF monotonically decreases to zero at late times for all links, and that the middle link is always the last to reach thermal equilibrium. To quantify thermalization time, we define $\mathcal{T}$ as the time it takes for the SEF at the middle link to drop to 30% of its initial value. The choice of the 30% threshold is for practical reasons, as smaller fractions would require significantly longer simulations. However, since thermalization is monotonic, this choice does not affect

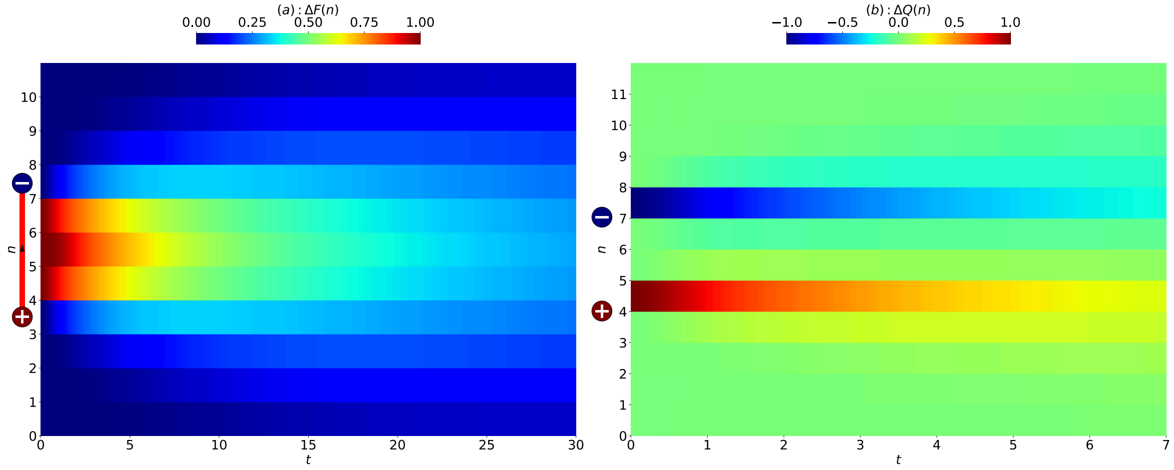

**Figure 6.1:** *Subtracted electric field (SEF) $\Delta F(n)$ per link $n$ as a function of time $t$. The red line on the y-axis represents the initial electric field flux generated by the pair of positive/negative charges shown as plus/minus on the string's endpoints. (b): Subtracted charge $\Delta Q(n)$ per site $n$ as a function of time $t$. In (b) we focus on the early time dynamics and show how the charges forming the initial string spread out. The parameters used are $N = 12$, $x = 1$, $m = 0.5$, $l_0 = 0$, $D = 2$, $T = 10$.*

the overall conclusions. While this does not represent the full thermalization time required to reach equilibrium, it offers a useful comparative measure for different parameter sets. To illustrate the monotonic decrease of SEF, we present a plot in Fig. 6.2 showing the SEF over time for a representative set of parameters, highlighting that this behavior is consistent across all parameter sets.

For this section, we use $N = 12$ and $T = 10$. Lower values of $D$ reduce kinetic dissipation, allowing particles to reach the boundaries within the thermalization time [126]. To minimize boundary effects, we restrict $D$ to the range $2 \leq D \leq 5$. Similarly, the background electric field is constrained to $0 \leq l_0 \leq 0.5$ to mitigate boundary interactions and Bragg reflections [286]. To ensure that the system is in the quantum Brownian motion (QBM) regime, the condition $T \gg H_S$ is verified numerically using ITensors' density matrix renormalization group (DMRG) to calculate the ground and first excited states of $H_S$ [206]. Specifically, for $N$ between 12 and 100, masses between 0.1 and 1.0, and $l_0$ between 0 and 0.5, the energy gaps are generally on the order of 1, which is an order of magnitude smaller than the chosen $T = 10$.

Thermalization times $\mathcal{T}$ as functions of $D \in [2, 5]$ and $l_0 \in [0, 0.5]$ are shown in Fig. 6.3 for masses $m = 0.1, 0.5, 0.75, 1$. Additionally, Fig. 6.4 illustrates how $\mathcal{T}$ depends on each individual parameter.

From Fig. 6.3, it is evident that thermalization time increases with the dissipator strength $D$ for all masses and $l_0$ values. In Fig. 6.4($a$), the relationship between $\mathcal{T}$ and $D$ is nearly linear for smaller $m$, but for larger $m$, the dependence weakens at lower $D$ values, with deviations becoming more apparent as $l_0$ increases. A higher $D$ results in stronger kinetic dissipation [126], acting as a drag force that slows the motion of charges, thus extending the thermalization time. This behavior is confirmed numerically in Fig. 6.5, where the subtracted kinetic energy (SKE) $\Delta K$ is plotted over time.

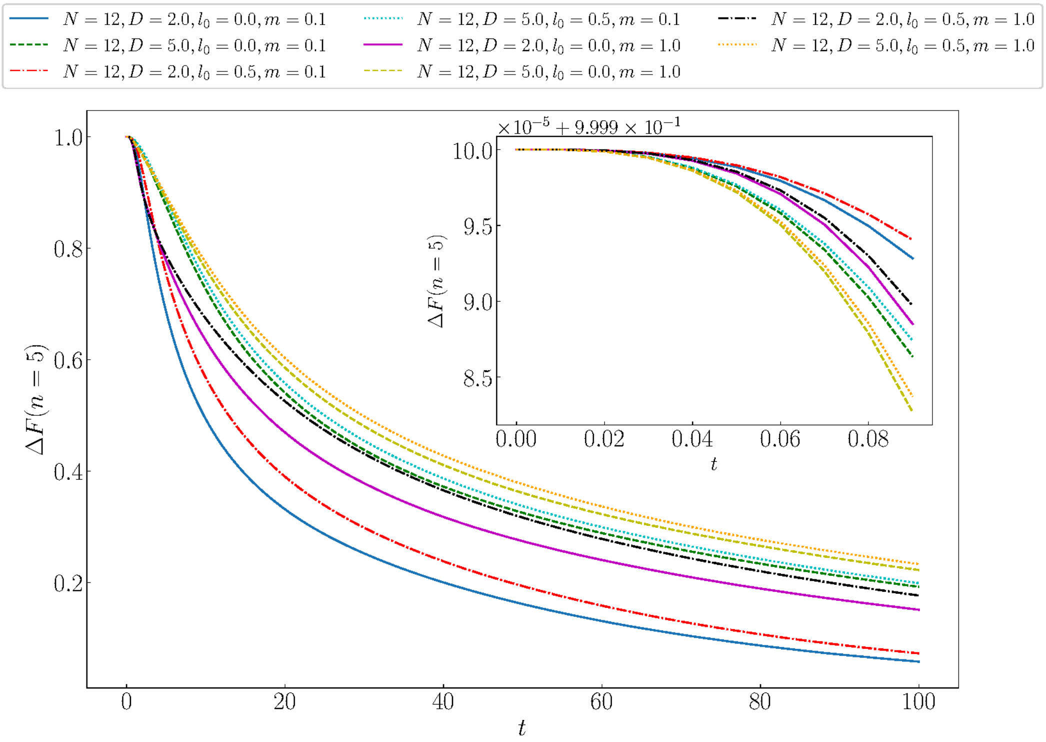

**Figure 6.2:** *Subtracted electric field (SEF) $\Delta F(n)$ of the middle link $n = 5$ as a function of time $t$. The inset zooms in on the early-time dynamics, demonstrating the monotonic decrease of SEF from its initial value to zero, indicating thermalization towards the steady state. The time resolution is fine enough to render the data quasi-continuous, with points connected by lines. This monotonic trend in SEF is key to defining the thermalization time $\mathcal{T}$.*

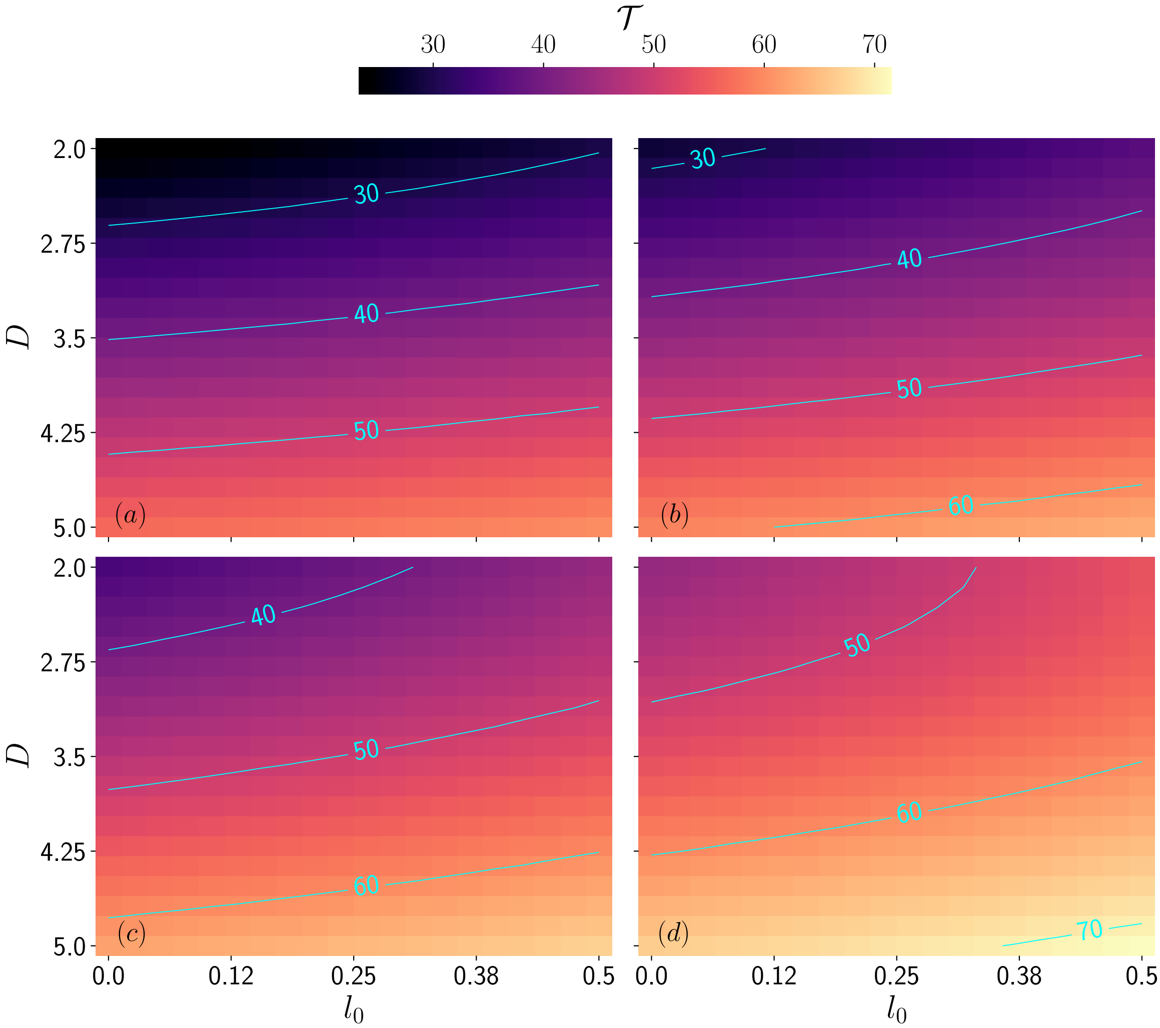

**Figure 6.3:** *Thermalization time $\mathcal{T}$ as a function of dissipator strength $D$ and background electric field $l_0$. The parameters are $N = 12$, $x = 1$, $T = 10$, (a): $m = 0.1$, (b): $m = 0.5$, (c): $m = 0.75$, (d): $m = 1$. Each axis contains 20 equidistant points with $D \in [2, 5]$, $l_0 \in [0.0, 0.5]$. All other parameters are as given in Sec. 6.1. Cyan contour lines represent levels of thermalization time $\mathcal{T}$. Increasing $D$, $l_0$, or $m$ results in a higher $\mathcal{T}$.*

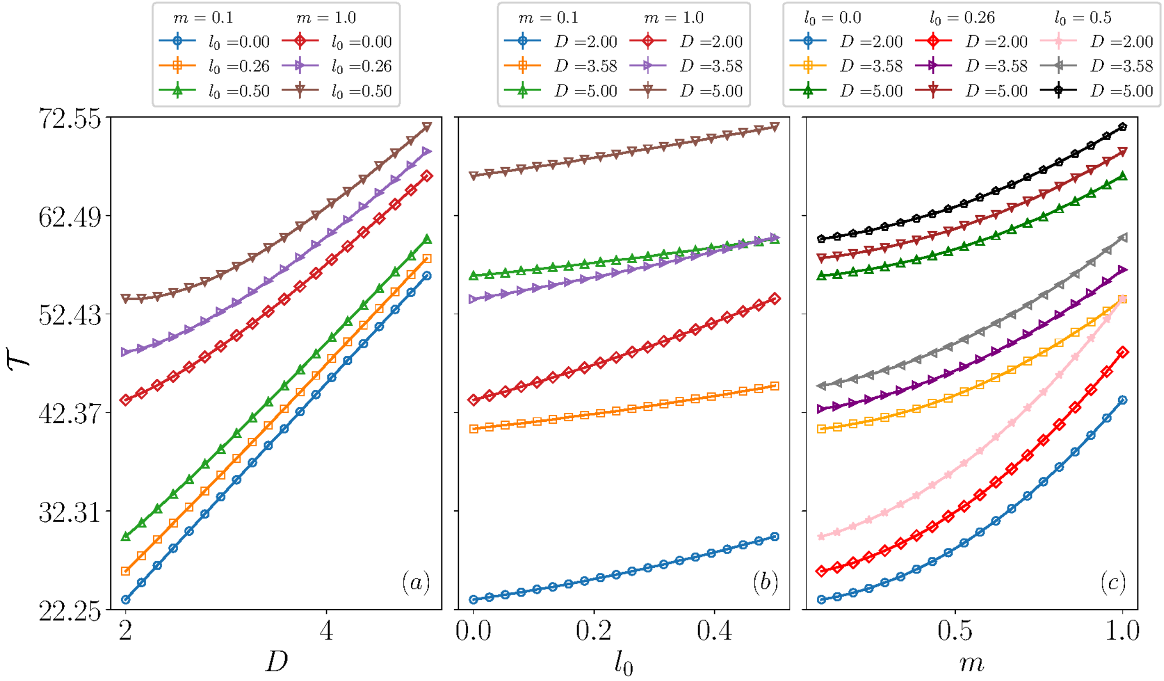

**Figure 6.4:** *(a): Thermalization time $\mathcal{T}$ vs dissipator strength $D$, (b): applied background electric field $l_0$, and (c): mass $m$. The error bars, which are not visible due to the large y-scale, are estimated to be 0.1, as inferred from the data in table 6.1 and discussed in Sec. 6.1.4. The lines are provided as visual aids.*

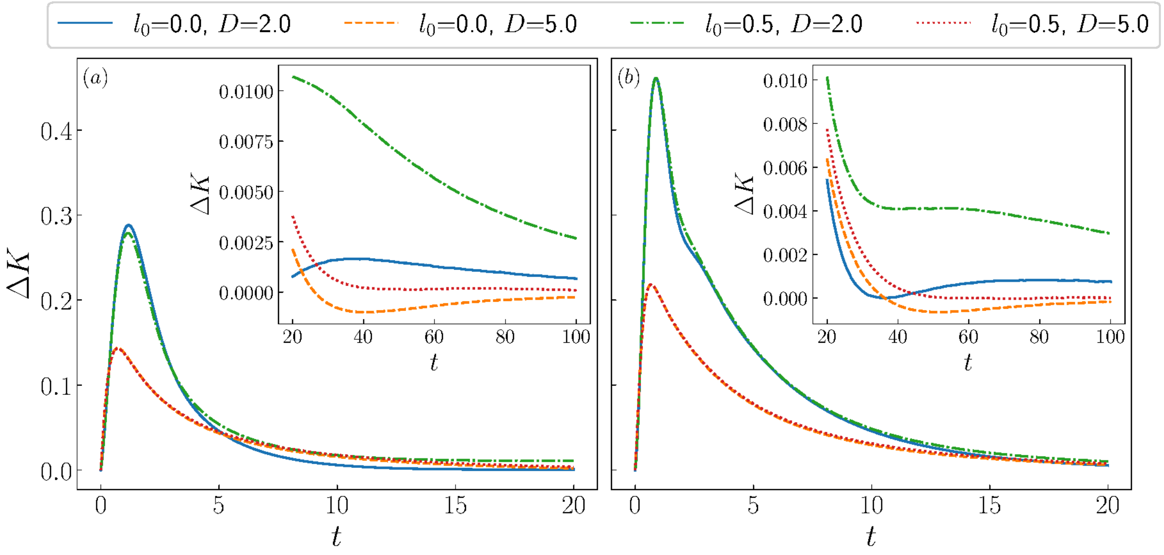

**Figure 6.5:** *(a): Subtracted kinetic energy (SKE) $\Delta K$ vs time for $m = 0.1$ and (b): $m = 1.0$ at $N = 12$. The time resolution is fine enough that the data appears quasi-continuous, with points connected by lines. Higher dissipator strength $D$ leads to a lower SKE peak. Insets display a later stage of the time evolution, highlighting the approach to thermalization.*

Additionally, Fig. 6.4($b$) shows that $\mathcal{T}$ increases as $l_0$ grows, with a trend slightly faster than linear. The applied background field creates an electrostatic force that draws the initial charge pair closer, which slows the outward expansion of the string.

Finally, both Fig. 6.3 and Fig. 6.4($c$) demonstrate that increasing $m$ results in longer thermalization times. The dependence of $\mathcal{T}$ on $m$ is faster than linear in the explored parameter range. Moreover, at lower $D$, the thermalization time is more sensitive to changes in $m$. Heavier charges move more slowly, and their reduced mobility delays the spreading or contraction of the string, thereby prolonging thermalization.

In conclusion, increasing $D$, $l_0$, or $m$ leads to slower outward expansion of the string, keeping the charges closer together for a longer time. This is analogous to quarkonia thermalization in a QGP, where a more localized wavefunction results in slower decoherence and delayed thermalization [130, 280]. Specifically in [280], it is further emphasized that the dissipation plays an important role not only for late time but also for early time dynamics as we have observed also in Fig. 6.2. Additionally, they note that the drag force prevents the quarkonia from dissociating within the QGP, balancing the thermal fluctuations, and that a smaller mass leads to a more spatially extended wavefunction that decoheres faster, thereby thermalizing faster.

### 6.1.2. Correlations between thermalization time and mutual information

Following from the previous discussion on dissociation, we now investigate the effect of $D$, $l_0$, and $m$ on the quantum mutual information for the same fixed parameters $N = 12, T = 10$. The quantum mutual information is defined as

$$S(\rho) = -\mathrm{Tr}(\rho \ln \rho), \tag{6.1}$$

$$I(A, B) = S(\rho_A) + S(\rho_B) - S(\rho_{AB}), \tag{6.2}$$

where the first equation describes the von Neumann entropy. The subsystems $A$ and $B$ represent two contiguous subregions of the full system, with the subscript notation on $\rho_A$ and $\rho_B$ indicating that all other degrees of freedom have been traced out.

To quantify the evolution of correlations between different parts of the system, we track the subtracted mutual information (SMI) $\Delta I$ between lattice sites $4, 5$ and $6, 7$, corresponding to opposite halves of the initial electric flux string. As outlined in Sec. 6.1, $\Delta I$ is defined as the difference between the mutual information computed for the case where the initial state is the Dirac vacuum modified to include the charge pair and the mutual information of the pure Dirac vacuum state. This allows us to probe the entanglement structure between the two halves of the string, where one side contains the positive charge and the other the negative charge.

The results are presented in Fig. 6.6. Consistent with our previous findings that larger values of $D$, $m$, and $l_0$ slow down dissociation, we observe that increasing any of these parameters delays the decrease of SMI towards $\Delta I = 0$, as highlighted in the inset of the figure. This

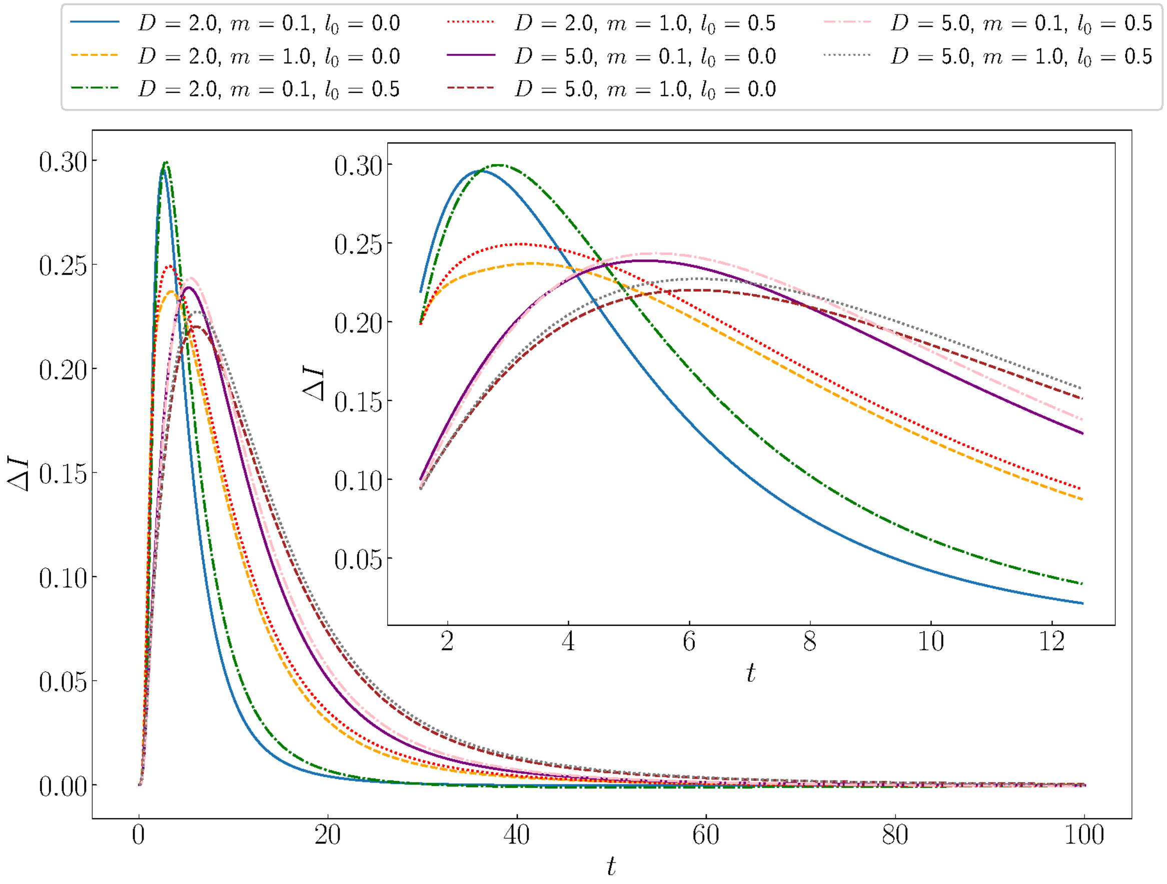

**Figure 6.6:** *Subtracted mutual information (SMI) $\Delta I$ as a function of time $t$ for the parameter sets in the four corners of Fig. 6.3(a, d) at $N = 12$. The mutual information is measured between sites 4,5 and 6,7. The initial string extends between sites 4 to 7, hence the two regions 4,5 and 6,7 measure the mutual information between the two halves of the original string. The inset focuses on the times between 10 and 20 to emphasize how fast the SMI of each parameter set decreases. The resolution in $t$ is fine enough that the data is quasi-continuous and connected with lines.*

trend reflects the fact that stronger dissipation, larger mass, or a stronger background field suppress the spreading of the charges, thereby prolonging correlations between the two regions.

Additionally, the peak of the SMI during the transient dynamics is affected by these parameters. Namely, increasing $l_0$ raises the peak, whereas increasing $D$ or $m$ lowers it. This behavior can be understood as follows. A stronger background field $l_0$ compresses the charges, keeping them spatially closer, which enhances initial entanglement and increases the peak value of $\Delta I$. In contrast, larger values of $D$ and $m$ suppress kinetic energy, reducing the spread of the charges in any direction and thereby lowering the amount of entanglement generated.

Since the system initially starts from a product state with zero mutual information, any parameter that brings the charges closer together will first lead to an increase in $\Delta I$, before it eventually decreases to zero as the system reaches its steady state. Further, parameters that localize the charges more effectively lead to a slower relaxation of $\Delta I$ back to zero, which can be observed in the late-time behavior of the curves in Fig. 6.6.

As mentioned in the introduction to this chapter, we have observed that mutual information can provide numerically consistent results with experimental observations. For example, we have seen above, that a larger $m$ leads to a prolonged coherence of the string, which also gives a longer thermalization time. The latter has also been observed in quarkonia experiments within the QGP [287–290].

### 6.1.3. Temperature dependence

The temperature $T$ is another crucial parameter in heavy-ion collision experiments, which motivates dedicating this section to exploring its effect on the thermalization time $\mathcal{T}$ of the string. The temperature range explored lies above $T = 10$ to satisfy the requirement from QBM that $T \gg H_S$, as discussed in Sec. 6.1.1.

Figure 6.7 presents $\mathcal{T}$ as a function of $T$ for $D = 2, 5$, $l_0 = 0.0, 0.5$, and $m = 0.1, 1.0$. The key takeaway from this plot is that the thermalization time increases with temperature. This trend, characteristic of the Schwinger model, deviates from the behavior expected for quarkonia in QGP [291]. At lower temperatures, $\mathcal{T}$ increases non-linearly with $T$, and beyond a certain threshold, the system enters a linear regime. The figure also reaffirms previous findings that for a broad range of temperatures, increasing $D$, $l_0$, or $m$ systematically results in a longer thermalization time $\mathcal{T}$.

In Eq. (A3) of [126], the relaxation rate is approximated with a quadratic dependence on the Lindblad jump operators in the numerator. Expanding this dependence yields a sum of terms scaling as $1/T^0$, $1/T$, and $1/T^2$. As a result, the thermalization time is inversely related to this sum, explaining both the increase in thermalization time with temperature, as seen in Fig. 6.7, and the transition from nonlinear to linear behavior. To model this trend quantitatively, we fit the data in Fig. 6.7 using the function

$$f(T) = \frac{a}{(b + c/T)^2}, \tag{6.3}$$

where $a, b$, and $c$ are fitting parameters. This function closely matches the observed trend.

In contrast, QCD exhibits a different temperature dependence due to the behavior of $D(k)$. Specifically, $D(k)$ follows a $T^3$ scaling, leading to an increase in the relaxation rate as temperature rises. This emanates from the connection between $D(k)$ and the heavy quark diffusion coefficient $\kappa$, which has been demonstrated to scale as $T^3$ [120, 280, 292, 293].

To further analyze the impact of temperature, we present in Fig. 6.9 the SMI as a function of time for $D = 5.0$, $m = 1.0$, and $l_0 = 0.5$, over a temperature range of $T \in [7, 100]$. The results indicate that increasing $T$ leads to a higher peak in $\Delta I$ and accelerates the decrease of mutual information towards its steady-state value. These effects, while subtle, may be understood as follows. A higher peak in $\Delta I$ at larger $T$ suggests that increasing temperature allows the string's charges to develop stronger correlations during the transient regime. This observation is supported by Fig. 6.8($a$), which compares the SKE for $T = 7$ and $T = 100$. The data show that $\Delta K$ reaches a smaller peak at higher temperatures, implying that the

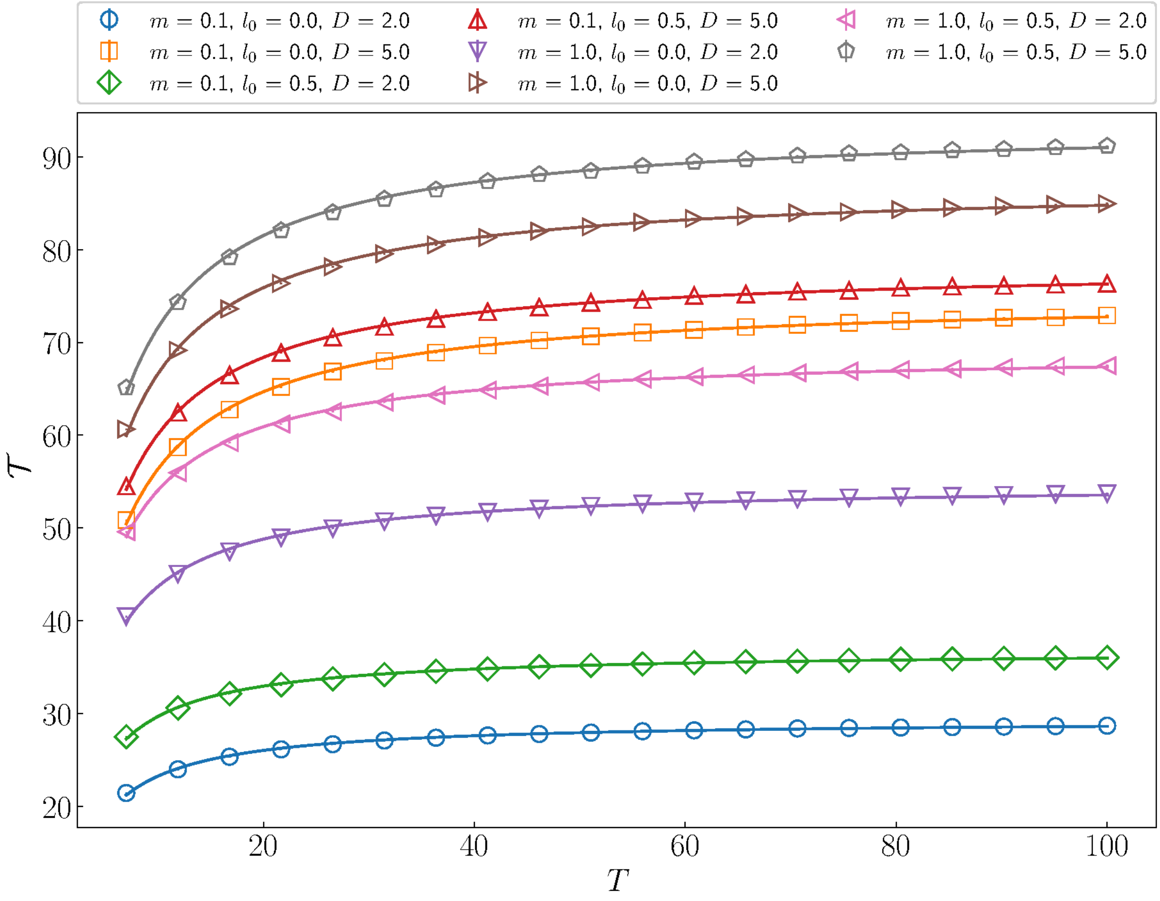

**Figure 6.7:** *Thermalization time* $\mathcal{T}$ *as a function of the environment's temperature* $T$ *for* $N = 12$, $D = 2, 5$, $l_0 = 0.0, 0.5$, $m = 0.1, 1.0$. *The error bars, which are not visible due to the y-scale of the plot, are estimated to be* 0.1 *as inferred from the data in table 6.1 and discussed in Sec. 6.1.4. The lines represent the fit described by Eq.* (6.3).

charges may remain spatially closer for a longer time as $T$ increases.

At late times, increasing $T$ appears to accelerates the decrease of $\Delta I$ towards zero. This may be attributed to enhanced particle production at higher temperatures, which weakens the string tension through the creation of screening charges, thereby diminishing correlations more rapidly. This screening effect may be comparable to the screening that quarkonia experience in QGP, which in turn affects their yield, with higher QGP temperatures resulting in a decreased quarkonia yield [276, 294, 295]. Figure 6.8($b$) provides numerical evidence for the higher particle production, displaying the total particle number (PN) $\mathcal{P}$ defined as

$$\mathcal{P} = \frac{N}{2} + \frac{1}{2}\sum_{n=0}^{N-1}(-1)^n Z_n. \tag{6.4}$$

This definition coincides with Eq. (5.4), nevertheless we follow here the notation of [62] for this chapter. By comparing $\mathcal{P}$ at $T = 7$ and $T = 100$, we observe that higher temperatures result in greater particle production, which can facilitate string screening and accelerate the decrease of $\Delta I$.

Further insights can be obtained from figures 6.8($c$) and 6.8($d$), which display the SEF as a function of link number $n$ and time $t$ for $T = 7$ and $T = 100$, respectively. At $t = 50$, we observe that links 3 and 8 exhibit a larger $\Delta F(n)$ at $T = 100$ than at $T = 7$, indicating that the string expands more with increasing temperature at later times. This behavior is consistent with Fig. 6.8($a$), where the late-time decrease of $\Delta K$ is slower for $T = 100$ compared to $T = 7$. The crossover point, occurring around $t = 50$, marks the moment when $\Delta K$ for $T = 7$ falls below that of $T = 100$. Figure 6.8($d$) further illustrates the longer thermalization time at higher temperatures, as the middle links maintain a higher $\Delta F(n)$ at late times compared to Fig. 6.8($c$).

### 6.1.4. Larger system sizes and symmetry preservation

As a final subsection for the case of the string, we present results on larger system sizes. To confirm that our findings are not significantly influenced by finite-size effects, we provide quantitative comparisons in Table 6.1, where thermalization times are evaluated for different parameter sets at $N = 12$ and $N = 24$, keeping $T = 10$ fixed. The results show agreement up to one decimal place, allowing us to estimate an uncertainty of approximately $\mathcal{O}(0.1)$ for the reported thermalization times in this chapter.

For additional qualitative insight, Fig. 6.10 illustrates the SEF per link number at different time steps for both system sizes. This comparison demonstrates that, for the chosen parameters, the dynamics of the $N = 24$ case closely resemble those of $N = 12$, while benefiting from a reduced influence of boundary effects. Despite this qualitative difference in boundary effects, Table 6.1 shows agreement between the two system sizes. The figure also offers a visual representation of the SEF's progression toward thermal equilibrium. In particular, transitioning from Fig. 6.10($a$) to ($b$), where $D$ increases from 2 to 5 while keeping $l_0 = 0$ and

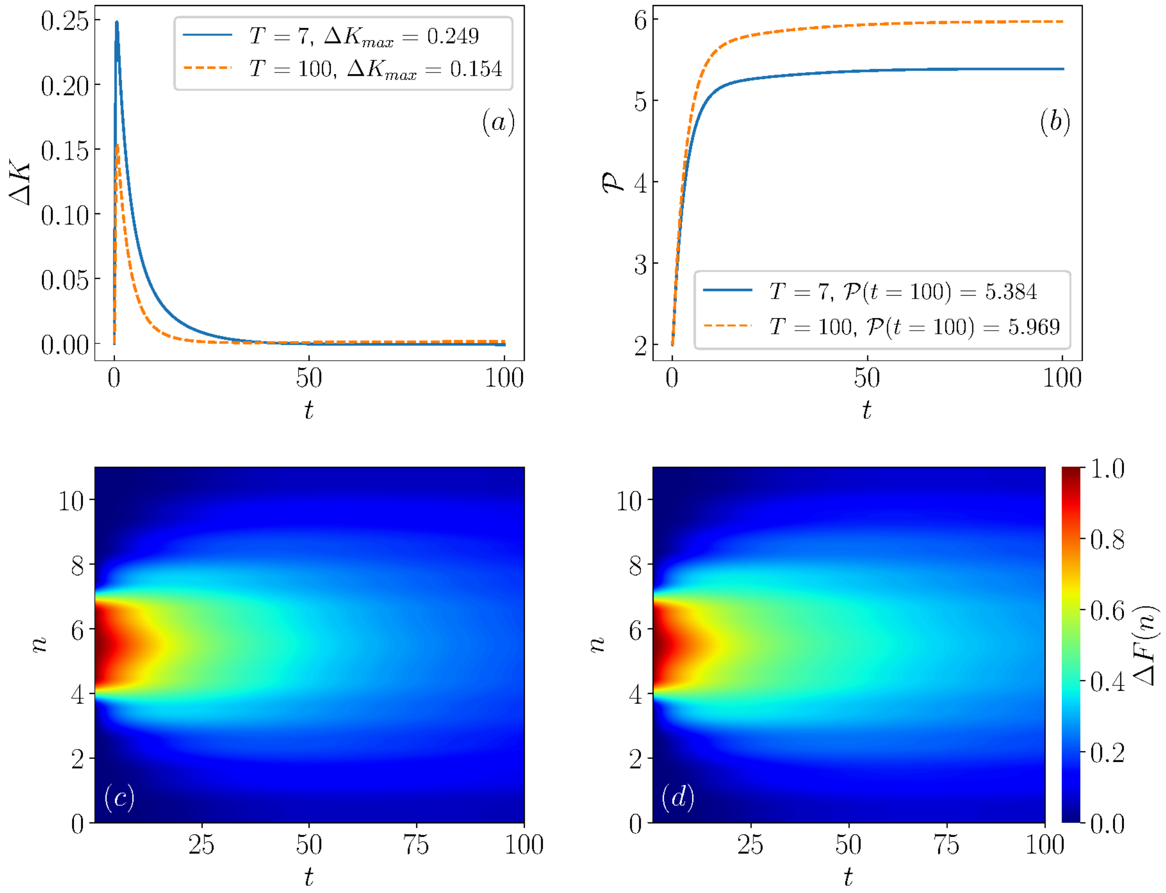

**Figure 6.8:** *$(a)$: Subtracted kinetic energy (SKE) $\Delta K$, $(b)$: particle number (PN) $\mathcal{P}$ for the case where the initial state is the Dirac vacuum with the string present $\mathcal{P}$ $(b)$, both as a function of time $t$. In $(a)$ the legend gives the value of $\Delta K$ at the peak and in $(b)$ the legend gives the final value of $\mathcal{P}$ at time $t = 100$. The comparison is drawn between temperatures $T = 7$ and $T = 100$. The bottom two subplots $(c)$, $(d)$ show the subtracted electric field (SEF) $\Delta F(n)$ as a function of the link number $n$ and time $t$ for $T = 7, 100$ respectively. All plots have fixed parameters $N = 12$, $D = 5$, $l_0 = 0.5$ and $m = 1.0$.*

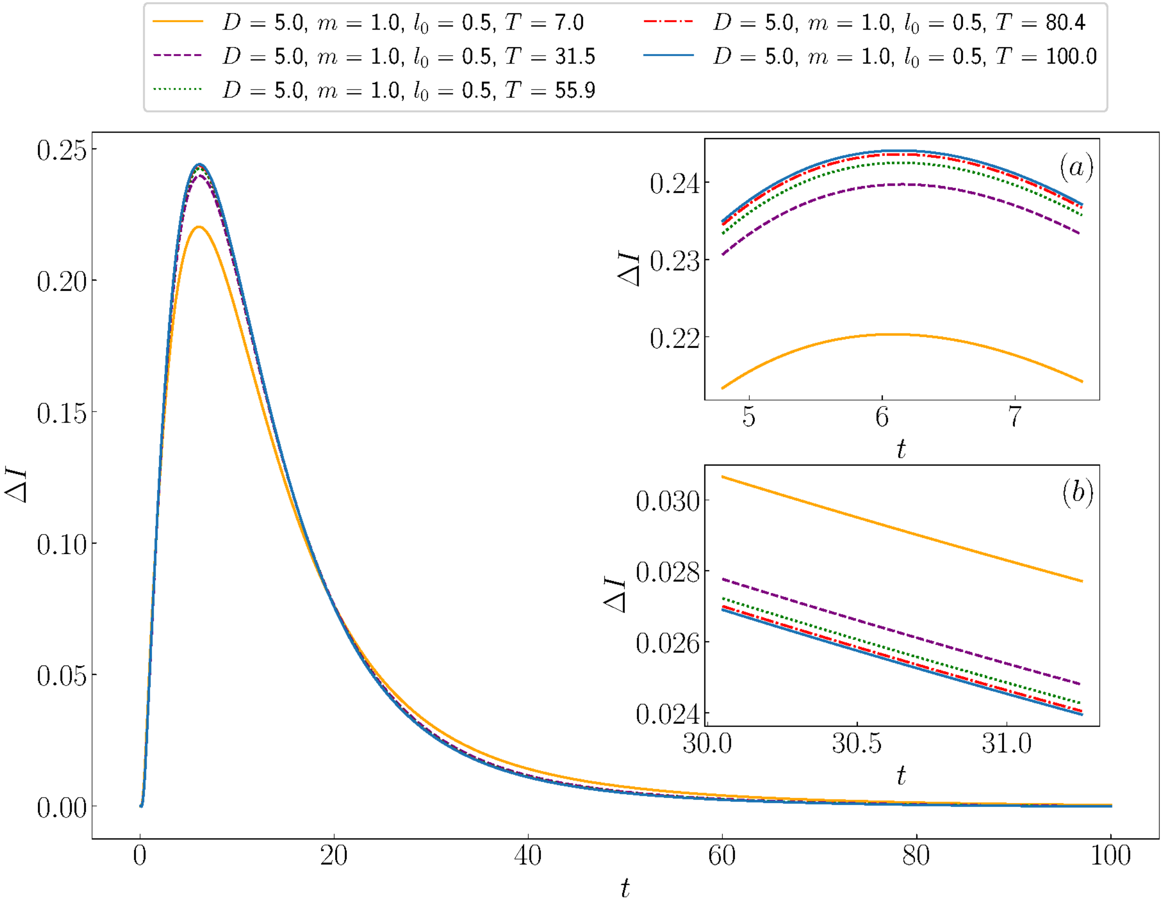

**Figure 6.9:** *Subtracted mutual information (SMI) $\Delta I$ as a function of time $t$ for $D = 5.0$, $m = 1.0$, $l_0 = 0.5$ and $T \in [7, 100]$. Inset $(a)$ focuses on the peak of $\Delta I$ and inset $(b)$ on the order at which different temperatures decrease to the steady state value $\Delta I = 0$ in late times.*

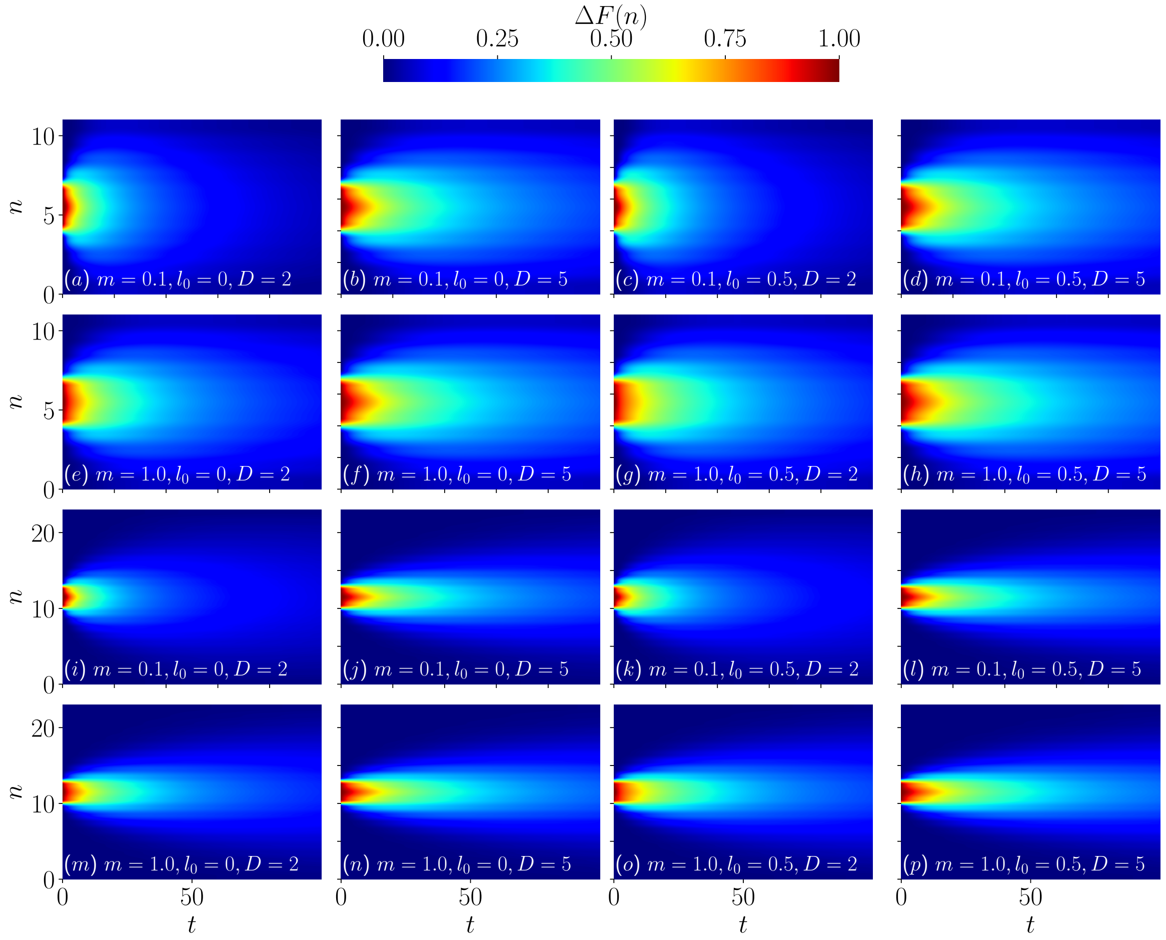

**Figure 6.10:** *Subtracted electric field (SEF) $\Delta F(n)$ per link number $n$ as a function of time $t$ for $N = 12, 24$, with parameter values $l_0 = 0.0, 0.5$, $D = 2.0, 5.0$, and $m = 0.1, 1.0$. Additional parameter details are provided in Section 6.1. The SEF approaches zero upon thermalization, and the data indicate that increasing $D$, $l_0$, and $m$ results in longer thermalization times. Doubling the system size further mitigates boundary effects.*

$m = 0.1$, results in a more concentrated red region near the central link. This is likely due to the combined effects of dissipative slowing of charge motion and electrostatic attraction pulling the charges together. Changes in $l_0$ and $m$ primarily extend the nonzero SEF region, though these effects are subtler in this qualitative representation.

The choice of dissipator $D(n-k) = D\delta_{n,k}$ ensures weak charge conjugation - parity (CP) conservation, which implies $[CP \otimes CP, \mathcal{L}] = 0$ [127], where $CP$ represents the CP operator. Under this formulation, the electric field maintains reflection symmetry around the central link [127]. Fig. 6.11 illustrates the degree to which our algorithm preserves this symmetry. The parameters used are $N = 100$, $D = 0.15$, $x = 4$, $m = 0$, and $\tau = 0.001$, with other parameters defined in Section 6.1. These values were specifically chosen to align with those used in Fig. 8$(a)$ of [127], where a neural network method was applied to a smaller system of $N = 20$.

Figure 6.11$(c)$ plots the absolute difference in SEF between symmetrically paired links,

| $D$ | $l_0$ | $m = 0.1$ | | $m = 1.0$ | |
|---|---|---|---|---|---|
| | | $N = 12$ | $N = 24$ | $N = 12$ | $N = 24$ |
| 2.0 | 0.0 | 23.32 | 23.39 | 43.66 | 43.92 |
| 3.58 | 0.0 | 40.89 | 41.14 | 54.14 | 53.93 |
| 5.0 | 0.0 | 56.56 | 56.64 | 66.98 | 66.96 |
| 2.0 | 0.26 | 26.15 | 26.63 | 48.68 | 49.26 |
| 3.58 | 0.26 | 42.90 | 43.35 | 56.75 | 57.23 |
| 5.0 | 0.26 | 58.20 | 58.78 | 68.86 | 69.25 |
| 2.0 | 0.5 | 29.72 | 30.70 | 53.98 | 55.45 |
| 3.58 | 0.5 | 45.10 | 45.77 | 59.99 | 60.90 |
| 5.0 | 0.5 | 59.72 | 60.36 | 71.12 | 71.87 |

**Table 6.1:** *Thermalization times for different parameters at $N = 12$ and $N = 24$. Other parameter values are provided in Section 6.1.*

defined as $P = |\Delta F(n = i) - \Delta F(n = N - i - 2)|$ for $i \in [0, 48]$. The results indicate that our algorithm preserves this symmetry with an average accuracy of $\mathcal{O}\left(10^{-4}\right)$, with the mean discrepancy across all links being $P_{\text{avg}} = 0.0006$. The corresponding SEF per link as a function of time is shown in Fig. 6.11$(a,\ b)$, which qualitatively aligns with the behavior observed in [127]. However, our method demonstrates improved performance in maintaining reflection symmetry, as well as improved accuracy and stability for large systems, even at $N = 100$. This figure also serves as an example of string breaking prior to full thermalization.

This completes our study of the string thermalization in the hot environment. Moving to the last section of this chapter, we will explore another type of mesonic state given by the theory's stable particle, that we have aforementioned throughout this thesis.

## 6.2. Schwinger boson thermalization

The second meson-type initial state examined is the first excited state of the system Hamiltonian in Eq. (1.36). To isolate the behavior of the Schwinger boson, the stable mesonic state of the theory with weak self-interactions [56] discussed in previous chapters, we subtract from observables the corresponding values with respect to the ground state of $H_S$. To differentiate these subtracted quantities from those in the string case, we introduce the subscript $B$, for instance, using $\Delta F_B(n)$ to denote the SEF.

This section serves as an independent verification of the trends identified in the string scenario, particularly regarding the relationship between thermalization time and dissipator strength. Unlike in the string case, the states analyzed here exhibit entanglement from the outset, leading to more complex dynamics. The first set of findings, depicted in Fig. 6.12$(a - f)$, is obtained for fixed parameters $N = 14$, $T = 10$, $l_0 = 0$, and $m = 0$. Panels $(a - c)$ illustrate the evolution of the SEF, $\Delta F_B(n)$, for different values of $D \in [2, 3.5, 5]$. A qualitative examination reveals that as $D$ increases, the system requires a longer time to thermalize, as inferred from the evolution of $\Delta F_B(n)$ at the middle link $n = 6$. These results confirm that

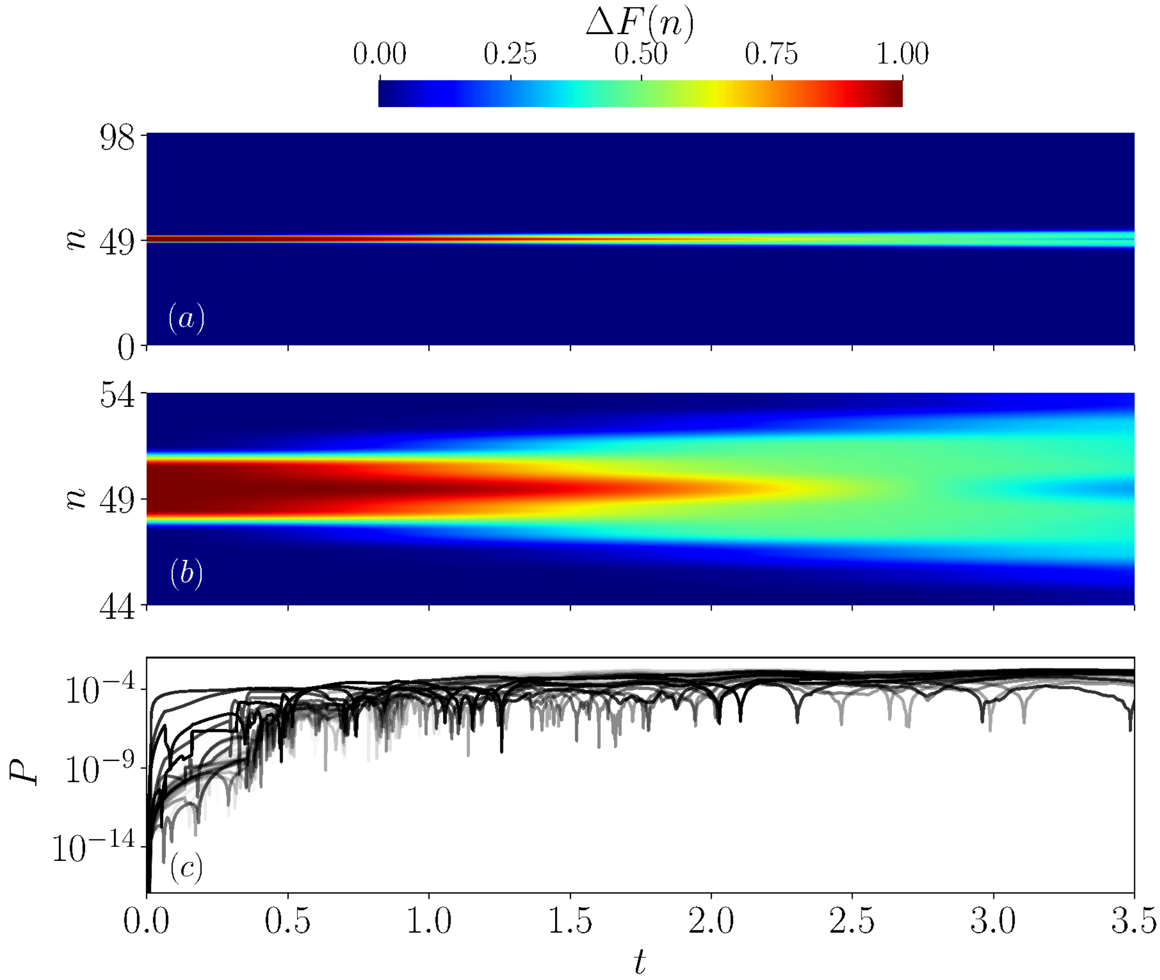

**Figure 6.11:** *(a): Subtracted electric field (SEF)* $\Delta F(n)$ *per link number* $n$ *over time* $t$ *for* $N = 100$, $D = 0.15$, $x = 4$, $m = 0$, $\tau = 0.001$. *(b): Close-up of the middle region of subplot (a). (c): Absolute SEF difference between symmetric link pairs,* $P = |\Delta F(n = i) - \Delta F(n = N - i - 2)|$, *for* $i \in [0, 48]$, *using data from (a). The algorithm preserves reflection symmetry around the central link with an average accuracy of* $\mathcal{O}\left(10^{-4}\right)$. *The darkest line corresponds to the link pair closest to the center, while the brightest line represents the first and last links.*

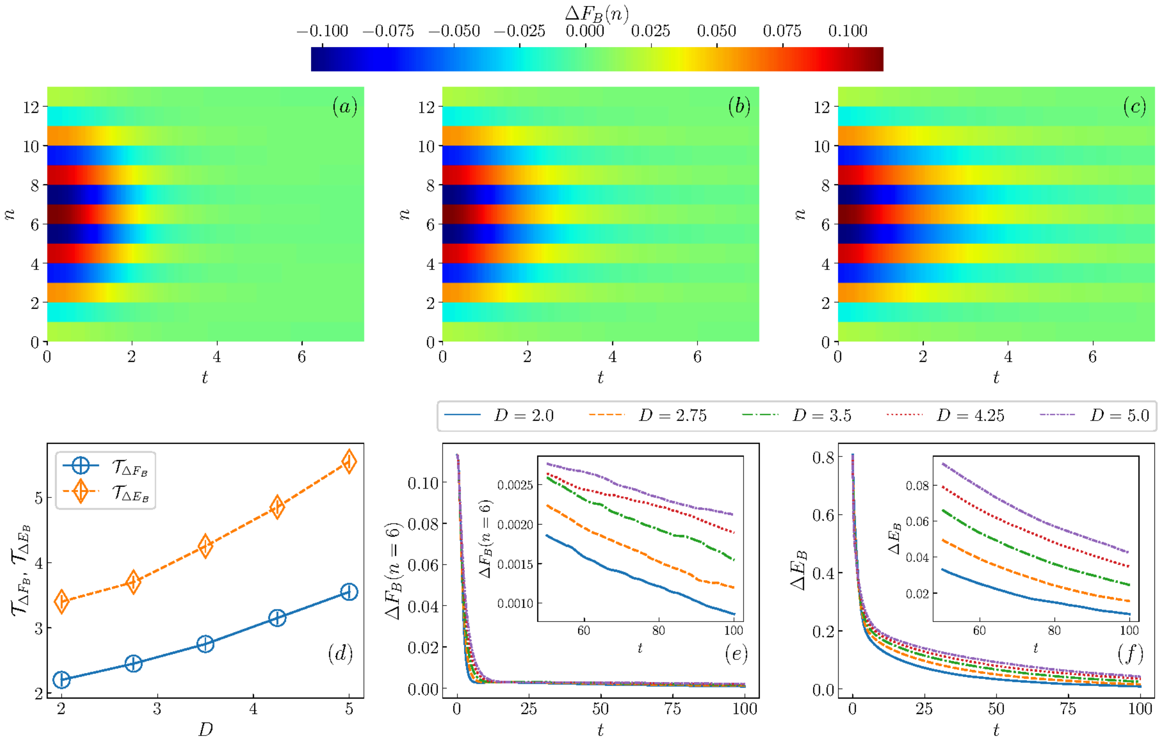

**Figure 6.12:** $(a)-(c)$: *Subtracted electric field (SEF) of the Schwinger boson, $\Delta F_B(n)$, per link number $n$ as a function of time $t$ for $D = 2, 3.5, 5$. $(d)$: Comparison of thermalization time measured using the SEF ($\mathcal{T}_{\Delta F_B}$) and the subtracted energy ($\mathcal{T}_{\Delta E_B}$) as a function of the dissipator strength $D$. $(e)$, $(f)$: Time evolution of SEF and subtracted energy, respectively, for different values of $D$. The insets highlight the long-time behavior. In $(e)$ and $(f)$, individual data points are omitted for clarity, as the time steps are finely spaced.*

the dependence of the thermalization time on $D$ observed for the string state is also present in the Schwinger boson case.

Panel $(d)$ presents a quantitative analysis of the thermalization time $\mathcal{T}$, estimated using both the electric field at $n = 6$, denoted $\mathcal{T}_{\Delta F_B}$, and the subtracted total energy $\Delta E_B$ of $H_S$, denoted $\mathcal{T}_{\Delta E_B}$. The subtracted energy serves as an additional reference to validate the behavior of $\mathcal{T}$ with respect to $D$. The figure demonstrates that both measures of thermalization time exhibit the same increasing trend with $D$, though $\mathcal{T}_{\Delta E_B}$ consistently yields higher values. Panels $(e)$ and $(f)$ display the time evolution of $\Delta F_B(n = 6)$ and $\Delta E_B$, respectively. The insets emphasize the long-time regime, where Trotterization errors become more pronounced, introducing some irregularities in the curves. Despite this, the insets reinforce the conclusion that larger values of $D$ correspond to slower thermalization.

Another set of key observables for the Schwinger boson case is shown in Fig. 6.13. Panel $(a)$ presents the evolution of the subtracted particle number (SPN), $\Delta\mathcal{P}_B$, where $\mathcal{P}_B$ is the expectation value of the operator defined in Eq. (6.4). Initially, $\Delta\mathcal{P}_B$ is close to 2, reflecting the mesonic nature of the Schwinger boson, which consists of two bound particles. Panel $(b)$ displays the SKE as a function of time. Both panels illustrate that as $D$ increases, the system

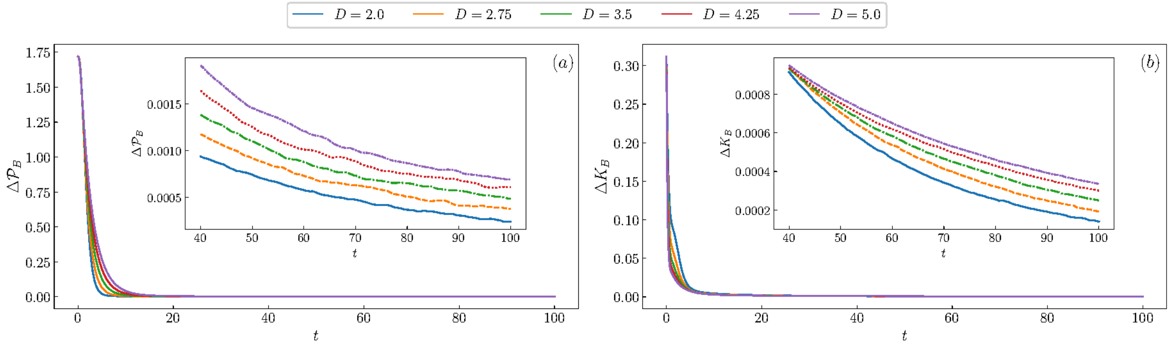

**Figure 6.13:** $(a)$: *Time evolution of the subtracted particle number (SPN)* $\Delta\mathcal{P}_B$ *for the Schwinger boson.* $(b)$: *Evolution of the subtracted kinetic energy (SKE),* $\Delta K_B$. *Both plots demonstrate how increasing the dissipator strength* $D$ *slows the thermalization process. The insets highlight the long-time behavior. Individual data points are omitted for clarity due to the fine time resolution.*

thermalizes at a slower rate.

# Conclusion

The Schwinger model serves as a benchmark model for quantum chromodynamics (QCD), sharing key features such as the confinement of fermionic degrees of freedom into mesons. This similarity makes it an important tool for developing numerical methods in strongly interacting gauge theories. Throughout this thesis, we have employed the Schwinger model to advance techniques in tensor network (TN) and quantum computing (QC), as well as to explore its physics.

In Chapter 1, we introduced the continuum Schwinger model with a single fermion flavour in the Hamiltonian formulation, incorporating a topological $\theta$-term. We analyzed its phase diagram, particularly along the $\theta = \pi$ axis, which exhibits first- and second-order phase transitions along with spontaneous charge conjugation - parity (CP) breaking, which is a feature shared with QCD and relevant to the strong CP problem. Additionally, we discussed mass perturbation theory, the mesonic Schwinger boson, and the axial anomaly, which establishes the model's periodicity in $\theta$.

For numerical simulations, we employed a lattice formulation, presenting two fermion discretization schemes, Wilson and staggered fermions, to mitigate fermion doubling. We also introduced the Schwinger model within open quantum system (OQS) and formulated its evolution via the Lindblad master equation in the Markovian quantum Brownian motion (QBM) limit.

Given their broad applications, TNs provide a powerful framework for quantum many-body physics (QMBP). In Chapter 2, we focused on matrix product state (MPS) and matrix product operator (MPO) architectures, detailing algorithms such as the density matrix renormalization group (DMRG) and the adaptive time-dependent DMRG (ATD-DMRG) for ground state search and time evolution. Beyond TNs, in Chapter 3 we explored QC for QMBP, introducing quantum circuits, the variational quantum eigensolver (VQE) algorithm, and various error mitigation techniques for noisy intermediate-scale quantum (NISQ) devices.

Chapter 4 focused on the mass shift (MS) within the Hamiltonian formulation of lattice gauge theory (LGT), which enables the study of non-perturbative effects in strongly coupled systems such as QCD. We developed methods to extract the MS using results from continuum mass perturbation theory and key observables like the electric field density (EFD) and energy gap. Our findings show that incorporating the MS significantly improves continuum extrapolations, yielding more accurate results with reduced error bounds. Additionally, we demonstrated that including the MS allows for meaningful extrapolations even at larger lattice spacings, reducing computational costs. These results, including the successful extrapolation of the EFD and precise determination of the Schwinger boson mass to three decimal places, validate the efficacy of our methods for broader applications in LGT.

In Chapter 5, we explored the potential of QC to simulate the first-order phase transition in the Schwinger model. Given the limitations of classical simulations, QC presents a promising alternative. We implemented the VQE algorithm on classical simulators, comparing Wilson and staggered fermions, testing different variational ansätze, and optimizing circuit architectures. These simulations were then executed using inference runs on IBM's superconducting quantum computers, where we employed state-of-the-art error mitigation techniques. Our findings demonstrate that, despite hardware noise, current quantum devices can simulate the phase diagram of a LGT, marking an important step toward quantum simulations of more complex theories such as QCD. Furthermore, by leveraging MPS simulations and MS methods, we performed continuum extrapolations to estimate the resources needed for continuum extrapolations to be performed with QC. Our results suggest that, while feasible with current NISQ technology, achieving high precision will require significant improvements in hardware and algorithms.

Chapter 6 extended our studies to OQS, motivated by the Schwinger model's relevance to QCD and the study of mesonic states in hot environments, similar to quarkonia in the quark gluon plasma (QGP). This chapter marked the first application of TNs to LGTs within the OQS framework. Using the ATD-DMRG algorithm, we investigated the time evolution of the density matrix in the Markovian QBM limit. Beyond exploring the dependence of the thermalization time on various parameters, our study revealed correlations between the thermalization time and mutual information. Additionally, we demonstrated the scalability of our approach, successfully simulating systems of up to 100 sites while preserving the theoretically predicted EFD parity symmetry. These results highlight the potential of TN methods for studying the time evolution of OQS.

This thesis paves the way for more precise calculations in LGTs using TNs and QC while expanding their applications to OQSs. Looking ahead, extending the MS method to other LGTs could eventually enable the use of the Hamiltonian formulation for QCD, which circumvents the sign problem and allows for the exploration of previously inaccessible regions of its phase diagram. Moreover, integrating the MS approach into QC simulations helps to mitigate errors in NISQ devices by allowing for smaller system sizes to be used without compromising accuracy in continuum extrapolations. Advancing these methods to higher spatial dimensions is another crucial step, as it would facilitate the simulation of gauge theories relevant to the Standard Model. Further, more realistic scenarios can be considered in the case of OQS, where a spatiotemporal variation of the environment's temperature can capture the expanding nature of the QGP.

# Bibliography

[1] F. Englert and R. Brout. “Broken Symmetry and the Mass of Gauge Vector Mesons”. In: *Phys. Rev. Lett.* 13 (9 1964), pp. 321–323. DOI: `10.1103/PhysRevLett.13.321`.

[2] Peter W. Higgs. “Broken Symmetries and the Masses of Gauge Bosons”. In: *Phys. Rev. Lett.* 13 (16 1964), pp. 508–509. DOI: `10.1103/PhysRevLett.13.508`.

[3] Sheldon L. Glashow. “Partial-symmetries of weak interactions”. In: *Nuclear Physics* 22.4 (1961), pp. 579–588. ISSN: 0029-5582. DOI: `https://doi.org/10.1016/0029-5582(61)90469-2`.

[4] Edilson Reyes and Raffaele Fazio. “High-Precision Calculations of the Higgs Boson Mass”. In: *Particles* 5.1 (2022), pp. 53–73. ISSN: 2571-712X. DOI: `10.3390/particles5010006`.

[5] M. Awramik et al. “Precise prediction for the W-boson mass in the standard model”. In: *Phys. Rev. D* 69 (5 2004), p. 053006. DOI: `10.1103/PhysRevD.69.053006`.

[6] Stephen P. Martin. “Three-loop QCD corrections to the electroweak boson masses”. In: *Phys. Rev. D* 106 (1 2022), p. 013007. DOI: `10.1103/PhysRevD.106.013007`.

[7] Tatsumi Aoyama, Toichiro Kinoshita, and Makiko Nio. “Revised and improved value of the QED tenth-order electron anomalous magnetic moment”. In: *Phys. Rev. D* 97 (3 2018), p. 036001. DOI: `10.1103/PhysRevD.97.036001`.

[8] J. C. Collins and M. J. Perry. “Superdense Matter: Neutrons or Asymptotically Free Quarks?” In: *Phys. Rev. Lett.* 34 (21 1975), pp. 1353–1356. DOI: `10.1103/PhysRevLett.34.1353`.

[9] Ágnes Mócsy, Péter Petreczky, and Michael Strickland. “Quarkonia in the quark gluon plasma”. In: *International Journal of Modern Physics A* 28.11 (2013), p. 1340012. DOI: `10.1142/S0217751X13400125`.

[10] N. Cabibbo and G. Parisi. “Exponential hadronic spectrum and quark liberation”. In: *Physics Letters B* 59.1 (1975), pp. 67–69. ISSN: 0370-2693. DOI: `https://doi.org/10.1016/0370-2693(75)90158-6`.

[11] Constantia Alexandrou et al. “Ruling Out the Massless Up-Quark Solution to the Strong $CP$ Problem by Computing the Topological Mass Contribution with Lattice QCD”. In: *Phys. Rev. Lett.* 125 (23 2020), p. 232001. DOI: `10.1103/PhysRevLett.125.232001`.

[12] Daniele S. M. Alves and Neal Weiner. "A viable QCD axion in the MeV mass range". In: *Journal of High Energy Physics* 2018.7 (2018), p. 92. DOI: 10.1007/JHEP07(2018)092.

[13] Roberto D. Peccei. "The Strong CP Problem and Axions". In: *Axions: Theory, Cosmology, and Experimental Searches*. Ed. by Markus Kuster, Georg Raffelt, and Berta Beltrán. Berlin, Heidelberg: Springer Berlin Heidelberg, 2008, pp. 3–17. ISBN: 978-3-540-73518-2. DOI: 10.1007/978-3-540-73518-2_1.

[14] Thomas Mannel. "Theory and Phenomenology of CP Violation". In: *Nuclear Physics B - Proceedings Supplements* 167 (2007). Proceedings of the 7th International Conference on Hyperons, Charm and Beauty Hadrons, pp. 170–174. ISSN: 0920-5632. DOI: https://doi.org/10.1016/j.nuclphysbps.2006.12.083.

[15] A. D. Sakharov. "Violation of CP Invariance, C asymmetry, and baryon asymmetry of the universe". In: *Pisma Zh. Eksp. Teor. Fiz.* 5 (1967), pp. 32–35. DOI: 10.1070/PU1991v034n05ABEH002497.

[16] John B. Kogut. "The lattice gauge theory approach to quantum chromodynamics". In: *Rev. Mod. Phys.* 55 (3 1983), pp. 775–836. DOI: 10.1103/RevModPhys.55.775.

[17] Franz Gross et al. "50 Years of quantum chromodynamics". In: *The European Physical Journal C* 83.12 (2023), p. 1125. DOI: 10.1140/epjc/s10052-023-11949-2.

[18] Y. Aoki et al. *FLAG Review 2024*. 2025. arXiv: 2411.04268 [hep-lat].

[19] Martin Hansen et al. "Gauge invariant determination of charged hadron masses". In: *JHEP* 05 (2018), p. 146. DOI: 10.1007/JHEP05(2018)146. arXiv: 1802.05474 [hep-lat].

[20] Richard D. Ball et al. "Parton distributions with QED corrections". In: *Nucl. Phys. B* 877 (2013), pp. 290–320. DOI: 10.1016/j.nuclphysb.2013.10.010. arXiv: 1308.0598 [hep-ph].

[21] Frithjof Karsch. "Lattice results on QCD thermodynamics". In: *Nucl. Phys. A* 698 (2002). Ed. by T. J. Hallman et al., pp. 199–208. DOI: 10.1016/S0375-9474(01)01365-3. arXiv: hep-ph/0103314.

[22] Frithjof Karsch. "Lattice QCD at High Temperature and Density". In: *Lectures on Quark Matter*. Ed. by Willibald Plessas and Leopold Mathelitsch. Berlin, Heidelberg: Springer Berlin Heidelberg, 2002, pp. 209–249. ISBN: 978-3-540-45792-3. DOI: 10.1007/3-540-45792-5_6.

[23] Sz. Borsanyi et al. "Leading hadronic contribution to the muon magnetic moment from lattice QCD". In: *Nature* 593.7857 (2021), pp. 51–55. DOI: 10.1038/s41586-021-03418-1.

[24] K. Nagata. "Finite-density lattice QCD and sign problem: Current status and open problems". In: *Progress in Particle and Nuclear Physics* 127 (2022), p. 103991. DOI: 10.1016/j.ppnp.2022.103991.

[25] Bañuls, Mari Carmen et al. "Towards overcoming the Monte Carlo sign problem with tensor networks". In: *EPJ Web Conf.* 137 (2017), p. 04001. DOI: `10.1051/epjconf/201713704001`.

[26] Nancy Makri and William H. Miller. "Monte carlo integration with oscillatory integrands: implications for feynman path integration in real time". In: *Chemical Physics Letters* 139.1 (1987), pp. 10–14. ISSN: 0009-2614. DOI: `https://doi.org/10.1016/0009-2614(87)80142-2`.

[27] Andrei Alexandru et al. "Monte Carlo Study of Real Time Dynamics on the Lattice". In: *Physical Review Letters* 117 (2016), p. 081602. DOI: `10.1103/PhysRevLett.117.081602`.

[28] Christof Gattringer and Kurt Langfeld. "Approaches to the sign problem in lattice field theory". In: *International Journal of Modern Physics A* 31.22 (2016), p. 1643007. DOI: `10.1142/S0217751X16430077`. eprint: `https://doi.org/10.1142/S0217751X16430077`.

[29] Ulrich Schollwöck. "The density-matrix renormalization group in the age of matrix product states". In: *Annals of Physics* 326.1 (2011). January 2011 Special Issue, pp. 96–192. ISSN: 0003-4916. DOI: `https://doi.org/10.1016/j.aop.2010.09.012`.

[30] Román Orús. "A Practical Introduction to Tensor Networks: Matrix Product States and Projected Entangled Pair States". In: *Annals of Physics* 349 (2014), pp. 117–158. DOI: `10.1016/j.aop.2014.06.013`.

[31] Alberto Di Meglio et al. "Quantum Computing for High-Energy Physics: State of the Art and Challenges". In: *PRX Quantum* 5 (3 2024), p. 037001. DOI: `10.1103/PRXQuantum.5.037001`.

[32] Lena Funcke et al. "Review on Quantum Computing for Lattice Field Theory". In: *PoS* LATTICE2022 (2023), p. 228. DOI: `10.22323/1.430.0228`.

[33] Mari Carmen Bañuls et al. "Simulating lattice gauge theories within quantum technologies". In: *The European Physical Journal D* 74.8 (2020), p. 165. DOI: `10.1140/epjd/e2020-100571-8`.

[34] Mari Carmen Bañuls et al. "Tensor Networks and their use for Lattice Gauge Theories". In: *36th Annual International Symposium on Lattice Field Theory*. 2018. DOI: `10.22323/1.334.0022`. arXiv: `1810.12838 [hep-lat]`.

[35] Giovanni Cataldi et al. "Simulating $(2+1)$D SU(2) Yang-Mills lattice gauge theory at finite density with tensor networks". In: *Phys. Rev. Res.* 6 (3 2024), p. 033057. DOI: `10.1103/PhysRevResearch.6.033057`.

[36] Timo Felser et al. "Two-Dimensional Quantum-Link Lattice Quantum Electrodynamics at Finite Density". In: *Phys. Rev. X* 10 (4 2020), p. 041040. DOI: `10.1103/PhysRevX.10.041040`.

[37] G. Vidal. “Class of Quantum Many-Body States That Can Be Efficiently Simulated”. In: *Phys. Rev. Lett.* 101 (11 2008), p. 110501. DOI: `10.1103/PhysRevLett.101.110501`.

[38] Giuseppe Magnifico et al. *Tensor Networks for Lattice Gauge Theories beyond one dimension: a Roadmap.* 2024. arXiv: `2407.03058 [hep-lat]`.

[39] M. A. Nielsen and I. L. Chuang. *Quantum Computation and Quantum Information.* 10th Anniversary Edition. Chapter 10, p. 334-338. Cambridge University Press, 2010.

[40] Boye Buyens et al. “Matrix Product States for Gauge Field Theories”. In: *Physical Review Letters* 113.9 (9 2014), p. 091601. DOI: `10.1103/PhysRevLett.113.091601`.

[41] E. Rico et al. “Tensor Networks for Lattice Gauge Theories and Atomic Quantum Simulation”. In: *Physical Review Letters* 112.20 (20 2014), p. 201601. DOI: `10.1103/PhysRevLett.112.201601`.

[42] T. Pichler et al. “Real-Time Dynamics in $U(1)$ Lattice Gauge Theories with Tensor Networks”. In: *Phys. Rev. X* 6 (1 2016), p. 011023. DOI: `10.1103/PhysRevX.6.011023`.

[43] Mari Carmen Bañuls et al. “Density Induced Phase Transitions in the Schwinger Model: A Study with Matrix Product States”. In: *Phys. Rev. Lett.* 118 (7 2017), p. 071601. DOI: `10.1103/PhysRevLett.118.071601`.

[44] Elisa Ercolessi et al. “Phase transitions in $Z_n$ gauge models: Towards quantum simulations of the Schwinger-Weyl QED”. In: *Physical Review D* 98.7 (7 2018), p. 074503. DOI: `10.1103/PhysRevD.98.074503`.

[45] Giuseppe Magnifico et al. “Real Time Dynamics and Confinement in the $\mathbb{Z}_n$ Schwinger-Weyl lattice model for 1+1 QED”. en. In: *Quantum* 4 (2020). arXiv:1909.04821 [cond-mat, physics:hep-lat, physics:hep-th, physics:quant-ph], p. 281. ISSN: 2521-327X. DOI: `10.22331/q-2020-06-15-281`.

[46] Lena Funcke, Karl Jansen, and Stefan Kühn. “Topological Vacuum Structure of the Schwinger Model with Matrix Product States”. In: *Physical Review D* 101.5 (2020), p. 054507. DOI: `10.1103/PhysRevD.101.054507`.

[47] Marco Rigobello et al. “Entanglement generation in (1+1)D QED scattering processes”. In: *Phys. Rev. D* 104 (11 2021), p. 114501. DOI: `10.1103/PhysRevD.104.114501`.

[48] Lena Funcke, Karl Jansen, and Stefan Kühn. “Exploring the $CP$-violating Dashen phase in the Schwinger model with tensor networks”. In: *Phys. Rev. D* 108 (1 2023), p. 014504. DOI: `10.1103/PhysRevD.108.014504`.

[49] Jesse Osborne, Ian P. McCulloch, and Jad C. Halimeh. “Probing Confinement Through Dynamical Quantum Phase Transitions: From Quantum Spin Models to Lattice Gauge Theories”. In: *arXiv* (2023). arXiv: `2310.12210 [cond-mat.quant-gas]`.

[50] Ron Belyansky et al. “High-Energy Collision of Quarks and Mesons in the Schwinger Model: From Tensor Networks to Circuit QED”. In: *Phys. Rev. Lett.* 132 (9 2024), p. 091903. DOI: `10.1103/PhysRevLett.132.091903`.

[51] Irene Papaefstathiou, Johannes Knolle, and Mari Carmen Bañuls. “Real-time scattering in the lattice Schwinger model”. In: *Phys. Rev. D* 111 (1 2025), p. 014504. DOI: 10.1103/PhysRevD.111.014504.

[52] Jared Jeyaretnam et al. “Hilbert space fragmentation at the origin of disorder-free localization in the lattice Schwinger model”. In: *arXiv* (2024). arXiv: 2409.08320 [quant-ph].

[53] Yibin Guo et al. *Concurrent VQE for Simulating Excited States of the Schwinger Model*. 2024. arXiv: 2407.15629 [quant-ph].

[54] Satoshi Iso and Hitoshi Murayama. “Hamiltonian Formulation of the Schwinger Model: Non-Confinement and Screening of the Charge”. In: *Progress of Theoretical Physics* 84.1 (1990), pp. 142–163. ISSN: 0033-068X. DOI: 10.1143/ptp/84.1.142.

[55] Christoph Adam. “Massive Schwinger model within mass perturbation theory”. In: *Annals Phys.* 259 (1997), pp. 1–63. DOI: 10.1006/aphy.1997.5697. arXiv: hep-th/9704064.

[56] Sidney R. Coleman. “More About the Massive Schwinger Model”. In: *Annals Phys.* 101 (1976), p. 239. DOI: 10.1016/0003-4916(76)90280-3.

[57] C. J. Hamer, M. Moshe, and J. B. Kogut. “The Massive Schwinger Model on a Lattice: Background Field, Chiral Symmetry and the String Tension”. In: *Nuclear Physics B* 201 (1982), pp. 242–258. DOI: 10.1016/0550-3213(82)90076-6.

[58] I. C. E. Turcu et al. “High field physics and QED experiments at ELI-NP”. In: *Rom. Rep. Phys.* 68.Supplement (2016), S145.

[59] Takis Angelides et al. “Mass Renormalization of the Schwinger Model with Wilson and Staggered Fermions in the Hamiltonian Lattice Formulation”. In: *PoS* LATTICE2022 (2023), p. 046. DOI: 10.22323/1.430.0046.

[60] Takis Angelides et al. “Computing the Mass Shift of Wilson and Staggered Fermions in the Lattice Schwinger Model with Matrix Product States”. In: *Physical Review D* 108 (2023), p. 014516. DOI: 10.1103/PhysRevD.108.014516.

[61] Takis Angelides et al. “First-order phase transition of the Schwinger model with a quantum computer”. In: *npj Quantum Information* 11.1 (2025), p. 6. DOI: 10.1038/s41534-024-00950-6.

[62] Takis Angelides et al. “Meson thermalization with a hot medium in the open Schwinger model”. In: *Journal of High Energy Physics* 2025.4 (2025), p. 195. DOI: 10.1007/JHEP04(2025)195.

[63] Sidney R. Coleman, R. Jackiw, and Leonard Susskind. “Charge Shielding and Quark Confinement in the Massive Schwinger Model”. In: *Annals Phys.* 93 (1975), p. 267. DOI: 10.1016/0003-4916(75)90212-2.

[64] Y. Nambu and G. Jona-Lasinio. “Dynamical Model of Elementary Particles Based on an Analogy with Superconductivity. I”. In: *Physical Review* 122.1 (1961), pp. 345–358. DOI: 10.1103/PhysRev.122.345.

[65] J. H. Lowenstein and J. A. Swieca. “Quantum electrodynamics in two-dimensions”. In: *Annals Phys.* 68 (1971), pp. 172–195. DOI: 10.1016/0003-4916(71)90246-6.

[66] Boye Buyens et al. “Real-time simulation of the Schwinger effect with Matrix Product States”. In: *Physical Review D* 96.11 (2017). arXiv:1612.00739 [cond-mat, physics:hep-lat, physics:quant-ph], p. 114501. ISSN: 2470-0010, 2470-0029. DOI: 10.1103/PhysRevD.96.114501.

[67] Lento Nagano, Aniruddha Bapat, and Christian W. Bauer. “Quench dynamics of the Schwinger model via variational quantum algorithms”. In: *Physical Review D* 108.3 (2023). arXiv:2302.10933 [cond-mat, physics:hep-lat, physics:hep-ph, physics:hep-th, physics:quant-ph], p. 034501. ISSN: 2470-0010, 2470-0029. DOI: 10.1103/PhysRevD.108.034501.

[68] N. Klco et al. “Quantum-classical computation of Schwinger model dynamics using quantum computers”. In: *Physical Review A* 98.3 (2018). ISSN: 2469-9934. DOI: 10.1103/physreva.98.032331.

[69] Giulia Mazzola et al. “Gauge-invariant quantum circuits for $U(1)$ and Yang-Mills lattice gauge theories”. In: *Phys. Rev. Res.* 3 (4 2021), p. 043209. DOI: 10.1103/PhysRevResearch.3.043209.

[70] Wibe A. de Jong et al. “Quantum simulation of nonequilibrium dynamics and thermalization in the Schwinger model”. In: *Phys. Rev. D* 106 (5 2022), p. 054508. DOI: 10.1103/PhysRevD.106.054508.

[71] Wenjie Gong et al. “Measurement of Bell-type inequalities and quantum entanglement from $\Lambda$-hyperon spin correlations at high energy colliders”. In: *Phys. Rev. D* 106 (3 2022), p. L031501. DOI: 10.1103/PhysRevD.106.L031501.

[72] Julius Mildenberger et al. “Confinement in a $${{\mathbb{Z}}}_{2}$$lattice gauge theory on a quantum computer”. In: *Nature Physics* 21.2 (2025), pp. 312–317. DOI: 10.1038/s41567-024-02723-6.

[73] Clement Charles et al. “Simulating $\mathbb{Z}_2$ lattice gauge theory on a quantum computer”. In: *Phys. Rev. E* 109 (1 2024), p. 015307. DOI: 10.1103/PhysRevE.109.015307.

[74] Domenico Pomarico et al. “Dynamical Quantum Phase Transitions of the Schwinger Model: Real-Time Dynamics on IBM Quantum”. In: *Entropy* 25.4 (2023). ISSN: 1099-4300. DOI: 10.3390/e25040608.

[75] Alessio Lerose. *Simulating Schwinger model dynamics with quasi-one-dimensional qubit arrays.* 2024. arXiv: 2409.14544 [quant-ph].

[76] Alexander Mil et al. “A scalable realization of local U(1) gauge invariance in cold atomic mixtures”. In: *Science* 367.6482 (2020), pp. 1128–1130. DOI: 10.1126/science.aaz5312. eprint: https://www.science.org/doi/pdf/10.1126/science.aaz5312.

[77] Bing Yang et al. “Observation of gauge invariance in a 71-site Bose–Hubbard quantum simulator”. In: *Nature* 587.7834 (2020), pp. 392–396. DOI: 10.1038/s41586-020-2910-8.

[78] Zhao-Yu Zhou et al. “Thermalization dynamics of a gauge theory on a quantum simulator”. In: *Science* 377.6603 (2022), pp. 311–314. DOI: 10.1126/science.abl6277. eprint: https://www.science.org/doi/pdf/10.1126/science.abl6277.

[79] Guo-Xian Su et al. “Observation of many-body scarring in a Bose-Hubbard quantum simulator”. In: *Phys. Rev. Res.* 5 (2 2023), p. 023010. DOI: 10.1103/PhysRevResearch.5.023010.

[80] Wei-Yong Zhang et al. “Observation of microscopic confinement dynamics by a tunable topological $\theta$-angle”. In: *Nature Physics* 21.1 (2025), pp. 155–160. DOI: 10.1038/s41567-024-02702-x.

[81] Esteban A. Martinez et al. “Real-time dynamics of lattice gauge theories with a few-qubit quantum computer”. In: *Nature* 534.7608 (2016), pp. 516–519. DOI: 10.1038/nature18318.

[82] C. Kokail et al. “Self-verifying variational quantum simulation of lattice models”. In: *Nature* 569.7756 (2019), pp. 355–360. DOI: 10.1038/s41586-019-1177-4.

[83] Nhung H. Nguyen et al. “Digital Quantum Simulation of the Schwinger Model and Symmetry Protection with Trapped Ions”. In: *PRX Quantum* 3 (2 2022), p. 020324. DOI: 10.1103/PRXQuantum.3.020324.

[84] Niklas Mueller et al. “Quantum Computation of Dynamical Quantum Phase Transitions and Entanglement Tomography in a Lattice Gauge Theory”. In: *PRX Quantum* 4 (3 2023), p. 030323. DOI: 10.1103/PRXQuantum.4.030323.

[85] S. Montangero, M. P. A. Fisher, and C. F. Roos. “Quantum simulations of the Schwinger model with trapped ions”. In: *Physical Review A* 96.6 (2017), p. 063615. DOI: 10.1103/PhysRevA.96.063615.

[86] A. J. Daley et al. “Simulating the Schwinger model with ultracold atoms in optical lattices”. In: *Physical Review Letters* 109.7 (2012), p. 070502. DOI: 10.1103/PhysRevLett.109.070502.

[87] Julian Schwinger. “Gauge Invariance and Mass. II”. In: *Physical Review* 128.5 (1962), pp. 2425–2429. DOI: 10.1103/PhysRev.128.2425.

[88] S. S. Schweber. “Quantum Electrodynamics in the Temporal Gauge”. In: *Physical Review D* 36.6 (1987), pp. 1830–1839. DOI: 10.1103/PhysRevD.36.1830.

[89] Carolo Friderico Gauss. “Theoria Attractionis Corporum Sphaeroidicorum Ellipticorum Homogeneorum”. In: *Werke: Fünfter Band*. Berlin, Heidelberg: Springer Berlin Heidelberg, 1877, pp. 3–22. DOI: `10.1007/978-3-642-49319-5_1`.

[90] John David Jackson. *Classical electrodynamics*. 3rd ed. New York, NY: Wiley, 1999.

[91] David Tong. *Quantum Field Theory*. `http://www.damtp.cam.ac.uk/user/tong/qft.html`. Lecture Notes, University of Cambridge. 2006.

[92] H. Blaine Lawson and Marie-Louise Michelsohn. *Spin Geometry*. Princeton, NJ: Princeton University Press, 1989.

[93] Michael E. Peskin and Daniel V. Schroeder. *An Introduction to Quantum Field Theory*. Chapter on Local Gauge Transformations and Gauge Theory. Reading, MA: Addison-Wesley, 1995.

[94] A. Zee. *Quantum Field Theory in a Nutshell*. Princeton, NJ: Princeton University Press, 2003.

[95] Emmy Noether and. “Invariant variation problems”. In: *Transport Theory and Statistical Physics* 1.3 (1971), pp. 186–207. DOI: `10.1080/00411457108231446`. eprint: `https://doi.org/10.1080/00411457108231446`.

[96] T. Byrnes et al. “Density Matrix Renormalization Group Approach to the Massive Schwinger Model”. In: *Nuclear Physics B* 636 (2002), pp. 536–550. DOI: `10.1016/S0550-3213(02)00304-3`.

[97] Hiroki Ohata. “Phase diagram near the quantum critical point in Schwinger model at $\theta = \pi$: analogy with quantum Ising chain”. In: *Progress of Theoretical and Experimental Physics* 2024.1 (2023), 013B02. ISSN: 2050-3911. DOI: `10.1093/ptep/ptad151`. eprint: `https://academic.oup.com/ptep/article-pdf/2024/1/013B02/55446166/ptad151.pdf`.

[98] David Tong. *Gauge Theory*. `https://www.damtp.cam.ac.uk/user/tong/gaugetheory.html`. 2006.

[99] Kazuo Fujikawa. “Path-Integral Measure for Gauge-Invariant Fermion Theories”. In: *Phys. Rev. Lett.* 42 (18 1979), pp. 1195–1198. DOI: `10.1103/PhysRevLett.42.1195`.

[100] I. Montvay and G. Münster. *Quantum Fields on a Lattice*. 1st. Cambridge: Cambridge University Press, 1997.

[101] C. Gattringer and C. B. Lang. *Quantum Chromodynamics on the Lattice*. 1st. Berlin: Springer, 2010.

[102] H. J. Rothe. *Lattice Gauge Theories: An Introduction*. 4th. Singapore: World Scientific, 2005.

[103] H. B. Nielsen and M. Ninomiya. “A no-go theorem for regularizing chiral fermions”. In: *Physics Letters B* 105.2-3 (1981), pp. 219–223. DOI: `10.1016/0370-2693(81)90524-1`.

[104] Kenneth G. Wilson. “Confinement of quarks”. In: *Physical Review D* 10.8 (1974), pp. 2445–2459. DOI: 10.1103/PhysRevD.10.2445.

[105] Rajan Gupta et al. “Kaon $B$ parameter with Wilson fermions”. In: *Phys. Rev. D* 47 (11 1993), pp. 5113–5127. DOI: 10.1103/PhysRevD.47.5113.

[106] E. Follana and H. Panagopoulos. “Critical mass of Wilson fermions: A comparison of perturbative and Monte Carlo results”. In: *Phys. Rev. D* 63 (1 2000), p. 017501. DOI: 10.1103/PhysRevD.63.017501.

[107] Michael Creutz. “Chiral symmetry on the lattice”. In: *Nuclear Physics B - Proceedings Supplements* 42.1 (1995), pp. 56–66. ISSN: 0920-5632. DOI: https://doi.org/10.1016/0920-5632(95)00187-E.

[108] T V Zache et al. “Quantum simulation of lattice gauge theories using Wilson fermions”. In: *Quantum Science and Technology* 3.3 (2018), p. 034010. DOI: 10.1088/2058-9565/aac33b.

[109] C. J. Hamer, Zheng Weihong, and J. Oitmaa. “Series expansions for the massive Schwinger model in Hamiltonian lattice theory”. In: *Phys. Rev. D* 56 (1 1997), pp. 55–67. DOI: 10.1103/PhysRevD.56.55.

[110] Pascual Jordan and Eugene P. Wigner. “About the Pauli exclusion principle”. In: *Z. Phys.* 47 (1928), pp. 631–651. DOI: 10.1007/BF01331938.

[111] John Kogut and Leonard Susskind. “Hamiltonian formulation of Wilson’s lattice gauge theories”. In: *Phys. Rev. D* 11 (2 1975), pp. 395–408. DOI: 10.1103/PhysRevD.11.395.

[112] Lena Funcke, Karl Jansen, and Stefan Kühn. “CP-violating Dashen phase transition in the two-flavor Schwinger model: a study with matrix product states”. In: *Physical Review D* 104.5 (2021), p. 054507. DOI: 10.1103/PhysRevD.104.054507.

[113] H. P. Breuer and F. Petruccione. *The theory of open quantum systems*. Oxford University Press, USA, 2002.

[114] Fabrizio Minganti and Alberto Biella. “Open quantum systems – A brief introduction”. In: *arXiv* (2024). arXiv: 2407.16855 [quant-ph].

[115] Heinz-Peter Breuer and Francesco Petruccione. “Concepts and Methods in the Theory of Open Quantum Systems”. In: *Irreversible Quantum Dynamics*. Ed. by Fabio Benatti and Roberto Floreanini. Berlin, Heidelberg: Springer Berlin Heidelberg, 2003, pp. 65–79. DOI: 10.1007/3-540-44874-8_4.

[116] Yoshiro Takahashi. “Cold atom realization of dissipative Hubbard model as open quantum system emulation”. In: *Cold-atom systems as condensed matter physics emulation*. Ed. by Tapash Chakraborty. Academic Press, 2024, pp. 135–144. DOI: https://doi.org/10.1016/B978-0-323-90800-9.00271-7.

[117] Bharath Sambasivam. “Open Quantum Systems in High Energy Physics”. PhD thesis. Syracuse University, 2024.

[118] R. Rapp, D. Blaschke, and P. Crochet. “Charmonium and bottomonium in heavy-ion collisions”. In: *Progress in Particle and Nuclear Physics* 65.2 (2010), pp. 209–266. ISSN: 0146-6410. DOI: `https://doi.org/10.1016/j.ppnp.2010.07.002`.

[119] Yasuo Miake Takafumi Niida. “Signatures of QGP at RHIC and the LHC”. In: *AAPPS Bulletin* 31.1 (2021), p. 12. DOI: `10.1007/s43673-021-00014-3`.

[120] Xiaojun Yao. “Open quantum systems for quarkonia”. In: *International Journal of Modern Physics A* 36.20 (2021), p. 2130010. DOI: `10.1142/S0217751X21300106`.

[121] McKibben Lofnes, Ingrid and for the ALICE Collaboration. “Quarkonia as probes of the QGP and of the initial stages of the heavy-ion collision with ALICE”. In: *EPJ Web Conf.* 259 (2022), p. 12004. DOI: `10.1051/epjconf/202225912004`.

[122] Ramamurti Shankar. *Principles of Quantum Mechanics*. 2nd, 19th corrected printing. New York, NY: Springer, 2014.

[123] Leslie Ballentine. “Density Matrix”. In: *Compendium of Quantum Physics*. Berlin, Heidelberg: Springer Berlin Heidelberg, 2009, p. 166. DOI: `10.1007/978-3-540-70626-7_51`.

[124] U. Fano. “Description of States in Quantum Mechanics by Density Matrix and Operator Techniques”. In: *Reviews of Modern Physics* 29.1 (1957), pp. 74–93. DOI: `10.1103/RevModPhys.29.74`.

[125] Alexander S. Holevo. *Statistical Structure of Quantum Theory*. Lecture Notes in Physics. Springer, 2001.

[126] Kyle Lee et al. “Liouvillian dynamics of the open Schwinger model: String breaking and kinetic dissipation in a thermal medium”. In: *Phys. Rev. D* 108 (9 2023), p. 094518. DOI: `10.1103/PhysRevD.108.094518`.

[127] Joshua Lin et al. “Real-time dynamics of the Schwinger model as an open quantum system with Neural Density Operators”. In: *Journal of High Energy Physics* 2024.6 (2024), p. 211. DOI: `10.1007/JHEP06(2024)211`.

[128] Göran Lindblad. “On the generators of quantum dynamical semigroups”. In: *Communications in Mathematical Physics* 48.2 (1976), pp. 119–130. DOI: `10.1007/BF01608499`.

[129] U. Weiss. *Quantum Dissipative Systems*. 3rd. World Scientific, 2012.

[130] Y. Akamatsu. “Quarkonium in quark–gluon plasma: Open quantum system approaches re-examined”. In: *Progress in Particle and Nuclear Physics* 123 (2022), p. 103932. ISSN: 0146-6410. DOI: `https://doi.org/10.1016/j.ppnp.2021.103932`.

[131] Román Orús. “Tensor networks for complex quantum systems”. In: *Nature Reviews Physics* 1.9 (2019), pp. 538–550. DOI: `10.1038/s42254-019-0086-7`.

[132] John. TM. Campbell. *Bridging Relations between SVD in Tensor Networks and Common Matrix Operations in Quantum Information Theory*. 2024. arXiv: `2402.02517 [math.QA]`.

[133] F. Verstraete and Juan Ignacio Cirac. "Renormalization algorithms for Quantum-Many Body Systems in two and higher dimensions". In: *arXiv: Strongly Correlated Electrons* (2004).

[134] Hans-Martin Rieser, Frank Köster, and Arne Peter Raulf. "Tensor Networks for Quantum Machine Learning". In: *Proceedings of the Royal Society A* 479.2277 (2023), p. 20230218. DOI: `10.1098/rspa.2023.0218`.

[135] Mario Collura et al. *Tensor Network Techniques for Quantum Computation.* SISSA Medialab S.r.l., 2024. DOI: `10.22323/9788898587049`.

[136] Igor L. Markov and Yaoyun Shi. "Simulating Quantum Computation by Contracting Tensor Networks". In: *SIAM Journal on Computing* 38.3 (2008), pp. 963–981. DOI: `10.1137/050644756`. eprint: `https://doi.org/10.1137/050644756`.

[137] Jielun Chen, E.M. Stoudenmire, and Steven R. White. "Quantum Fourier Transform Has Small Entanglement". In: *PRX Quantum* 4 (4 2023), p. 040318. DOI: `10.1103/PRXQuantum.4.040318`.

[138] Joseph Tindall et al. "Efficient Tensor Network Simulation of IBM's Eagle Kicked Ising Experiment". In: *PRX Quantum* 5 (1 2024), p. 010308. DOI: `10.1103/PRXQuantum.5.010308`.

[139] Martin Kiffner and Dieter Jaksch. "Tensor network reduced order models for wall-bounded flows". In: *Physical Review Fluids* 8.12 (2023), p. 124101. DOI: `10.1103/PhysRevFluids.8.124101`.

[140] Raghavendra Dheeraj Peddinti et al. "Quantum-inspired framework for computational fluid dynamics". In: *Communications Physics* 7.1 (2024), p. 135. DOI: `10.1038/s42005-024-01623-8`.

[141] Borja Aizpurua et al. *Quantum Large Language Models via Tensor Network Disentanglers.* 2024. arXiv: `2410.17397 [quant-ph]`.

[142] Hao Chen and Thomas Barthel. "Machine Learning With Tree Tensor Networks, CP Rank Constraints, and Tensor Dropout". In: *IEEE Transactions on Pattern Analysis and Machine Intelligence* 46.12 (2024), pp. 7825–7832. DOI: `10.1109/TPAMI.2024.3396386`.

[143] Ian Convy and K Birgitta Whaley. "Interaction decompositions for tensor network regression". In: *Machine Learning: Science and Technology* 3.4 (2022), p. 045027. DOI: `10.1088/2632-2153/aca271`.

[144] Ivan Glasser, Nicola Pancotti, and J. Ignacio Cirac. "From Probabilistic Graphical Models to Generalized Tensor Networks for Supervised Learning". In: *IEEE Access* 8 (2020), pp. 68169–68182. DOI: `10.1109/ACCESS.2020.2986279`.

[145] Edwin Stoudenmire and David J Schwab. "Supervised Learning with Tensor Networks". In: *Advances in Neural Information Processing Systems* 29 (2016).

[146] Alexander Novikov, Mikhail Trofimov, and Ivan Oseledets. *Exponential Machines*. 2017. arXiv: `1605.03795 [stat.ML]`.

[147] Sander Wahls et al. "Learning multidimensional Fourier series with tensor trains". In: *2014 IEEE Global Conference on Signal and Information Processing (GlobalSIP)* (2014), pp. 394–398. DOI: `10.1109/GlobalSIP.2014.7032146`.

[148] Yian Chen and Yuehaw Khoo. *Combining Monte Carlo and Tensor-network Methods for Partial Differential Equations via Sketching*. 2023. arXiv: `2305.17884 [math.NA]`.

[149] Yifan Peng et al. *Generative Modeling via Hierarchical Tensor Sketching*. 2023. arXiv: `2304.05305 [math.NA]`.

[150] Alexander Lidiak et al. *Quantum state tomography with tensor train cross approximation*. 2022. arXiv: `2207.06397 [quant-ph]`.

[151] YoonHaeng Hur et al. "Generative modeling via tensor train sketching". In: *Applied and Computational Harmonic Analysis* 67 (2023), p. 101575. ISSN: 1063-5203. DOI: `https://doi.org/10.1016/j.acha.2023.101575`.

[152] Yuriel Núñez Fernández et al. "Learning Feynman Diagrams with Tensor Trains". In: *Phys. Rev. X* 12 (4 2022), p. 041018. DOI: `10.1103/PhysRevX.12.041018`.

[153] Tom Vieijra, Laurens Vanderstraeten, and Frank Verstraete. *Generative modeling with projected entangled-pair states*. 2022. arXiv: `2202.08177 [quant-ph]`.

[154] Jing Liu et al. "Tensor networks for unsupervised machine learning". In: *Phys. Rev. E* 107 (1 2023), p. L012103. DOI: `10.1103/PhysRevE.107.L012103`.

[155] Song Cheng et al. "Tree tensor networks for generative modeling". In: *Physical Review B* 99.15 (2019). ISSN: 2469-9969. DOI: `10.1103/physrevb.99.155131`.

[156] Zhao-Yu Han et al. "Unsupervised Generative Modeling Using Matrix Product States". In: *Phys. Rev. X* 8 (3 2018), p. 031012. DOI: `10.1103/PhysRevX.8.031012`.

[157] Samuel T. Wauthier et al. *Learning Generative Models for Active Inference using Tensor Networks*. 2022. arXiv: `2208.08713 [cs.LG]`.

[158] Friederike Metz and Marin Bukov. "Self-correcting quantum many-body control using reinforcement learning with tensor networks". In: *Nature Machine Intelligence* 5.7 (2023), pp. 780–791. DOI: `10.1038/s42256-023-00687-5`.

[159] Szilárd Szalay et al. "Tensor product methods and entanglement optimization for ab initio quantum chemistry". In: *International Journal of Quantum Chemistry* 115.19 (2015), pp. 1342–1391. DOI: `https://doi.org/10.1002/qua.24898`. eprint: `https://onlinelibrary.wiley.com/doi/pdf/10.1002/qua.24898`.

[160] Marcos Díez García and Antonio Márquez Romero. "Survey on Computational Applications of Tensor-Network Simulations". In: *IEEE Access* 12 (2024), pp. 193212–193228. DOI: `10.1109/ACCESS.2024.3519676`.

[161] Debarshi Kundu et al. “Application of Quantum Tensor Networks for Protein Classification”. In: *Proceedings of the Great Lakes Symposium on VLSI 2024*. 2024, p. 132. DOI: `10.1145/3649476.3658701`.

[162] Abhishek Samlodia et al. “Phase diagram of generalized XY model using the tensor renormalization group”. In: *Phys. Rev. D* 110 (3 2024), p. 034504. DOI: `10.1103/PhysRevD.110.034504`.

[163] Matthias Troyer and Uwe-Jens Wiese. “Computational Complexity and Fundamental Limitations to Fermionic Quantum Monte Carlo Simulations”. In: *Physical Review Letters* 94 (2005), p. 170201. DOI: `10.1103/PhysRevLett.94.170201`.

[164] Jens Eisert, Marcus Cramer, and Martin B. Plenio. “Colloquium: Area laws for the entanglement entropy”. In: *Reviews of Modern Physics* 82.1 (2010), pp. 277–306. DOI: `10.1103/RevModPhys.82.277`.

[165] Jiarui Zhao et al. “Measuring Rényi entanglement entropy with high efficiency and precision in quantum Monte Carlo simulations”. In: *npj Quantum Materials* 7.1 (2022), p. 69. DOI: `10.1038/s41535-022-00476-0`.

[166] Regina Finsterhölzl et al. “Using Matrix-Product States for Open Quantum Many-Body Systems: Efficient Algorithms for Markovian and Non-Markovian Time-Evolution”. en. In: *Entropy* 22.9 (2020), p. 984. ISSN: 1099-4300. DOI: `10.3390/e22090984`.

[167] Florian A. Y. N. Schröder and Alex W. Chin. “Simulating open quantum dynamics with time-dependent variational matrix product states: Towards microscopic correlation of environment dynamics and reduced system evolution”. In: *Physical Review B* 93.7 (2016). arXiv:1507.02202 [cond-mat, physics:quant-ph], p. 075105. ISSN: 2469-9950, 2469-9969. DOI: `10.1103/PhysRevB.93.075105`.

[168] Yuchen Guo, Ke Ding, and Shuo Yang. *A New Framework for Quantum Phases in Open Systems: Steady State of Imaginary-Time Lindbladian Evolution*. 2024. arXiv: `2408.03239 [quant-ph]`.

[169] Roland C. Farrell et al. “Scalable Circuits for Preparing Ground States on Digital Quantum Computers: The Schwinger Model Vacuum on 100 Qubits”. In: *PRX Quantum* 5 (2 2024), p. 020315. DOI: `10.1103/PRXQuantum.5.020315`.

[170] John Preskill. “Quantum computing in the NISQ era and beyond”. In: *Quantum* 2 (2018), p. 79. ISSN: 2521-327X. DOI: `10.22331/q-2018-08-06-79`.

[171] Sergei Filippov et al. *Scalable tensor-network error mitigation for near-term quantum computing*. 2023. arXiv: `2307.11740 [quant-ph]`.

[172] Sergey N. Filippov, Sabrina Maniscalco, and Guillermo García-Pérez. *Scalability of quantum error mitigation techniques: from utility to advantage*. 2024. arXiv: `2403.13542 [quant-ph]`.

[173] Andrew J. Ferris and David Poulin. “Tensor Networks and Quantum Error Correction”. In: *Phys. Rev. Lett.* 113 (3 2014), p. 030501. doi: `10.1103/PhysRevLett.113.030501`.

[174] Steven R. White. “Density matrix formulation for quantum renormalization groups”. In: *Phys. Rev. Lett.* 69 (19 1992), pp. 2863–2866. doi: `10.1103/PhysRevLett.69.2863`.

[175] Frank Verstraete, J. Ignacio Cirac, and Valentin Murg. “Matrix Product States, Projected Entangled Pair States, and variational renormalization group methods for quantum spin systems”. In: *Advances in Physics* 57.2 (2008), pp. 143–224. doi: `10.1080/14789940801912366`.

[176] J. Ignacio Cirac et al. “Matrix Product States and Projected Entangled Pair States: Concepts, Symmetries, and Theorems”. In: *Reviews of Modern Physics* 93.4 (2021), p. 045003. doi: `10.1103/RevModPhys.93.045003`.

[177] Sebastian Paeckel et al. “Time-evolution methods for matrix-product states”. In: *Annals of Physics* 411 (2019), p. 167998. doi: `10.1016/j.aop.2019.167998`.

[178] Roger Penrose. “Applications of negative dimensional tensors”. In: *Combinatorial Mathematics and its Applications*. Academic Press, 1971, pp. 221–244.

[179] Predrag Cvitanovic. *Group Theory, Birdtracks, Lie’s, and Exceptional Groups*. Princeton University Press, 2008.

[180] Jacob C Bridgeman and Christopher T Chubb. “Hand-waving and interpretive dance: an introductory course on tensor networks”. In: *Journal of Physics A: Mathematical and Theoretical* 50.22 (2017), p. 223001. doi: `10.1088/1751-8121/aa6dc3`.

[181] Frank Verstraete and J. Ignacio Cirac. “Matrix Product States Represent Ground States Faithfully”. In: *Physical Review B* 73.9 (2006), p. 094423. doi: `10.1103/PhysRevB.73.094423`.

[182] Frank Pollmann et al. “Entanglement properties of the square-lattice Heisenberg model”. In: *Physical Review B* 94.16 (2016), p. 165106. doi: `10.1103/PhysRevB.94.165106`.

[183] Sudipto Banerjee and Anindya Roy. *Linear Algebra and Matrix Analysis for Statistics*. 1st. Texts in Statistical Science. Chapman and Hall/CRC, 2014.

[184] James Bisgard. *Analysis and Linear Algebra: The Singular Value Decomposition and Applications*. 1st. Student Mathematical Library. American Mathematical Society, 2021.

[185] Marcus Huber and Julio I. de Vicente. “Structure of Multidimensional Entanglement in Multipartite Systems”. In: *Physical Review Letters* 110.3 (2013), p. 030501. issn: 0031-9007. doi: `10.1103/PhysRevLett.110.030501`.

[186] Asher Peres. “Higher order Schmidt decompositions”. In: *Physics Letters A* 202.1-2 (1995), pp. 16–17. doi: `10.1016/0375-9601(95)00308-G`.

[187] Jens Eisert and Hans J. Briegel. "Schmidt measure as a tool for quantifying multiparticle entanglement". In: *Physical Review A* 64.2 (2001), p. 022306. DOI: `10.1103/PhysRevA.64.022306`.

[188] Mark Srednicki. "Entropy and area". In: *Physical Review Letters* 71.5 (1993), pp. 666–669. DOI: `10.1103/PhysRevLett.71.666`.

[189] M. B. Hastings. "An area law for one-dimensional quantum systems". In: *Journal of Statistical Mechanics: Theory and Experiment* 2007.08 (2007), P08024. DOI: `10.1088/1742-5468/2007/08/P08024`.

[190] Itai Arad, Zeph Landau, and Umesh Vazirani. "Improved one-dimensional area law for frustration-free systems". In: *Physical Review B* 85.19 (2012). DOI: `10.1103/PhysRevB.85.195145`.

[191] Itai Arad et al. *An area law and sub-exponential algorithm for 1D systems.* 2013. arXiv: `1301.1162 [quant-ph]`.

[192] Anurag Anshu, Itai Arad, and David Gosset. "An area law for 2D frustration-free spin systems". In: *Proceedings of the 54th Annual ACM SIGACT Symposium on Theory of Computing (STOC 2022).* 2022. DOI: `10.1145/3519935.3519962`.

[193] Tao Xiang, Jizhong Lou, and Zhaobin Su. "Two-dimensional algorithm of the density-matrix renormalization group". In: *Physical Review B* 64.10 (2001), p. 104414. DOI: `10.1103/PhysRevB.64.104414`.

[194] Örs Legeza and Jenő Sólyom. "Quantum data compression, quantum information generation, and the density-matrix renormalization-group method". In: *Physical Review B* 70.20 (2004), p. 205118. DOI: `10.1103/PhysRevB.70.205118`.

[195] Guifre Vidal et al. "Entanglement in quantum critical phenomena". In: *Physical Review Letters* 90.22 (2003), p. 227902. DOI: `10.1103/PhysRevLett.90.227902`.

[196] Pasquale Calabrese and John Cardy. "Entanglement entropy and quantum field theory". In: *Journal of Statistical Mechanics: Theory and Experiment* 2004.06 (2004), P06002. DOI: `10.1088/1742-5468/2004/06/P06002`.

[197] Martin B. Plenio et al. "Entropy, entanglement, and area: analytical results for harmonic lattice systems". In: *Physical Review Letters* 94.6 (2005), p. 060503. DOI: `10.1103/PhysRevLett.94.060503`.

[198] B. Pirvu et al. "Matrix product operator representations". In: *New Journal of Physics* 12.2 (2010), p. 025012. DOI: `10.1088/1367-2630/12/2/025012`.

[199] C. Hubig, I. P. McCulloch, and U. Schollwöck. "Generic construction of efficient matrix product operators". In: *Phys. Rev. B* 95 (3 2017), p. 035129. DOI: `10.1103/PhysRevB.95.035129`.

[200] G. K.-L. Chan et al. “Matrix product operators, matrix product states, and ab initio density matrix renormalization group algorithms”. In: *The Journal of Chemical Physics* 145.1 (2016), p. 014102. doi: `10.1063/1.4955108`.

[201] Daniel E. Parker, Xiangyu Cao, and Michael P. Zaletel. “Local matrix product operators: Canonical form, compression, and control theory”. In: *Phys. Rev. B* 102 (3 2020), p. 035147. doi: `10.1103/PhysRevB.102.035147`.

[202] Amit Dutta et al. *Quantum Phase Transitions in Transverse Field Spin Models: From Statistical Physics to Quantum Information*. Cambridge University Press, 2015. doi: `10.1017/CBO9781107706057`.

[203] Y. Y. Atas and E. Bogomolny. “Quantum Ising model in transverse and longitudinal fields: chaotic wave functions”. In: *Journal of Physics A: Mathematical and Theoretical* 48.33 (2015), p. 335201. doi: `10.1088/1751-8113/48/33/335201`.

[204] S. Fey and K. P. Schmidt. “Quantum transverse-field Ising model on an infinite tree from matrix product states”. In: *Physical Review B* 94.7 (2016), p. 075156. doi: `10.1103/PhysRevB.94.075156`.

[205] I. P. McCulloch. “Infinite size density matrix renormalization group, revisited”. In: *arXiv* (2008). arXiv: `0804.2509 [cond-mat.str-el]`.

[206] Matthew Fishman, Steven R. White, and E. Miles Stoudenmire. “The ITensor Software Library for Tensor Network Calculations”. In: *SciPost Phys. Codebases* (2022), p. 4. doi: `10.21468/SciPostPhysCodeb.4`.

[207] Daniel E. Parker, Xiangyu Cao, and Michael P. Zaletel. “Local Matrix Product Operators: Canonical Form, Compression, & Control Theory”. In: *arXiv preprint arXiv:1909.06341* (2019).

[208] Cornelius Lanczos. “An iteration method for the solution of the eigenvalue problem of linear differential and integral operators”. In: *Journal of Research of the National Bureau of Standards* 45.4 (1950), pp. 255–282.

[209] Lloyd N. Trefethen and David Bau III. *Numerical Linear Algebra*. Philadelphia: SIAM, 1997.

[210] M. C. Bañuls et al. “The Mass Spectrum of the Schwinger Model with Matrix Product States”. In: *Journal of High Energy Physics* 2013.11 (2013), p. 158. doi: `10.1007/JHEP11(2013)158`.

[211] A J Daley et al. “Time-dependent density-matrix renormalization-group using adaptive effective Hilbert spaces”. In: *Journal of Statistical Mechanics: Theory and Experiment* 2004.04 (2004), P04005. doi: `10.1088/1742-5468/2004/04/P04005`.

[212] Steven R. White and Adrian E. Feiguin. “Real-Time Evolution Using the Density Matrix Renormalization Group”. In: *Phys. Rev. Lett.* 93 (7 2004), p. 076401. doi: `10.1103/PhysRevLett.93.076401`.

[213] Tao Xiang. *Density Matrix and Tensor Network Renormalization.* Cambridge University Press, 2023.

[214] Daniel Manzano. "A short introduction to the Lindblad master equation". In: *AIP Advances* 10.2 (2020), p. 025106. DOI: `10.1063/1.5115323`.

[215] Joel E. Cohen et al. "Eigenvalue inequalities for products of matrix exponentials". In: *Linear Algebra and Its Applications* 45 (1982), pp. 55–95. DOI: `10.1016/0024-3795(82)90211-7`.

[216] Christian W. Bauer et al. "Quantum Simulation for High-Energy Physics". In: *PRX Quantum* 4 (2 2023), p. 027001. DOI: `10.1103/PRXQuantum.4.027001`.

[217] D. Paulson et al. "Simulating 2D effects in lattice gauge theories on a quantum computer". In: *PRX Quantum* 2 (2021), p. 030334. DOI: `10.1103/PRXQuantum.2.030334`.

[218] L. Bassman et al. "Simulating quantum materials with digital quantum computers". In: *Quantum Science and Technology* 6 (2021), p. 043002. DOI: `10.1088/2058-9565/ac165b`.

[219] S. Thompson and G. Siopsis. "Quantum computation of phase transition in the massive Schwinger model". In: *Quantum Science and Technology* 7 (2022), p. 035001. DOI: `10.1088/2058-9565/ac6ad5`.

[220] M. C. Bañuls and K. Cichy. "Review on novel methods for lattice gauge theories". In: *Reports on Progress in Physics* 83 (2020), p. 024401. DOI: `10.1088/1361-6633/ab6311`.

[221] J. C. Halimeh et al. "Cold-atom quantum simulators of gauge theories". In: *arXiv e-prints* (2023). arXiv: `2310.12201 [cond-mat.quant-gas]`.

[222] A. Di Meglio et al. "Quantum computing for high-energy physics: state of the art and challenges. Summary of the QC4HEP working group". In: *arXiv e-prints* (2023). arXiv: `2307.03236`.

[223] G S Mamatha, Namya Dimri, and Rasha Sinha. *Post-Quantum Cryptography: Securing Digital Communication in the Quantum Era.* 2024. arXiv: `2403.11741 [cs.CR]`.

[224] Nicolas Gisin et al. "Quantum cryptography". In: *Rev. Mod. Phys.* 74 (1 2002), pp. 145–195. DOI: `10.1103/RevModPhys.74.145`.

[225] Nina Bindel et al. "Applications of Post-Quantum Cryptography". In: *arXiv preprint arXiv:2406.13258* (2024).

[226] Edward Farhi, Jeffrey Goldstone, and Sam Gutmann. "Quantum Approximate Optimization Algorithm: Performance, Mechanism, and Applications". In: *arXiv preprint arXiv:1602.07674* (2016). arXiv: `1602.07674 [quant-ph]`.

[227] Kostas Blekos et al. "A Review on Quantum Approximate Optimization Algorithm and its Variants". In: *Physics Reports* 1068 (2024), pp. 1–66. DOI: `10.1016/j.physrep.2024.03.002`.

[228] Amira Abbas et al. “Challenges and opportunities in quantum optimization”. In: *Nature Reviews Physics* 6.12 (2024), pp. 718–735. ISSN: 2522-5820. DOI: `10.1038/s42254-024-00770-9`.

[229] B. Camino et al. “Quantum computing and materials science: A practical guide to applying quantum annealing to the configurational analysis of materials”. In: *Journal of Applied Physics* 133.22 (2023), p. 221102. DOI: `10.1063/5.0151346`.

[230] D. Song, N.P. Bauman, G. Prawiroatmodjo, et al. “Periodic plane-wave electronic structure calculations on quantum computers”. In: *Materials Theory* 7 (2023), p. 2. DOI: `10.1186/s41313-022-00049-5`.

[231] J. Wright, M. Gowrishankar, D. Claudino, et al. “Numerical simulations of noisy quantum circuits for computational chemistry”. In: *Materials Theory* 6 (2022), p. 18. DOI: `10.1186/s41313-022-00047-7`.

[232] N.P. Bauman and K. Kowalski. “Coupled Cluster Downfolding Theory: Towards universal many-body algorithms for dimensionality reduction of composite quantum systems in chemistry and materials science”. In: *Materials Theory* 6 (2022), p. 17. DOI: `10.1186/s41313-022-00046-8`.

[233] L. Bassman Oftelie, R. Van Beeumen, E. Younis, et al. “Constant-depth circuits for dynamic simulations of materials on quantum computers”. In: *Materials Theory* 6 (2022), p. 13. DOI: `10.1186/s41313-022-00043-x`.

[234] G. Greene-Diniz, D.Z. Manrique, W. Sennane, et al. “Modelling carbon capture on metal-organic frameworks with quantum computing”. In: *EPJ Quantum Technologies* 9 (2022), p. 37. DOI: `10.1140/epjqt/s40507-022-00155-w`.

[235] Y. Cao et al. “Quantum chemistry in the age of quantum computing”. In: *Chemical Reviews* 119 (2019), pp. 10856–10915. DOI: `10.1021/acs.chemrev.8b00803`.

[236] S. McArdle et al. “Quantum computational chemistry”. In: *arXiv preprint arXiv:1808.10402* (2018). arXiv: `1808.10402`.

[237] Hrishikesh Dutta and Amit Kumar Bhuyan. *Quantum Communication: From Fundamentals to Recent Trends, Challenges and Open Problems*. 2024. arXiv: `2406.04492 [quant-ph]`.

[238] Maria Schuld, Ilya Sinayskiy, and Francesco Petruccione and. “An introduction to quantum machine learning”. In: *Contemporary Physics* 56.2 (2015), pp. 172–185. DOI: `10.1080/00107514.2014.964942`. eprint: `https://doi.org/10.1080/00107514.2014.964942`.

[239] Carlo Ciliberto et al. “Quantum Machine Learning: A Classical Perspective”. In: *Proceedings of the Royal Society A* 474.2209 (2018), p. 20170551. DOI: `10.1098/rspa.2017.0551`.

[240] Hsin-Yuan Huang et al. “Power of data in quantum machine learning”. In: *Nature Communications* 12.1 (2021), p. 2631. DOI: `10.1038/s41467-021-22539-9`.

[241] Antonio Macaluso. “Quantum Supervised Learning”. In: *KI - Künstliche Intelligenz* 38.4 (2024), pp. 277–291. DOI: `10.1007/s13218-024-00856-7`.

[242] Yaswitha Gujju, Atsushi Matsuo, and Rudy Raymond. “Quantum machine learning on near-term quantum devices: Current state of supervised and unsupervised techniques for real-world applications”. In: *Phys. Rev. Appl.* 21 (6 2024), p. 067001. DOI: `10.1103/PhysRevApplied.21.067001`.

[243] D. Herman, C. Googin, X. Liu, et al. “Quantum computing for finance”. In: *Nature Reviews Physics* 5 (2023), pp. 450–465. DOI: `10.1038/s42254-023-00603-1`.

[244] Arianna Crippa et al. “Quantum computing inspired paintings: reinterpreting classical masterpieces”. In: *arXiv* (2024). arXiv: `2411.09549 [quant-ph]`.

[245] Giuseppe Clemente et al. *New Directions in Quantum Music: concepts for a quantum keyboard and the sound of the Ising model.* 2022. arXiv: `2204.00399 [quant-ph]`.

[246] J. C. L. Chow. “Quantum Computing in Medicine”. In: *Medical Sciences (Basel, Switzerland)* 12.4 (2024), p. 67. DOI: `10.3390/medsci12040067`.

[247] B. Fauseweh. “Quantum many-body simulations on digital quantum computers: State-of-the-art and future challenges”. In: *Nature Communications* 15 (2024), p. 2123. DOI: `10.1038/s41467-024-46402-9`.

[248] Y. Dong, K. B. Whaley, and L. Lin. “A quantum Hamiltonian simulation benchmark”. In: *npj Quantum Information* 8 (2022), p. 131. DOI: `10.1038/s41534-022-00636-x`.

[249] Seth Lloyd. “Universal Quantum Simulators”. In: *Science* 273 (1996), pp. 1073–1078. DOI: `10.1126/science.273.5278.1073`.

[250] Oleg M. Sotnikov et al. “Achieving the volume-law entropy regime with random-sign Dicke states”. In: *Phys. Rev. A* 110 (6 2024), p. 062416. DOI: `10.1103/PhysRevA.110.062416`.

[251] A. Peruzzo et al. “A variational eigenvalue solver on a photonic quantum processor”. In: *Nature Communications* 5 (2014), p. 4213. DOI: `10.1038/ncomms5213`.

[252] Jan Lukas Bosse, Raul A Santos, and Ashley Montanaro. “Sketching phase diagrams using low-depth variational quantum algorithms”. In: *Quantum Science and Technology* 9.3 (2024), p. 035034. DOI: `10.1088/2058-9565/ad4979`.

[253] John Preskill. “Noisy Intermediate-Scale Quantum (NISQ) Era”. In: *Quantum* 2.1 (2018), p. 79. DOI: `10.22331/q-2018-08-06-79`.

[254] Ewout van den Berg, Zlatko K. Minev, and Kristan Temme. “Model-free readout-error mitigation for quantum expectation values”. In: *Phys. Rev. A* 105 (3 2022), p. 032620. DOI: `10.1103/PhysRevA.105.032620`.

[255] Tudor Giurgica-Tiron et al. “Digital zero noise extrapolation for quantum error mitigation”. In: *2020 IEEE International Conference on Quantum Computing and Engineering (QCE).* 2020, pp. 306–316. DOI: 10.1109/QCE49297.2020.00045.

[256] Joel J. Wallman and Joseph Emerson. “Noise tailoring for scalable quantum computation via randomized compiling”. In: *Phys. Rev. A* 94 (5 2016), p. 052325. DOI: 10.1103/PhysRevA.94.052325.

[257] L. Viola and S. Lloyd. “Dynamical suppression of decoherence in two-state quantum systems”. In: *Physical Review A* 58.3 (1998), pp. 2733–2744. DOI: 10.1103/PhysRevA.58.2733.

[258] Dong C. Liu and Jorge Nocedal. “On the limited memory BFGS method for large scale optimization”. In: *Mathematical Programming* 45.1 (1989), pp. 503–528. DOI: 10.1007/BF01589116.

[259] N. Boulant et al. “Incoherent Noise and Quantum Information Processing”. In: *The Journal of Chemical Physics* 121.7 (2004), pp. 2955–2961. DOI: 10.1063/1.1773161.

[260] Michael K. Henry et al. “Signatures of Incoherence in a Quantum Information Processor”. In: *Physical Review A* 75.2 (2007), p. 022318. DOI: 10.1103/PhysRevA.75.022318.

[261] Ying Li and Simon C. Benjamin. “Efficient Variational Quantum Simulator Incorporating Active Error Minimization”. In: *Phys. Rev. X* 7 (2 2017), p. 021050. DOI: 10.1103/PhysRevX.7.021050.

[262] K. Temme, S. Bravyi, and J. M. Gambetta. “Error Mitigation for Short-Depth Quantum Circuits”. In: *Physical Review Letters* 119.18 (2017), p. 180509. DOI: 10.1103/PhysRevLett.119.180509.

[263] E. Knill. *Fault-Tolerant Postselected Quantum Computation: Threshold Analysis.* 2004. arXiv: quant-ph/0404104 [quant-ph].

[264] Joe O’Gorman et al. “A silicon-based surface code quantum computer”. In: *npj Quantum Information* 2.1 (2016), p. 15019. DOI: 10.1038/npjqi.2015.19.

[265] Zhenyu Cai, Xiaosi Xu, and Simon C. Benjamin. “Mitigating coherent noise using Pauli conjugation”. In: *npj Quantum Information* 6.1 (2020), p. 17. DOI: 10.1038/s41534-019-0233-0.

[266] Gunnar S. Bali et al. “Scale setting and the light baryon spectrum in $\mathrm{Nf} = 2 + 1$ QCD with Wilson fermions”. In: *Journal of High Energy Physics* 2023.5 (2023), p. 35. DOI: 10.1007/JHEP05(2023)035.

[267] Ross Dempsey et al. “Discrete chiral symmetry and mass shift in the lattice Hamiltonian approach to the Schwinger model”. In: *Phys. Rev. Res.* 4 (4 2022), p. 043133. DOI: 10.1103/PhysRevResearch.4.043133.

[268] Ch. Hoelbling. “Lattice QCD: Concepts, Techniques and Some Results”. In: *Acta Physica Polonica B* 45.12 (2014), p. 2143. DOI: 10.5506/aphyspolb.45.2143.

[269] Richard L. Burden and J. Douglas Faires. *Numerical Analysis*. 9th. Brooks/Cole, Cengage Learning, 2011.

[270] Mei Huang and Pengfei Zhuang. “QCD Matter and Phase Transitions under Extreme Conditions”. In: *Symmetry* 15.2 (2023), p. 541. ISSN: 2073-8994. DOI: `10.3390/sym15020541`.

[271] Philippe de Forcrand. “Simulating QCD at finite density”. In: *PoS* LAT2009 (2009). Ed. by Chuan Liu and Yu Zhu, p. 010. DOI: `10.22323/1.091.0010`. arXiv: `1005.0539 [hep-lat]`.

[272] A. Yu. Kitaev. “Quantum measurements and the Abelian Stabilizer Problem”. In: *arXiv e-prints*, quant-ph/9511026 (1995), quant–ph/9511026. DOI: `10.48550/arXiv.quant-ph/9511026`. arXiv: `quant-ph/9511026 [quant-ph]`.

[273] Vicente Azcoiti et al. “Massive Schwinger model at finite $\theta$”. In: *Phys. Rev. D* 97 (1 2018), p. 014507. DOI: `10.1103/PhysRevD.97.014507`.

[274] Matthew D. Schwartz. *Quantum Field Theory and the Standard Model*. Cambridge University Press, 2014. ISBN: 978-1-107-03473-0, 978-1-107-03473-0.

[275] Min He, Hendrik van Hees, and Ralf Rapp. “Heavy-quark diffusion in the quark-gluon plasma”. In: *Prog. Part. Nucl. Phys.* 130 (2023), p. 104020. DOI: `10.1016/j.ppnp.2023.104020`.

[276] T. Matsui and H. Satz. “J/$\psi$ suppression by quark-gluon plasma formation”. In: *Physics Letters B* 178.4 (1986), pp. 416–422. ISSN: 0370-2693. DOI: `https://doi.org/10.1016/0370-2693(86)91404-8`.

[277] A. Andronic et al. “Comparative study of quarkonium transport in hot QCD matter”. en. In: *The European Physical Journal A* 60.4 (2024), p. 88. ISSN: 1434-601X. DOI: `10.1140/epja/s10050-024-01306-6`.

[278] Jean-Paul Blaizot et al. “Heavy quark bound states in a quark–gluon plasma: Dissociation and recombination”. en. In: *Nuclear Physics A* 946 (2016), pp. 49–88. ISSN: 03759474. DOI: `10.1016/j.nuclphysa.2015.10.011`.

[279] Bruno Scheihing-Hitschfeld and Xiaojun Yao. “Real time quarkonium transport coefficients in open quantum systems from Euclidean QCD”. In: *Phys. Rev. D* 108 (5 2023), p. 054024. DOI: `10.1103/PhysRevD.108.054024`.

[280] Takahiro Miura et al. “Quantum Brownian motion of a heavy quark pair in the quark-gluon plasma”. In: *Phys. Rev. D* 101 (3 2020), p. 034011. DOI: `10.1103/PhysRevD.101.034011`.

[281] Rishi Sharma and Anurag Tiwari. “Quantum evolution of quarkonia with correlated and uncorrelated noise”. In: *Phys. Rev. D* 101 (7 2020), p. 074004. DOI: `10.1103/PhysRevD.101.074004`.

[282] Nicholas S. Manton. “The Schwinger Model and Its Axial Anomaly”. In: *Annals of Physics* 159.2 (1985), pp. 220–251. DOI: 10.1016/0003-4916(85)90148-9.

[283] Mari Carmen Bañuls. “Tensor Network Algorithms: A Route Map”. In: *Annual Review of Condensed Matter Physics* 14.Volume 14, 2023 (2023), pp. 173–191. ISSN: 1947-5462. DOI: https://doi.org/10.1146/annurev-conmatphys-040721-022705.

[284] Pietro Silvi et al. “Lattice gauge tensor networks”. In: *New Journal of Physics* 16.10 (2014), p. 103015. DOI: 10.1088/1367-2630/16/10/103015.

[285] C Adam. “General bound-state structure of the massive Schwinger model”. In: *Physics Letters B* 382.1 (1996), pp. 111–116. ISSN: 0370-2693. DOI: https://doi.org/10.1016/0370-2693(96)00639-9.

[286] Guo-Xian Su, Jesse J. Osborne, and Jad C. Halimeh. “Cold-Atom Particle Collider”. In: *PRX Quantum* 5 (4 2024), p. 040310. DOI: 10.1103/PRXQuantum.5.040310.

[287] F. Riek and R. Rapp. “Quarkonia and heavy-quark relaxation times in the quark-gluon plasma”. In: *Phys. Rev. C* 82 (3 2010), p. 035201. DOI: 10.1103/PhysRevC.82.035201.

[288] Yuhei Morino. *Production of charm and bottom quarks in $p+p$ collisions at 200GeV*. 2009. arXiv: 0903.3504 [nucl-ex].

[289] A. Adare et al. “Measurement of Bottom Versus Charm as a Function of Transverse Momentum with Electron-Hadron Correlations in $p+p$ Collisions at $\sqrt{s}=200$ GeV”. In: *Phys. Rev. Lett.* 103 (8 2009), p. 082002. DOI: 10.1103/PhysRevLett.103.082002.

[290] Ze-Bo Tang, Wang-Mei Zha, and Yi-Fei Zhang. “An experimental review of open heavy flavor and quarkonium production at RHIC”. In: *Nuclear Science and Techniques* 31.8 (2020), p. 81. DOI: 10.1007/s41365-020-00785-8.

[291] Shouxing Zhao and Min He. “Second-order dissociation and transition of heavy quarkonia in the quark-gluon plasma”. In: *Phys. Rev. D* 110 (7 2024), p. 074040. DOI: 10.1103/PhysRevD.110.074040.

[292] Nora Brambilla et al. “Heavy quarkonium suppression in a fireball”. In: *Phys. Rev. D* 97 (7 2018), p. 074009. DOI: 10.1103/PhysRevD.97.074009.

[293] Simon Caron-Huot and Guy D. Moore. “Heavy Quark Diffusion in Perturbative QCD at Next-to-Leading Order”. In: *Phys. Rev. Lett.* 100 (5 2008), p. 052301. DOI: 10.1103/PhysRevLett.100.052301.

[294] John W. Harris and Berndt Müller. ““QGP Signatures”revisited”. In: *The European Physical Journal C* 84.3 (2024), p. 247. DOI: 10.1140/epjc/s10052-024-12533-y.

[295] F. Karsch, D. Kharzeev, and H. Satz. “Sequential charmonium dissociation”. In: *Physics Letters B* 637.1 (2006), pp. 75–80. ISSN: 0370-2693. DOI: https://doi.org/10.1016/j.physletb.2006.03.078.

# Erklärung

Ich erkläre, dass ich die Dissertation selbständig und nur unter Verwendung der von mir gemäß § 7 Abs. 3 der Promotionsordnung der Mathematisch-Naturwissenschaftlichen Fakultät, veröffentlicht im Amtlichen Mitteilungsblatt der Humboldt-Universität zu Berlin Nr. 42/2018 am 11.07.2018, angegebenen Hilfsmittel angefertigt habe.

Berlin, September 24, 2025

Takis Angelides